POLITECNICO DI TORINO

Doctorate School
Ph.D in: “Metrology: measuring science and technique” – XXIV cycle

Doctorate Thesis

Innovative Plastic Optical Fiber Sensors

POF sensors and related acquisition systems for
the measurement of displacement, vibration and acceleration

Maria Luisa Casalicchio

Advisors
Alberto Vallan
Guido Perrone

2012

Contents

Summary

This thesis describes the development of new types of fiber optic sensors for the measurement of mechanical quantities such as displacement, vibration and acceleration.
Also, it describes the realization of specific acquisition systems designed to interrogate the developed sensors.
Since optical fibers have been historically associated with high speed telecommunication links because of their very large bandwidth and low attenuation, there is a great interest for their employment in sensor applications.
Fiber sensors represent a promising solution in many fields since fibers can be used for the measurement of several quantities, not only mechanical as those investigated in this work, but also chemical with the possibility to detect specific chemical or bio-chemical molecules.
Among the physical quantities to be detected, the displacement measurement is required in some applications, especially in structural civil and mechanical fields, where it is possible to evaluate the cracks evolution, providing information about the safety of the structure under monitoring in order to detect eventually risky situations.

All the developed sensors are able to measure the displacement along one or two axis, that can be employed also during vibration tests especially at high frequencies, and also acceleration sensors to monitor acceleration at low frequencies.
The developed sensors are based on plastic optical fibers instead of the traditional glass fibers, which are traditionally employed in optical communications.
This change is related to the aim of realizing sensors maintaining the excellent typical characteristics of the fibers, such as electromagnetic immunity, intrinsically fire safety and flexibility of applications, but with costs comparable to those of commercial electromechanical sensors.
Indeed, nowadays, the commercial fiber optic sensors are based on glass fibers because they have very good performance.
However, they find limited applications due to the high costs of their complex interrogation systems and also for the procedure required to splice the fibers.
On the other hand, plastic optical fibers represent a promising alternative because of their geometrical and optical properties that allow employing low-cost non coherent sources such as LED and also simplifying the procedure for the sensor connection and installation.

Therefore, the design of the proposed plastic optical fiber displacement sensors is described with the sensor practical arrangement and the realized prototypes. An acquisition system has been designed and realized to characterize the sensors and the characterization results are also provided. Moreover, the development and the characterization of a plastic optical fiber sensor able to measure the displacement in two directions have been described.

The main drawback of the developed sensors are stability issues and for this reason laboratory and in situ-tests have been carried out in order to verify the sensor performance over the time.

The results obtained with the stability tests have highlighted the necessity to develop displacement sensors with increased stability. To this aim, a compensation technique based on two different wavelengths has been developed.

The same working principle of the developed displacement sensor has been exploited to realize a fiber vibrometer to be employed during the vibration monitoring for measuring without contact the vibrations of the device under test.
The sensor development, a suitable calibration procedure developed to overcome the problem of real targets with a non uniform reflectivity, and the experimental tests have been described.

Furthermore, the preliminary results concerning the feasibility study of a plastic optical fiber accelerometer are reported.

Chapter 1

Background

1.1 Optical fibers technology

Optical fibers have been historically associated with high speed telecommunication links because of their very large bandwidth and low attenuation, but there is a growing interest also for their use in sensing applications.
Indeed, Fiber Optic Sensors (FOS) represent an attractive solution in many fields since fibers can be used for the measurement of physical (e.g. strain, displacement, temperature, pressure, velocity, acceleration) and chemical (e.g. PH) quantities, as well as for the detection of specific chemical or bio-chemical molecules (e.g. air and water pollutants, glucose contents in blood, DNA sequencing).

Considering the measurement of physical quantities, one of the most relevant applications of FOS is in Structural Health Monitoring (SHM), which is the process that allows establishing the current condition of a structure, starting from the analysis of suitable physical parameters, such as position, deformation, inclination, strain, force, pressure, acceleration and vibration.
In particular, continuous SHM, with remote supervision, using sensors integrated within the structure, has gained an increasing attention in the last years as new types of sensors have become available, providing early warnings of possibly unsafe conditions.
Of course, this continuous SHM to be effective requires the deployment of a large number of sensors, and real-time data processing and accurate interpretation of the measured signals.
Therefore, one of the SHM new frontiers is the development of automatic data processing algorithms to be used with embedded measurements systems for the continuous real-time evaluation of forces acting on the structure, with the objective of identifying the onset of critical damages and determine the appropriate action to guarantee the structure health, or in alternative, at least estimate the lifetime of the structure.
Focusing on the measurement systems, since SHM can be applied to the evaluation of different types of structures (bridges, buildings, tunnels, dams, but also cultural heritages), the requirements for the sensors and the data acquisition architecture are quite different, too.
More in detail, buildings and bridges usually require monitoring the concrete during the setting period, the displacement of joints, the neutral axis evolution, the long-term deformation of beams, the concrete-steel interactions, and the evolution of cracks due to aging or earthquakes. In tunnels, instead, it is typically necessary to monitor vaults and joints are necessary, while in dams it is important to monitor foundations, joint expansion, displacement and temperature in various locations.

The more and more relevant role of FOS [1] in SHM is due to the intrinsic properties of optical fibers such as lightweight, flexible adaptation to various geometries, possibility of being embedded directly into the structure, immunity to electromagnetic interference, and impossibility to start fires.

So, given the widespread interest for FOS, many working principles have been investigated in the literature, such as intensity-variation [2], [3], wavelength shifts, [4], change of polarization, interferometry [5], [6] and optical triangulation [7].

Typical intensiometric fiber sensors are basically composed of at least one optical fiber span, a light source and a receiver built on a photodiode and a transimpedance amplifier, so they are quite straightforward to implement.

Their simplicity is, however, also their main limitation because by relating the quantity under measure with the light intensity, they are sensitive to any perturbation that may change the received power, including parasitic quantities, such as fiber propagation loss variation due to aging and temperature and stray light.

Today, practically all the commercial FOS employ silica fibers, similar to those used for telecommunications, and indeed, some intensiometric sensors are available on the market as an alternative solution to traditional electromechanical sensors [8].

Anyway, despite their excellent performances, FOS are still limited mainly to niche applications due to the high costs of currently available commercial interrogators (e.g. some thousands of euro), and this is especially true for crack monitoring applications in which they have to compete with very low-cost traditional alternatives.

Moreover, other difficulties hampering the FOS widespread deployment come from the complex equipment needed to connect fibers and the level of expertise required to handle them.

For this reason, in the recent past, a number of research groups from universities and industries have pioneered the replacement of standard glass fibers with Plastic Optical Fibers (POF) with the main objective of decreasing the costs of the measurement system exploiting the simplifications in the connections and source requirements allowed by these fibers. Examples of monitoring applications using both single-mode [9], and multimode plastic fibers [10] [11] have already been reported in literature.

In brief, POF allow maintaining the advantages intrinsically related to the fiber nature itself, but having higher light collecting capabilities, they do not require expensive equipment to handle them.

1.2 Doctoral activity

The Ph.D. activity described in this thesis has regarded the investigation of plastic optical fiber sensors for the measurement of displacements and vibrations, with the aim of reaching the same advantages of “traditional” fiber optic sensors, but with much lower costs thanks to the development of simplified interrogators.
Main applications of the studied sensing systems are in cultural heritage preservation (e.g. long-term crack monitoring) and in industrial measurements (e.g. determination of vibration amplitudes and frequencies of machines).

First, a review of fiber and electromechanical sensors for measuring displacements and vibrations has been carried out, studying the working principles of FOS presented in the literature, and comparing the performance of commercially available devices.
Considering the typical requirements of crack and vibration monitoring applications, and the constraint of keeping the measurement system overall costs low, the research activity has been focused on the development of intensity-variation plastic fiber sensors.
Therefore, the power distribution in highly multimode plastic fiber has been studied, and models have been developed in order to predict the sensor response with the quantity under measurement.

Then, sensor prototypes have been arranged to verify the feasibility of the chosen approach and sensors measuring displacement in one and two directions have been developed and characterized for the crack monitoring. Also, the developed displacement sensors able to measure the displacement along one direction have been tested in laboratory. Some of these sensors have been also tested in field to assess their performance in practical applications, in particular in the Chapel of the Holy Shroud in the framework of the Progetto Guarini, where it was requested to install a crack permanent monitoring system. The experimental results have highlighted some stability issues, especially in case of long-term monitoring. To overcome this limitation, a new sensor with improved stability has been designed and implemented, and experimental tests carried out in laboratory have confirmed the theoretic expectations.

Plastic fibers vibration sensors have been studied in response to the technological challenges set by two research projects promoted by the “Regione Piemonte”. The first is namely “MAESS: Development of a standardized modular platform for low-cost nano- and micro-satellites and applications to low-cost space missions and to Galileo”.
In this framework it was necessary to develop a sensor for monitoring the vibration tests of electronic modules of nano-satellites. The second is namely “LaserFactory: Next generation of machines based on fiber lasers for massive production in the automotive and aerospace insdustry”.
In this framework it was requested to investigate the possibility to employ low-cost plastic optical fiber sensors to detect vibration and accelerations of industrial machines in working conditions, such as moving arms of high-precision laser cutting and welding machines.

1.3 Plastic optical fibers overview

The optical fibers are defined as optical waveguides basically composed of two cylinders, as schematized in Fig. 1.1, constituted from materials having different refractive indexes.
The light propagation in the fiber happens because the inner cylinder, namely *core*, has a greater refractive index than the outer cylinder, namely *cladding*.

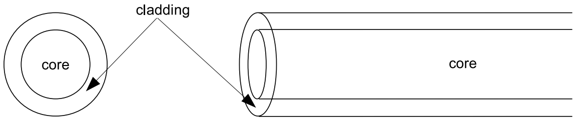

Figure 1.1. Optical fiber representation: front and lateral view.

The main parameters characterizing an optical fiber are: material, diameter, numerical aperture (related to the difference between core and cladding refractive index) and attenuation.
Typically, plastic optical fibers have a large core, usually constituted from PolyMethylMethachrylate (PMMA), better known as *Plexiglas*, and a thin cladding, composed from fluorinated polymers. Also, typical values for fiber diameter are between 0.25 mm and 1 mm, (i.e. approximately core diameter is 0.98 mm and the remaining part is constituted from cladding), that are typically greater than the diameters of glass fibers, give to the fibers robustness and easiness of employment.
The numerical aperture (NA) of POF is typically 0.5, that is greater than in the glass fibers, and allows to plastic fibers to collect a great amount of light, as larger is NA greater is amount of the received light.
Moreover, exploiting the dependence from the numerical aperture, it is possible design extrinsic intensity based fiber sensors.
On the contrary of the silica fibers, in the plastic optical fibers the attenuation is higher, and changes not only with the fiber length but also in the visible spectrum according to the wavelength employed to light the fiber. The only advantage is that the minimum of attenuation occurs in the visible part of the spectrum, approximately in the green-red region, and this simplifies the alignments.
Anyway, the attenuation can slightly change according to the fiber diameter, manufacturer or production lot and for other factors, not so easily measurable (they will be further analyze in the following of this work), like as the environmental conditions whose the fiber is subjected, the source stability, the fiber bending, the fiber ageing.
Thus, the attenuation of plastic fibers is an issue that has to be investigate carefully.
Consequently, the fiber span maximum length useful to realize fiber sensors is strictly dependent on the fiber attenuation effects and typically is about few of tenths of meters. [1].

---

[1] Further details about optical fibers properties and plastic optical fibers characteristics are reported in Appendix

Chapter 2

Development of a POF displacement sensor for crack monitoring

2.1 Crack monitoring issue

Crack monitoring is useful in the structural health monitoring (SHM) of civil structures, like buildings and cultural heritage structures, because the crack evolution monitoring provides information about the health of the structure under observation in order to evaluate the safety conditions and eventual damages, allowing a preventive diagnosis of potentially risky situations.
Since the crack evolution is typically slow, to this aim the crack displacement measurement has to be carried out for a long-term period and the expected displacements have the order of magnitude of few millimeters in a long period (from months to years) and then, the required uncertainties have to be maintained about below 0.1 mm.
Moreover, some studies in literature have been demonstrated that important structural information can be obtained from the measurement of a crack evolution also in a short-term monitoring.
In this case, the phenomenon of interest is a vibration of the crack, and then the measurement has to be carried out at high frequency, in the order of kilohertz, with a micrometric uncertainty, since the expected displacements are below 1 mm.
Since the crack evaluation has to be detected over a certain period of time, the monitoring is namely respectively *Short-term* monitoring or *Long-Term* monitoring, according to the measurement period. Typically, short-term is considered from few seconds up to few days, while the long-term is from a month and extended up to some years.
It is evident that measuring cracks for different periods requires sensors with different characteristics, both in terms of maximum operating range and resolution.
Typical sensors employed in the crack monitoring are mechanical, such as examples shown in Fig. 2.1. They are calipers, having typically 0.05 mm of resolution, crack gauges or extensometers [12], having typically 1 mm accuracy in a 25 mm sensor working range, and electronic devices (potentiometers, Linear Variable Differential Transducers (LVDT) [13], Eddy-current sensors), whose example shown in Fig. 2.2.
LVDT commercial sensors have typically a working range from 1 mm to 50 mm, with a micrometric resolution and a good linearity. Otherwise, inductive sensors have typically sub−micrometric

resolution at the expense of a reduced working range, even below 1 mm, while potentiometers measure displacements with micrometric resolution but limited stability, so they are not suitable for long-term monitoring.

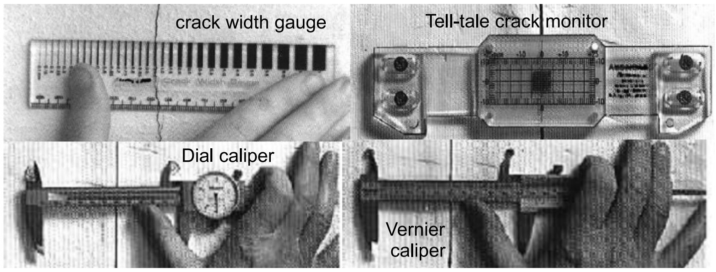

Figure 2.1. Example of mechanical crack sensors

Figure 2.2. Example of electronic crack sensors

Nowadays, also the employment of optical sensors is currently growing, in particular using vision based, laser triangulation and fiber based systems, whose examples are shown in Fig. 2.3.
Among fiber based sensors [5], the most diffused are glass fiber interferometers, sensors based on Optical Time Domain Reflectometer (OTDR) technique and Fiber Bragg Grating (FBG) sensors, that are widely employed for SHM applications, in particular arranged to measure physical quantities such as temperature, strain and acceleration. [1]
Commercial FBG sensors can detect mechanical strain with a resolution lower than 1 $\mu\varepsilon$ but they have a limited range, typically up to a fraction of millimeters, due to the fragility of glass fibers. Thus, these sensors are not suitable for crack measurement in a long-term monitoring because the expected displacement can easily overcome the grating breaking limit.
Comparing the optical sensors performance based on different technologies, the vision based systems present millimetric working range and micrometric resolution but require the presence of an operator, fiber interferometers have better performances than the previous but at expense of

---

[1] Further details about OTDR technique and FBG sensors are reported in Appendix.

Figure 2.3. Example of optical crack sensors

high complexity for the sensor interrogation system at high costs, while FBG sensors require high resolution interrogators (based on optical spectrum analyzers) and consequently have high costs. The aim of this research activity is therefore the development of an alternative solution based on optical technology but having a reduced cost.

2.2 POF sensor for displacement measurements

The work aim is the development and the realization of a low-cost optical sensor to measure displacements.
These requirements can be fullfilled developing an intensity based sensor. In this type of sensors the quantity under measurement, in this case the displacement, is related to the optical power and hence, this quantity can be easily measured using very low-cost components.
The simplest sensor configuration exploits the light intensity changes with the distance, as shown in Fig. 2.4, where the light is launched inside a transmitting fiber and it is collected from a receiving fiber that routes the light to an optical detector. The collected light depends on the optical power at the receiving fiber that in turn depends on the distance between fibers tips d and on the light cone angle θ_a. This angle is defined as the half angle of the light cone.
The emitted light cone, having the vertex O inside the fiber, is called *Acceptance Cone* or *Emission Cone*.
The maximum value that the angle θ_a can assume is called θ_{max} and it is strictly related to an intrinsic fiber property [2], the *Numerical Aperture* (NA), defined as (Eq.2.1):

$$NA = n_0 \cdot \sin\theta_{max} \tag{2.1}$$

For this reason, this sensor is also called *Numerical Aperture Sensor*.

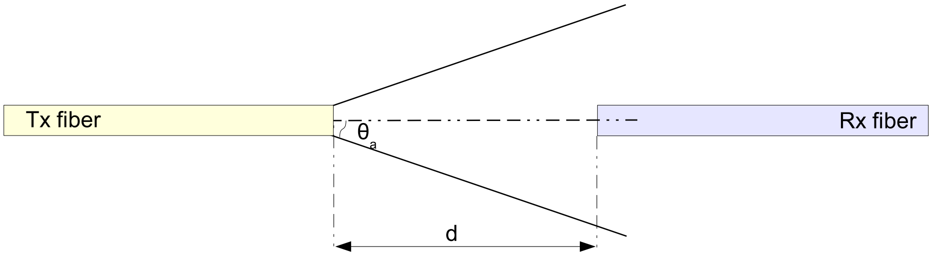

Figure 2.4. Sketch of the simplest sensor configuration: the light is propagated inside a transmitting fiber and reaches a receiving fiber placed at a certain distance d to the transmitting fiber.

Numerical aperture sensors can be realized according two types of structures:

- *Transmission* structure
- *Reflection* structure

that are respectively schematized in Fig. 2.5 and in Fig. 2.6.

In the *Transmission structure* the fibers are faced at a certain distance d, while in the *Reflection structure* there are at least two parallel fibers, one transmits the light to a reflecting target while the other collects the light reflected from the target.
In both cases, one fiber, namely transmitting fiber or “Tx fiber” of radius r_{TX}, transmits the light and the other, namely receiving fiber or “Rx fiber”, collects the received light.
Also, the light cone has a vertex O inside the transmitting fiber placed at a certain distance from the fiber tip, that is equal to $z_a = r_{TX}/tan(\theta_a)$.

---

[2] Further details about fiber optical properties are reported in Appendix.

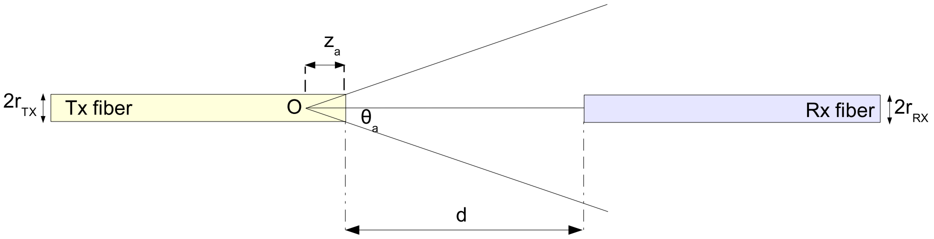

Figure 2.5. Sketch of the transmission structure: a transmitting fiber lights the receiving fiber placed at a certain distance *d*.

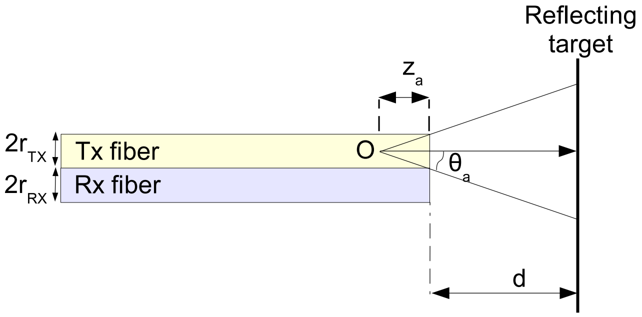

Figure 2.6. Sketch of the reflection structure: a transmitting fiber lights a reflecting target at a certain distance *d* from the fiber tip and the light reflected from the target is collected by the receiving fiber.

In the following sections is described the sensor optical model useful to evaluate the sensor metrological characteristics.

2.2.1 Power distribution model in numerical aperture sensors

It is possible to evaluate the optical power distribution in numerical aperture plastic fiber sensors, taking into account of a theoretical model [14] already developed for multimode glass fibers sensors arranged in a reflection structure.
Anyway, the relationship between the distance and the optical power collected by the receiving fiber can be found, independently from the structure, considering the light modeled as rays, according to the:

- **geometrical model**: the light is confined inside a cone (the power outside the light cone is null), and the light diffraction effects at the cone boundaries are neglected.
- **gaussian model**: this approach accounts for the power outside the light cone boundaries.

The following sections describe how the optical power model can be applied in the case of the sensor arranged in transmission and in reflection structure, respectively.

Sensor arranged in transmission structure

Considering the equivalent sensor structure such as that shown in Fig. 2.5, the obtained sensor sketch according to the **geometrical model** is schematized in Fig. 2.7.
Here, the fibers have the same radius w_a in order to simplify the model and θ_a is the acceptance angle related to the half light cone.
The distance z' is evaluated between the fiber tips, z_a is the distance between the cone vertex and the transmitting fiber tip, depending for definition on the fiber radius and the angle related to the light cone.
The z-axis (z) has the origin in the cone vertex and is aligned with the emitted light cone axis, the y-axis (y) is perpendicular to the fiber axis, and w is the radius of the circular cross section corresponding to the light cone having the following expression:

$$w(z) = z' \cdot \tan\theta_a = z' \frac{w_a}{z_a} \tag{2.2}$$

Since the receiving fiber has coordinates $Q' : (y = 0; z = z')$, it is evident that this fiber is always totally illuminated. The optical power emitted by the transmitting fiber is namely P_E and the irradiance I can be considered constant for all points with the same z-coordinate that are inside the irradiance cone, while it is null outside the cone, as reported in the following expression (Eq. 2.3):

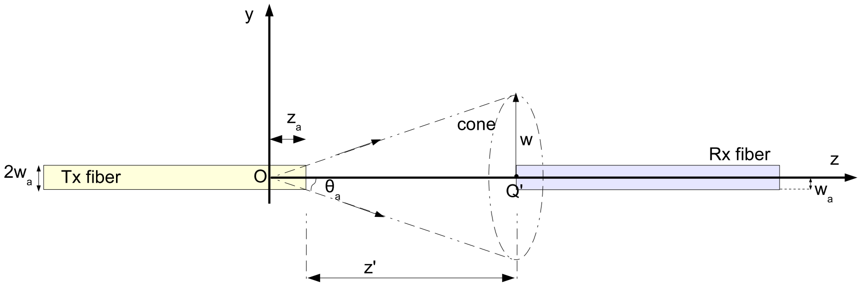

Figure 2.7. Sketch of the equivalent circuit according to the geometrical approach for the sensor arranged in transmission structure.

$$I(z) = \frac{P_E}{\pi \cdot \omega^2(z)}; \quad \mid \theta \mid \leq \theta_a \tag{2.3}$$

$$I(z) = 0; \quad \mid \theta \mid > \theta_a \tag{2.4}$$

The optical power collected at the end of the receiving fiber is obtained integrating the irradiance over the receiving fiber surface S, that is the illuminated area.
In first approximation, the irradiance can be considered constant over the entire surface and therefore the collected power can be obtained multiplying the correspondent illuminated area by the irradiance value evaluated at the fiber center.
Thus, it is possible obtain the expression of the collected power at the receiving fiber tip (Eq. 2.5):

$$P_{RX}(z) = S \cdot I(z) = P_E \cdot \frac{w_a^2}{[\tan(\theta_a)]^2} \cdot \frac{1}{z^2} \tag{2.5}$$

As an example, the geometrical model has been applied to study a sensor in transmission structure composed of two fibers with radius $w_a = 0.5$ mm and NA = 0.5, obtaining the ratio between the

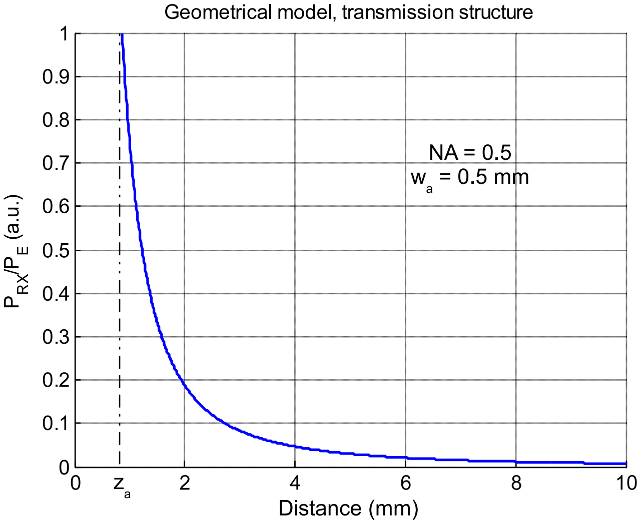

Figure 2.8. Normalized received power according to the geometrical approach for the sensor arranged in transmission structure.

received power and the input power, that is shown in Fig. 2.8. When the fiber tips are in contact ($z = z_a$) the received power is equal to the transmitted power. Otherwise, when there is a gap between the fiber tips, the ratio P_{RX}/P_E decreases because the distance z' increases, according to a law depending to the inverse of the square of the distance. The sensor behavior is thus strongly not linear and presents an high sensitivity for small distances.

On the other hand, the sensor sketch according to the **gaussian model** is schematized in Fig. 2.9, where w_0, namely *waist radius*, is the minimum width beam in correspondence of the cone vertex while w is the generical width of the light beam in correspondence of the receiving fiber tip.

Both are according to the z-axis (z) that has the origin in the cone vertex and it is aligned with the cone axis, while the vertical axis is perpendicular to the fiber axis and it is represented with a generical radial coordinate r. The measurement of the beam width in the gaussian model w is obtained through Eq. 2.6:

$$w(z) = w_0 \cdot \sqrt{1 + \left(\frac{z}{z_R}\right)^2} \tag{2.6}$$

where w_0 and the z_R (*Rayleigh distance*) are beam parameters related to the light wavelength through this relationship:

$$\pi \cdot {w_0}^2 = \lambda \cdot z_R \tag{2.7}$$

It is evident that the beam width w depends on the distance, and also on the waist radius and the Rayleigh distance.

Consequently, modeling the beam width with a gaussian profile is a very good assumption in far field, whereas in the near field (that is for the distance lower than the Rayleigh distance) is just a rough approximation.

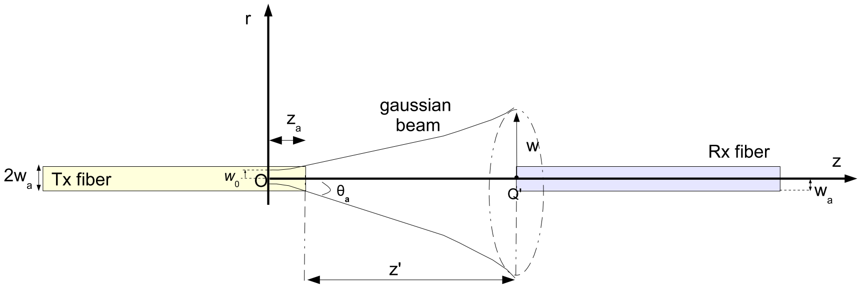

Figure 2.9. Sketch of the equivalent circuit according to the gaussian approach for the sensor arranged in transmission structure.

In the far field, that is $z \gg z_R$, the irradiance of emitted light, that is not constant over beam cross sections, decreases radially (obeying an exponential law) depending on $w(z)$ and r, according to the following equation:

$$I(r,z) = \frac{2 \cdot P_E}{\pi \cdot w(z)^2} \cdot \exp\left[-\frac{2 \cdot r^2}{w(z)^2}\right] \tag{2.8}$$

The beam resembles a spherical wave characterized by the divergence angle θ_a given by:

$$\tan\theta_a = \frac{w(z)}{z} = \frac{w_0}{z_R} = \frac{\lambda}{\pi \cdot w_0} \tag{2.9}$$

In this situation the irradiance expression, see Eq. 2.8, results simplified in:

$$I(r,z) = \frac{2 \cdot P_E}{z^2 \cdot \pi \cdot (\tan\theta_a)^2} \cdot \exp\left[-\frac{2 \cdot r^2}{(\tan\theta_a)^2 \cdot z^2}\right] \tag{2.10}$$

Accounting for that r and z depend on the fiber receiving position, it is possible to evaluate the irradiance as in Eq. 2.10, and thus, the power collected by the receiving fiber can be evaluated integrating the irradiance, over the fiber end surface $S = \pi \cdot w_a^2$.
To calculate the amount of the received power, a first-order approximation about the irradiance can be carried out, considering that it is constant all across the illuminated surface, and equal to its value at the center of the receiving fiber.
Thus, the value of received power for the sensor arranged in transmission structure is reported in Eq. 2.11:

$$P_{RX}(z) = I \cdot S = \frac{P_E \cdot w_a}{z^2 \cdot (\tan\theta_a)^2} \cdot \exp\left[-\frac{2 \cdot r^2}{(\tan\theta_a)^2 \cdot z^2}\right] \tag{2.11}$$

In order to compare the results with the geometrical approach, the power gaussian model has been applied to a sensor in transmission structure composed of two fibers with the same characteristics of the previous case, that is a fiber radius $w_a = 0.5$ mm and NA $= 0.5$, thus obtaining the power ratio shown in Fig. 2.10. Hence, this characteristic is similar to the one obtained with the geometrical model.
Thus, it depends intrinsically on the arrangement in transmission structure, and not from the power model, as demonstrated from the comparison between the two approaches, shown in Fig. 2.11.
It is highlighted that there is not appreciable difference between the two models because the distance dependent term is dominant with respect to others terms composing the optical received power.

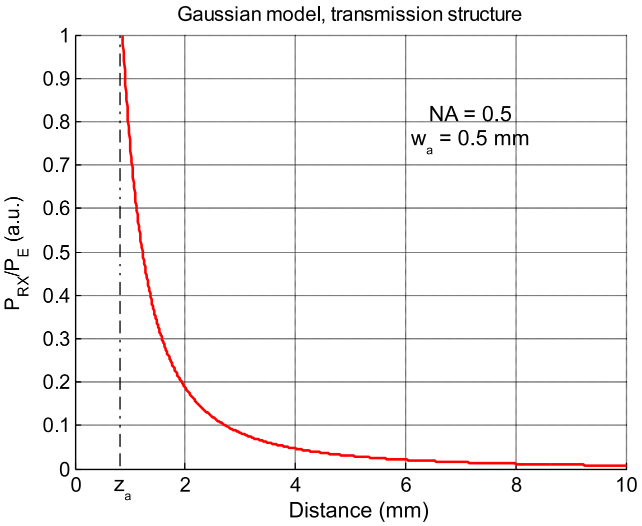

Figure 2.10. Normalized received power according to the gaussian approach for the sensor arranged in transmission structure.

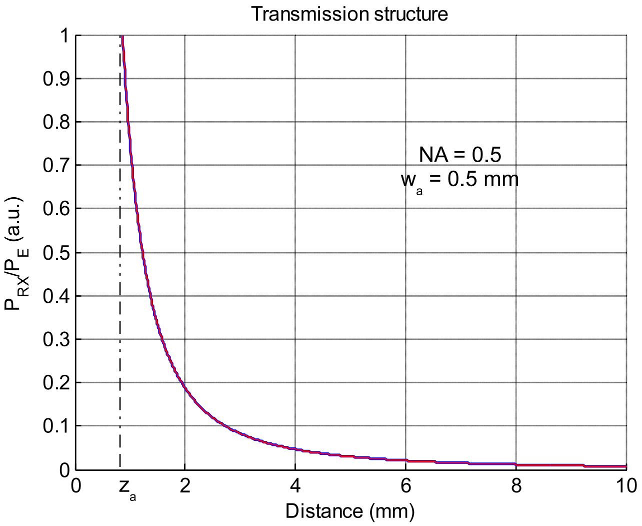

Figure 2.11. Normalized received power respectively according to the geometrical (blue line) and the gaussian model (red line) for the sensor arranged in transmission structure.

Sensor arranged in reflection structure

The analysis of the reflection structure can be performed by using the same approach, distinguishing the geometrical model and the gaussian one.

The sensor structure, with two parallel fibers and a reflecting target placed at a distance z' from the fiber tips, is shown in Fig. 2.12, where the light behavior is considered according to the power **geometrical model**.

Moreover, in this sensor arrangement, the presence of the reflecting target can be modeled considering a receiving fiber "image" beyond the target, on the same axis of the receiving fiber and placed at a distance z' at the opposite side of the target.

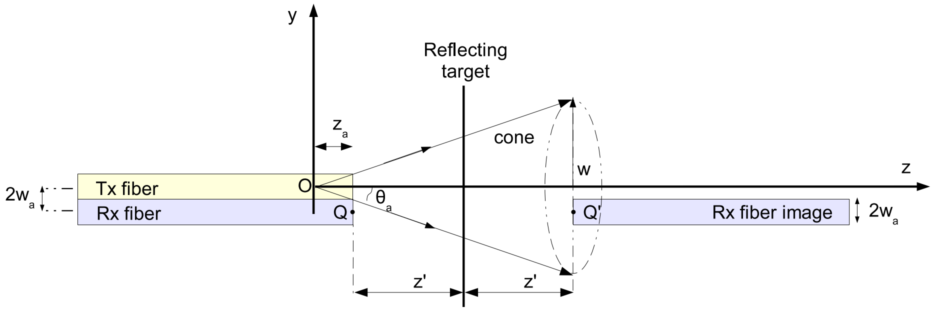

Figure 2.12. Sketch of the equivalent circuit according to the geometrical approach for the sensor arranged in reflection structure.

Since the point Q has coordinates $(y = 2 \cdot w_a; z = z_a)$, the coordinates of Q' are $(y = 2 \cdot w_a; z = z_a + 2 \cdot z')$ and then the total distance to consider in the model is equal to $2 \cdot z'$.

The illuminated area is the overlapping area of two circles, one of radius w, corresponding to the emitted light cone, the second one of radius w_a corresponding to the collecting area of the receiving fiber.

Since the centers of both circles are separated of a distance equal to $2 \cdot w_a$, two cases may occur. The first, occurring for small values of z lower than z_a, when the receiving fiber is partially illuminated, is shown in Fig. 2.13(a). The second, for large values of z larger than z_a when the receiving fiber is totally illuminated, is shown in Fig. 2.13(b).

To find the overlapping area S in the first case, it is necessary to determine the angles α_1 and α_2, as follows:

$$\alpha_1(z) = \arccos\left[\frac{w(z)}{4 \cdot w_a}\right] + \frac{3 \cdot w_a}{4 \cdot w(z)} \alpha_2(z) = \arccos\left(\frac{5}{4}\right) - \left[\frac{w(z)}{2 \cdot w_a}\right]^2 \tag{2.12}$$

Thus, the received optical power in this case is:

$$P_{RX}(z) = \frac{P_E}{\pi} \cdot \frac{w_a}{w(z)} \cdot \left\{\alpha_2(z) - \sin\alpha_2(z) + \frac{w(z)}{w_a} \cdot \left[\alpha_1(z) \cdot \frac{w(z)}{w_a} - \sin\alpha_1(z)\right]\right\} \tag{2.13}$$

Otherwise, when the distance between the fibers is greater than z_a, the receiving fiber is completely illuminated by the light cone, and the received optical power has the following expression:

$$P_{RX}(z) = P_E \cdot \left[\frac{w_a}{w(z)}\right]^2 \tag{2.14}$$

Summarizing, the behavior depicted for the collected power is thus determined by two conflicting mechanisms: the increasing of the effective collecting area and the decreasing of the irradiance as the receiving fiber tips moves progressively away inside the light cone.

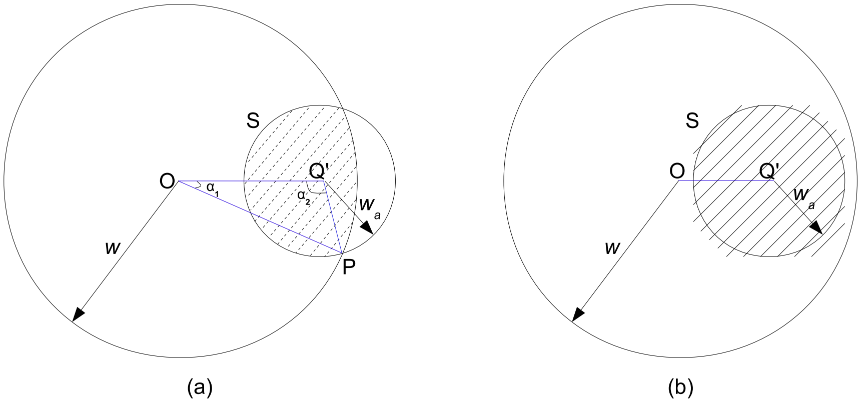

Figure 2.13. The circle of radius ω represents the z−cross section of the light cone. The circle of radius w_a represents the receiving end surface. The shaded area S describes the effective illuminated surface in two cases: partially (a) and completely (b) illuminated.

For small values of z', the first mechanism is predominant, while for high values of z' the second effect dominates on the first.

As example, the power geometrical model has been applied to a sensor in reflection structure composed of two fibers with a radius $w_a = 0.5$ mm and NA $= 0.5$.
The obtained ratio between the received and the input power is shown in Fig. 2.14.

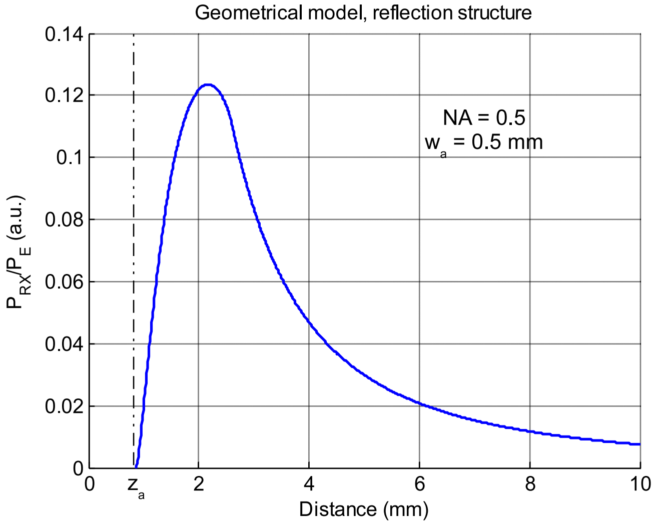

Figure 2.14. Normalized received power according to the geometrical approach for the sensor arranged in reflection structure.

The obtained results show clearly two different regions: the first is on the left of the signal peak

and in this case the power increases with the distance because the increasing of the illuminated area dominates on the decreasing of the irradiance. In the second region, on the peak right, the power decreases with the distance because the dominant effect is the power decreasing with the inverse of the distance square.
It is also evident that the received power peak has a level of about 12% of the input power, while the remaining part of the emitted power is lost.

Considering the light propagation according to the **power gaussian model**, the light wave leaving the transmitting fiber is described as a beam with a gaussian profile.
The equivalent circuit, according to the gaussian approach, for the sensor arranged in reflection structure is shown in Fig. 2.15, where the presence of the reflecting target is equivalent to a receiving fiber "image" beyond the target, on the same axis of the receiving fiber and also placed at a distance z' from the target itself.
According to the Eq. 2.8, the irradiance of the emitted light is not constant over the beam cross sections, but decreases radially obeying an exponential law.

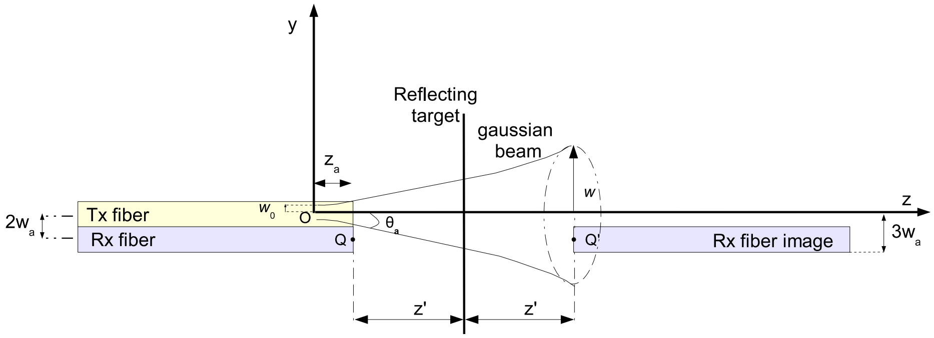

Figure 2.15. Sketch of the equivalent circuit according to the gaussian approach for the sensor arranged in reflection structure.

Considering that the receiving fiber is not in the same axis of the transmitting one, $r = 2 \cdot w_a$.
Hence, substituting this value in Eq. 2.11 and knowing that: $w_a = z_a \cdot \tan(\theta_a)$, it is possible to obtain Eq. 2.15:

$$P_{RX}(z) = \frac{2 \cdot P_E \cdot z_a^2}{z^2} \exp\left(\frac{-8 \cdot z_a^2}{z^2}\right) \tag{2.15}$$

As an example, the power gaussian model has been applied to a sensor in reflection structure composed of two fibers with a radius $w_a = 0.5$ mm and NA $= 0.5$, obtaining the ratio between the received power and the input power that is shown in Fig. 2.16.

Also in this case, the obtained results show clearly two different regions, one on the left of the signal peak where the power increases with the distance and the other, at the peak right, where the power decreases with the distance.
Fig. 2.17 shows the comparison between the geometrical and the gaussian model for a sensor arranged in reflection structure.
The difference between the two models leads to a different peak amplitude, 9% for the gaussian approach instead of 12% of the geometric one. It is also evident that in the gaussian model, when the reflecting target is in close contact with the fiber tips, the amplitude is not exactly null. This

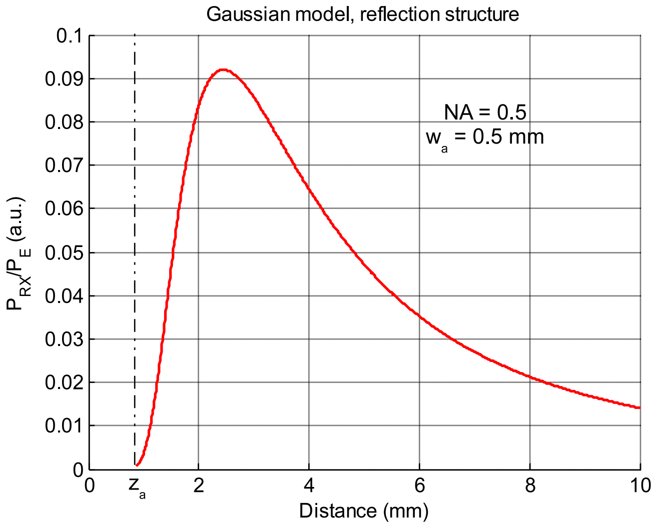

Figure 2.16. Normalized received power according to the gaussian model for the sensor arranged in reflection structure.

discrepancy can be explained because of the Gaussian beam is not confined in the light cone.

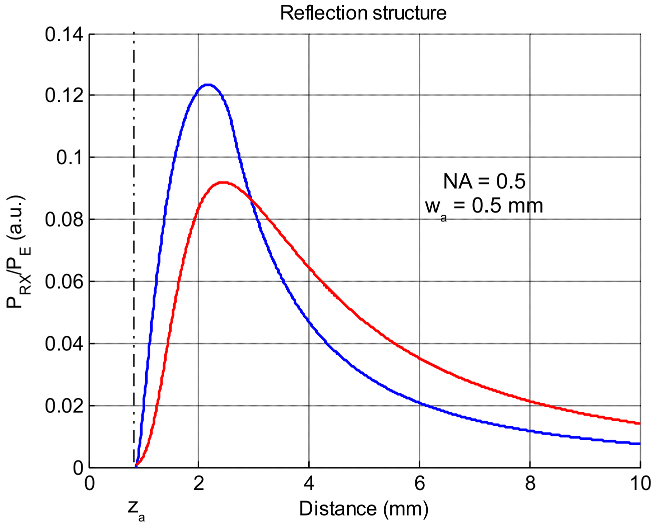

Figure 2.17. Normalized received power according to the geometrical (blue line) and the gaussian model (red line) for the sensor arranged in reflection structure.

Fig. 2.18 shows the comparison between the sensor arranged respectively in transmission and in

reflection structure, where it is clear that the received optical power is higher for sensor arranged in the transmission structure.
Anyway, the reflection structure can be realized in a more compact way since both fibers are at the same side. For this, the proposed displacement sensor able to detect the crack evolution along one-axis is realized in reflection structure.

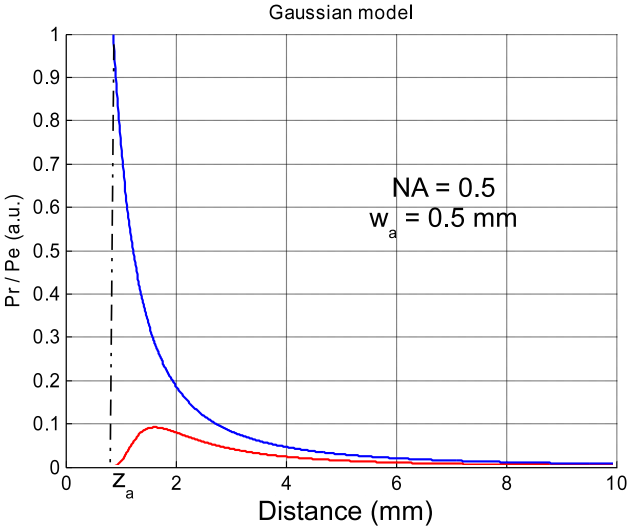

Figure 2.18. Normalized received power according to gaussian model evaluated for the sensor arranged in transmission and in reflection structure respectively.

2.3 A displacement sensor for monitoring crack evolution in two directions (2D)

In structural monitoring applications, some situations exist where it can be difficult predict the direction of the crack evolution.

In these cases, the proposed sensors detecting the displacement along one axis (1D) do not provide enough information.

So, the feasibility of a compact 2D displacement fiber sensor has been investigated.

The proposed two-dimensional (2D) plastic optical fiber sensor resembles a typical commercial mechanical crack monitoring device, composed of two plates that can slide one on the top of the other where a reference crosshair is engraved on one plate and a grid on the other, such as shown in Fig. 2.19.

The proposed optical solution is a numerical aperture sensor arranged in transmission structure where the receiving fiber is replaced with a bundle of three fibers to allow the measurements along two directions.

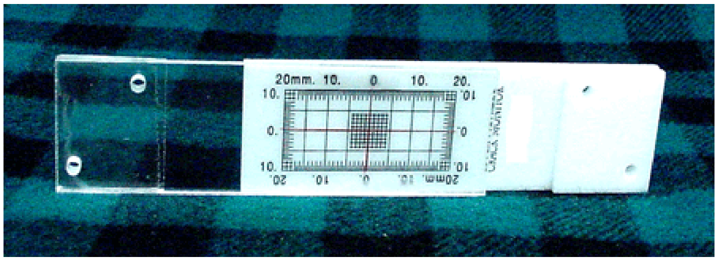

Figure 2.19. A commercial mechanical crack monitoring device able to monitor the crack evolution in two directions.

Also the fibers are embedded in two plastic plates, designed to be fastened at the sidewalls of the crack, whose displacement has to be monitored, that are superimposed and can slide along two dimensions according to the crack evolution.

One of the plates embeds a transmitting fiber while the other embeds the bundle of receiving fibers arranged to form the displacement sensor, whose scheme is shown in Fig. 2.20.

This configuration exploits the transmission structure properties described before and by means of the gaussian model, it is possible evaluate the received power at each receiving fiber when the transmitting one lights them.

Fig. 2.21 shows in further detail the proposed configuration, when a transmitting fiber is facing to a bundle composed of the three receiving fibers embedded inside one of the plates composing the sensor.

When the upper and lower parts of the sensor are aligned, the axis of the transmitting fiber is facing the center of mass of the receiving fiber bundle, as shown in Fig. 2.22, and the detected power at the three receiving fibers is equal.

The idea is to identify the relative displacement (amount, direction and versus) between the two plates exploiting the comparison of the readings of the three received power levels, in a similar way to that employed in one-dimensional intensity-based displacement sensors.

To evaluate the sensor behavior, some simulations have been carried out, taking account that the received power from each fiber is a function of the relative position with respect to the transmitting fiber.

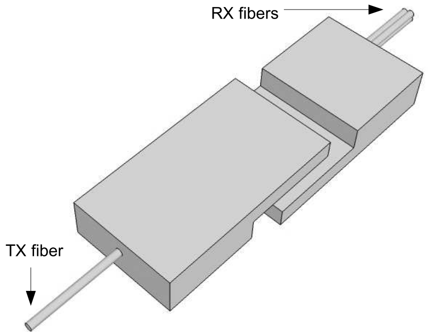

Figure 2.20. A schematic representation of the proposed sensor.

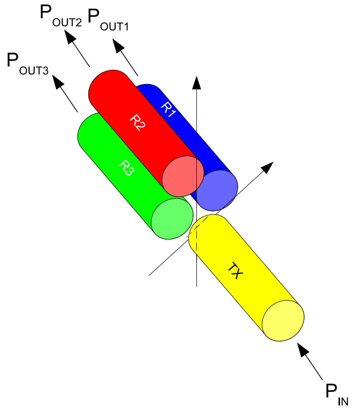

Figure 2.21. A representation related to the fiber inside the sensor: the transmitting fiber (yellow cylinder) is facing to a bundle composed of three receiving fibers (represented from red, blue and green cylinders).

Hence, the sensor response can be computed using models based on geometrical considerations, obtaining a representation such as shown in Fig. 2.23.

Some simulations have been carried out normalizing the displacements to the fiber radius and

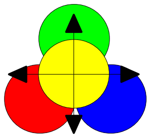

Figure 2.22. A front view of the transmitting (yellow circle) and receiving (red, blue and green) fibers.

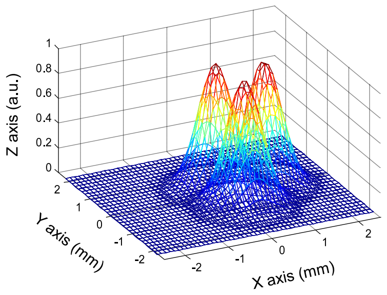

Figure 2.23. Simulation of the normalized sensor response.

considering the received power intensity as unitary if the transmitting and the corresponding receiving fiber is perfectly overlapped.

An example of the resulting received power versus transmitting fiber position for the receiving fibers is reported in Fig. 2.24, confirming that the peaks intensity is located in different positions of the plane according to the fibers position. Fig. 2.25 shows instead the results obtained having simulated an horizontal and a diagonal (45°) displacement from the position of null displacement, respectively. In both cases, the corresponding power variations of the three receiving fibers are

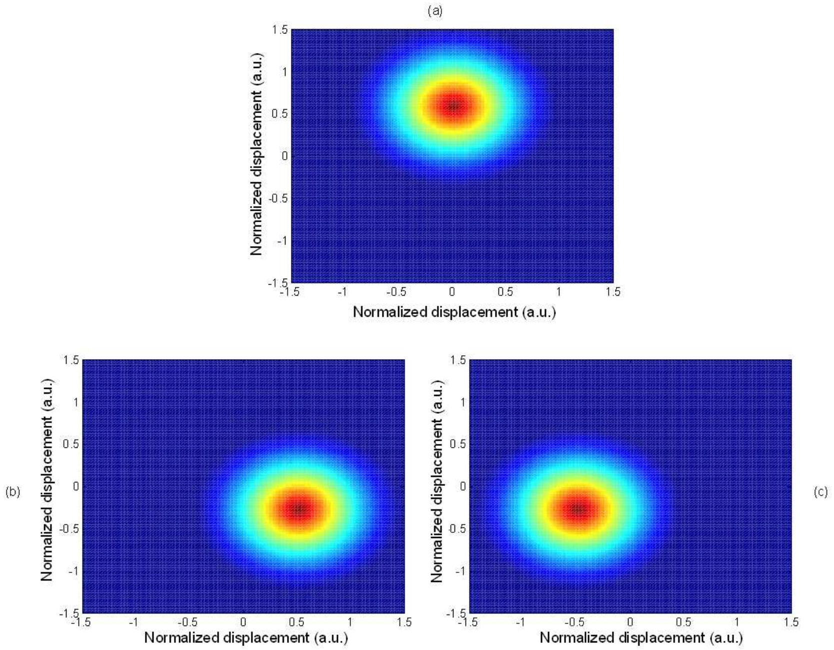

Figure 2.24. Simulation of the expected readings from the receiving fibers versus transmitting fiber position, having normalized the displacements to the fiber radius.

shown.

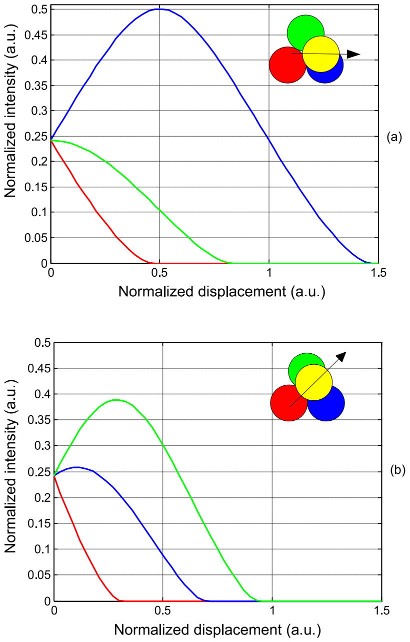

Figure 2.25. Simulation of the expected readings for an horizontal (a) and a diagonal (b) (45°) displacement.

Chapter 3

Displacement sensor realization

Some sensor displacement prototypes have been developed and employed to measure the displacement along one and two axes.
The activity has also concerned the development of systems for the optical interrogation of the sensors and for the automatic acquisition of the sensor outputs.
This chapter describes some of the sensor embodiments, the structure of the interrogation systems and also provides the results obtained during the sensor characterization as well as the ones obtained during in-field tests.

3.1 Sensor practical arrangement

The proposed optical sensor to measure the displacement along one direction is arranged in a reflection structure employing, as reflecting surface, a mirror placed at a certain distance d from the fiber tips, as shown in Fig. 3.1.
In addition, a suitable mechanical embodiment, surrounding the sensor, has been designed as a sliding structure, in order to maintain the fibers in a fixed position leaving the part containing the reflecting surface free to move along the fiber axis.
This embodiment protects the optical part of the sensor, since the sensor has to be placed across the crack under monitoring. Fig. 3.2 shows how the sliding structure, specifically conceived to measure the crack evolution, moves when the crack width increases.

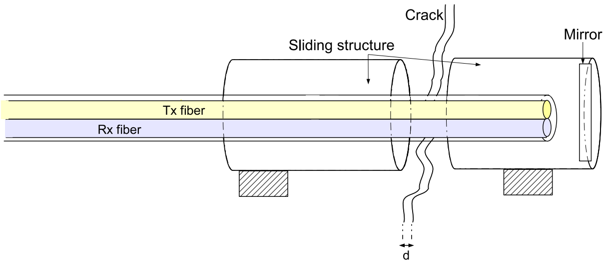

Figure 3.1. Fiber displacement sensor working principle with the protective embodiment designed to detect the crack evolution.

According to the gaussian model, it is possible evaluate the distance variations with the optical

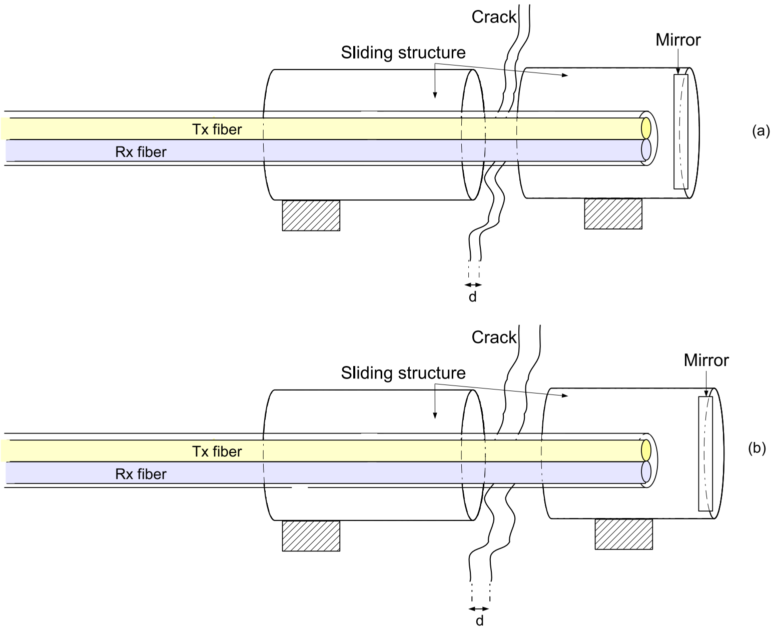

Figure 3.2. Examples of the sliding structure behavior according to the crack evolution.

power variations, taking into account that the received optical power depends on the input optical power, on the divergence angle of the light cone and the on the distance d. In this case the distance is considered between the fiber tips and the mirror, that means to consider a null distance when the fiber tips are in contact with the mirror. The typical optical response with the distance, evaluated according to the theoretical model and expressed in term of percentage of normalized received optical power, is reported in Fig. 3.3, where two working regions, namely R_1 and R_2, can be recognized.

In the region R_1, the sensor working range is rather limited, but the sensitivity is higher than in the region R_2.

Then, it is better employ the sensor in the region R_1, if the expected crack width variations are not so extended, such in the case of a short-term monitoring, whereas it is better employ the sensor in the working region R_2 if the expected displacements are larger than 2 mm because of a greater range, such as in a long-term monitoring.

3.2 Sensor prototypes and experimental setup

The sensors have been developed according to the structure reported in Fig. 3.1.

Indeed, different types of prototypes, shown in Fig. 3.4, have been realized in order to know what is the best mechanical embodiment.

The structure surrounded the optical sensing part is composed of two sliding metallic cylinders, that protect the sensor against the dirty and ambient light.

Since the distance d is related to the amount of the received power, there is a distance limit beyond which the optical power level and the sensor sensitivity become too low to appreciate larger

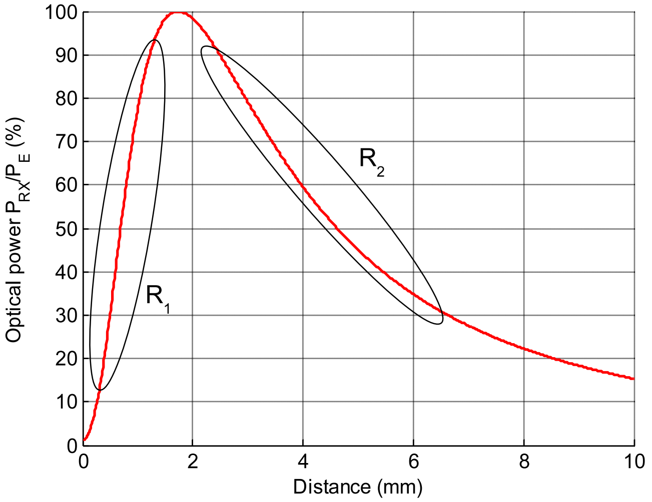

Figure 3.3. Optical response dependence with the distance.

displacements than this limit.
According to the gaussian model, this maximum distance is fixed in $d = 10$ mm.
The employed fibers are standard POF with PMMA core surrounded by a fluoropolymer cladding having a 0.5 mm diameter, with or without jacket.

Figure 3.4. Different realized sensor prototypes.

Indeed, the jacket guarantees more protection for the fiber span not protected from the embodiment. Fig. 3.5 shows one of the prototypes installed on a cracked stone to verify the feasibility of the fixing technique and mechanical arrangement.

Also, a measurement system has been developed to detect the fiber sensor output.
Fig. 3.6 shows a block diagram of the interrogation system that includes transmitter, sensitive part and receiver.
The transmitter contains a red commercial led fed through a constant current.
It is possible to use a commercial non−coherent source because the plastic fibers are multimode and have an higher numerical aperture and higher diameter than silica fibers.

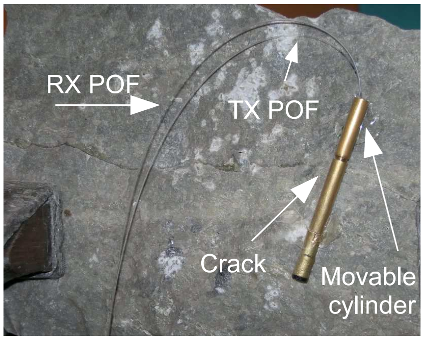

Figure 3.5. Sensor prototype installed on a cracked stone to verify the feasibility of the fixing technique and mechanical arrangement.

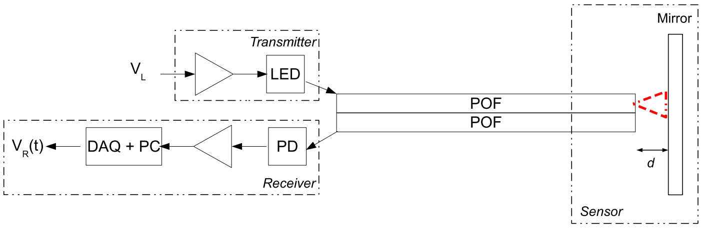

Figure 3.6. Measurement system: transmitter, sensitive part and receiver.

Also, they contributes to maintain low the system costs.

The receiver is basically composed of a photodiode, that convert the light to a photocurrent, followed by a transimpedance amplifier, with a suitable gain related to the expected optical power input. The amplifier output can be acquired by a commercial data acquisition board connected with a PC or in alternative from a microcontroller.

Anyway, the data elaboration is realized through a dedicated acquisition program developed in “visual basic .net” language.

In detail, the expression of the received voltage V_R measured at the receiver output can be written as in Eq. 3.1 [15]:

$$V_R = A \cdot v_L \cdot \frac{P_R(d)}{P_T} \tag{3.1}$$

where $\frac{P_R(d)}{P_T}$ is the optical power response according to the gaussian power model written in Eq. 2.15, v_L is the voltage applied to the LED, and the term A takes into account all the factors that are constants because independent from the distance d, like the amplifier gain for the electronic part, the LED efficiency and the photodiode responsivity, the mirror reflectivity and the fibers attenuation.

3.3 Sensor characterization

The sensor response shown in the previous chapter has been obtained using a theoretical optical model and it is based on the hypothesis that all the optical component, fibers and mirror, have an ideal behavior.

Anyway, the response of real sensors is rather different than the expected one mainly because fibers and mirror can be not perfectly aligned and eventually fibers present some imperfections.

For these reasons, to obtain the best result, each sensor has to be characterized before its use.

The characterization has been carried out simply applying known displacement to the movable part of the sensor and simultaneously measuring the received voltage at the receiver output.

In this way it is possible to evaluate the relationship between the received voltage and the displacement in the entire range, thus obtaining the sensor calibration curve.

An experimental setup has been arranged exploiting two commercial linear stages, produced by Thorlabs, in order to simulate the crack evolution: the first stage is motorized, with a working range of 25 mm and a resolution of 0.1 μm, thus allowing known displacements be applied to the movable part of the sensor.

The second stage is manual and it is employed to maintain the fiber tips in a fixed position.

A detail of one sensor prototype subjected to the characterization is shown in Fig. 3.7, where it is possible observe the sensor positioned between the two stages and two plastic fiber spans, that are respectively connected with the transmitter and the receiver shown in Fig. 3.8, exploiting a microcontroller to acquire the detected signals.

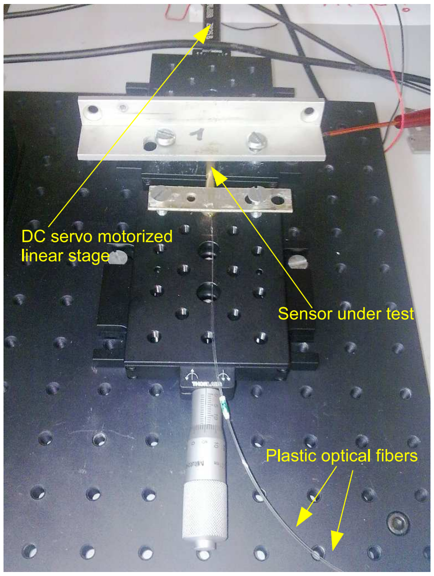

Figure 3.7. Experimental setup arranged to characterize the sensor prototypes.

Several experimental tests to characterize the sensor prototypes have been carried out in a distance range of 5 mm.

Thus, the characteristic curve of each sensor has been subdivided in a set of intervals, N_{int} and each interval has been linearized.

Using this approach, the distance can be obtained from the sensor output exploiting simple linear models and it is also suitable to be implemented in the microcontroller having a reduced computational power.

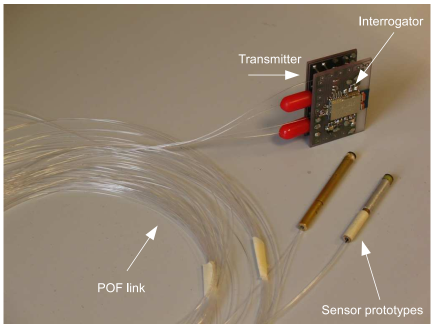

Figure 3.8. Sensor prototypes connected with the interrogation system.

The choice of the number of intervals N_{int} affects the sensor uncertainty because a large N_{int} corresponds to a small linearity error but this increases the amount of microcontroller memory required to store the linearized intervals.
Fig. 3.9 shows the calibration curve subdivided in N_{int} = 20 and N_{int} = 5 segments respectively.

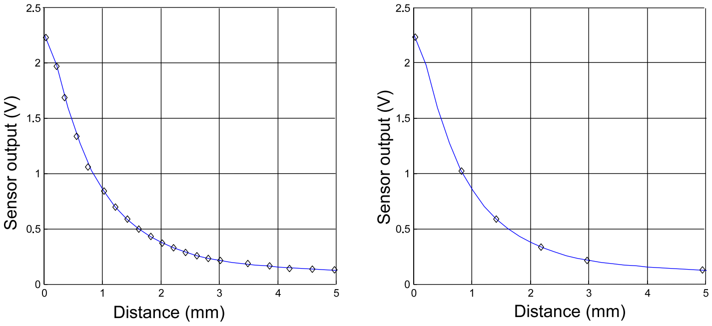

Figure 3.9. Sensor prototype output subdivided in N_{int} = 20 (a) and N_{int} = 5 (b) segments respectively. Larger is N_{int}, lower is the non-linearity error

.

Experimental tests have been demonstrated that N_{int} = 20 allows to maintain the linearity error below to 5 μm, while using N_{int} = 5 the linearity error is of about 50 μm.
Fig. 3.10 shows the calibration curve obtained for the sensor prototype considering N_{int} = 20 segments.
Since the sensor is working in the region R_2, the sensitivity decreases, in absolute value, with the distance, as expected.
As an example, the sensitivity at d=2 mm is of about S = -0.5 V/mm whereas at d=5 mm it is about S = -0.05 V/mm.

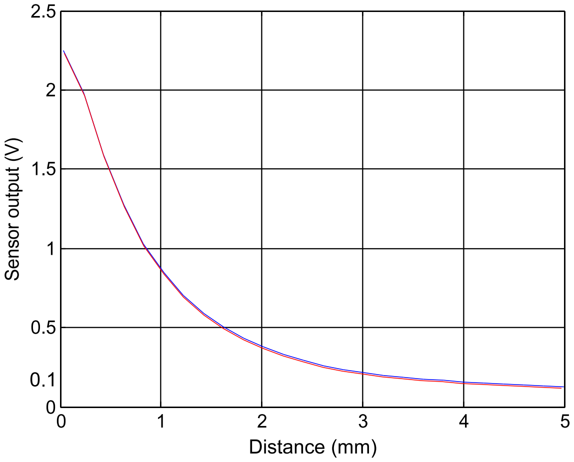

Figure 3.10. Calibration curve of the sensor prototype obtained through lookup table technique employing $N_{int} = 20$ segments. This curve (red curve) is overlapped to the sensor output curve with the distance (blue curve).

3.4 Acquisition system for long term crack monitoring

A low cost acquisition system, whose block scheme is shown in Fig. 3.11, has been designed to allow the remote monitoring of up to eight sensors in a prestigious XVI-century building in Venice [16].

The developed system is able to monitor up to eight of the developed displacement fiber sensors and also provides the acquisition of traditional commercial temperature and humidity sensor outputs in order to monitor the environmental conditions.

The fiber sensors have been arranged following the scheme exploited to realize the first prototypes, employing plastic optical fibers having a step index refractive profile, a PMMA core and a 1 mm diameter.

Fiber sensors were connected, through an optical link of about 10 m length, to the correspondent conditioning circuits, realized with the same scheme of the demonstration setup, and they also have been placed in a fire proof container.

One of the eight sensors, surrounded by a suitable support having a negligible thermal expansion, has been blocked in a fixed position, very close to a working fiber sensor in order to detect the signal variations due to environmental conditions instead of the crack displacement, like as highlighted in Fig. 3.12.

In this way, the sensor, forced to have null displacement, namely *"reference"* sensor or *"null"* sensor, can be employed to evaluate how the environmental conditions effect on the fibers behavior during the monitoring.

The acquisition unit, located in the same fireproof box with the transmitter and receivers, is basically composed of an embedded PC and a GPRS modem. In detail, the PC is a FOX board, running a Linux operating system, that manages analog to digital conversion, stores the acquired data in a local Secure Digital (SD) memory card of 1 GB, and also enables the GPRS modem and is able to send, once a day, the stored data to a remote web server located in Torino.

An experimental long term monitoring over more than one-year has been carried out in Venice and the obtained results are shown in Fig. 3.13. The upper curve is the working sensor response while the lower is the response of the same sensor after the compensation accounting for the "null"

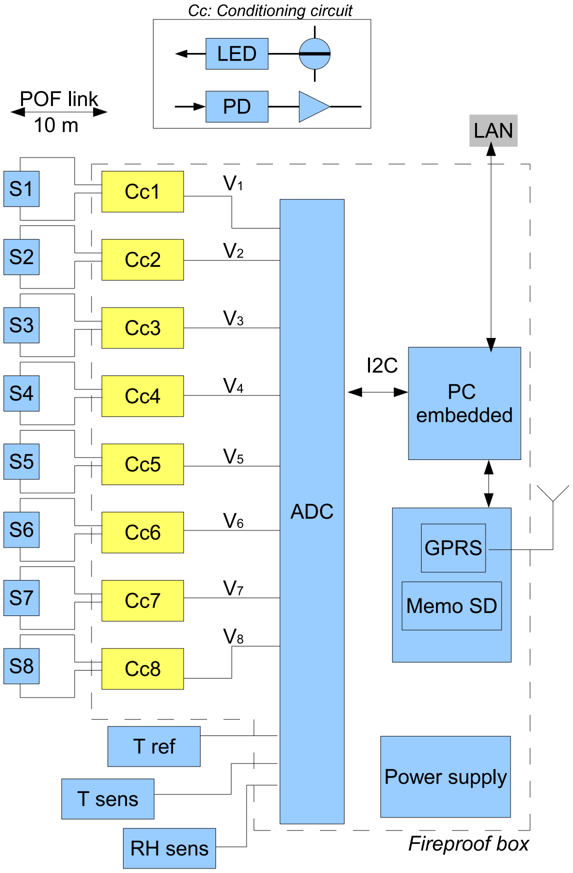

Figure 3.11. Block scheme of the acquisition system designed for a real time crack monitoring.

sensor response.

The experimental results confirm that in the short-term monitoring (days), the environmental condition affect both the optical sensors and hence the used compensation is effective.
On the contrary, in the long term, the unwanted drift can not be related only to the environmental conditions effects, therefore the *"null"* sensor can not be employed for the correction purposes.
The reason of this unwanted drift is the aging of the fiber, mainly due to the degradation of the fiber material (PMMA) because of the temperature and humidity. [1].

The fiber ageing issue, also known in literature [18], [19], is the main drawback of the intensiometric numerical aperture sensors and for this, it has been further investigated.

---

[1] The work described in this section is also published in [17]

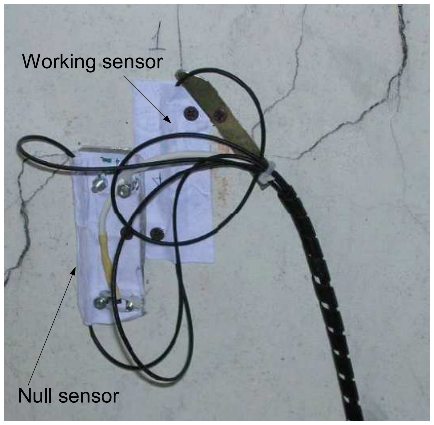

Figure 3.12. Optical sensors installed in Venice during the long-term monitoring: the leftmost is the reference sensor while the other is the crack working sensor.

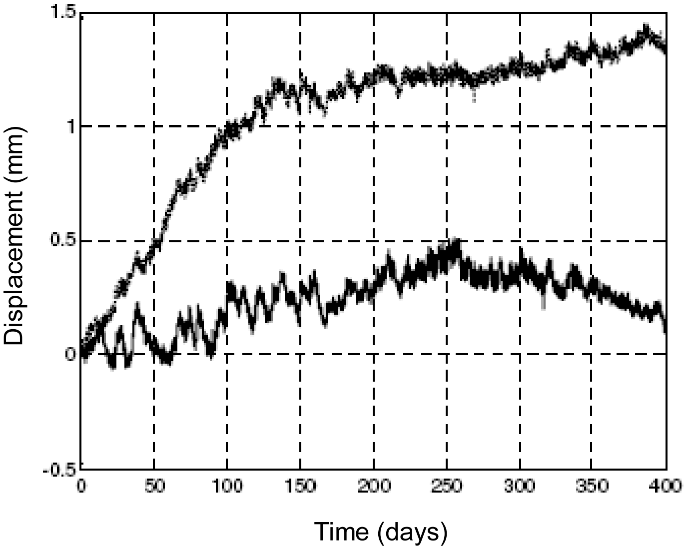

Figure 3.13. A displacement measurement across a crack during a long term monitoring of about 400 days: the upper curve is the response measured from the working sensor, while the lower curve is the displacement measurement after the compensation carried out with the reference sensor.

3.5 Sensor practical arrangement for 2D displacement sensor

To arrange the sensor able to measure displacement along two directions, the fibers can be embedded into two plates horizontally and cut to deflect the light by 90° with a metered angular cleave.

On the contrary, if the plate thickness is not a primary concern, the metered cleave in the fibers can be avoided by using a multicore plastic fiber that allows much narrower curvature radii without significant increase of loss.
Moreover, the employment of multicore fibers has the further advantage to reduce the sensor sensitivity to external disturbances, such as the fiber bending, an interesting property when the sensor is employed in long-term monitoring applications.
To realize this structure, based on two sliding plates, the selected fibers have to be positioned in a small empty box with the help of adhesive tape strips, and a liquid resin poured into the box and cured to permanently embed the fibers.
Finally, the plates can be polished to get flat surfaces, with the transmitting fiber tip that can be slightly retracted with respect to the surface itself and the receiving fiber tips at the same level of the surface, since this solution enables an increment of the sensor working range.
Also, in order to limit the effect of stray light, that produces crosstalk among the receiving fiber, the fiber receiving tips have to be laterally covered with black paintings.
A first simplified prototype has been built following the scheme of Fig. 3.14, employing step index PMMA fibers with 1 mm diameter, in order to maintain the costs low, since the first aim of this prototype is to demonstrate experimentally the feasibility of the sensor working principle. The three receiving fiber tips were laterally covered with black paintings to avoid crosstalk.

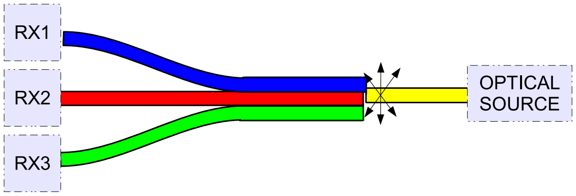

Figure 3.14. Simplified sensor scheme.

The tip of the transmitting fiber has been embedded in a polymeric block, while the receiving fibers tips have been fixed in an another block of the same polymeric material. The obtained prototype is shown in Fig. 3.15. The measurement system is shown in 3.16, where the transmitter

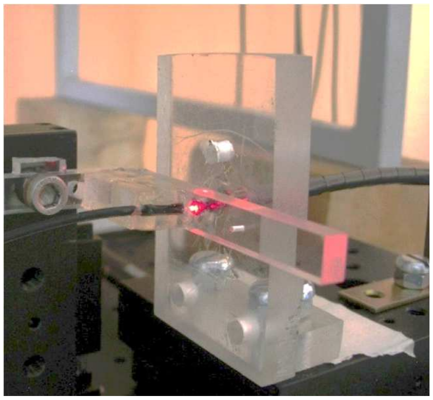

Figure 3.15. Simplified 2D fiber sensor prototype.

is a red LED source driven with a modulated current signal at $f_s = 315$ Hz, in order to allow a synchronous detection to reduce the effect of noise, while the three receivers employ circuits with photodiodes connected to transimpedance amplifiers followed by data acquisition board and *PC* to analyze the acquired data.

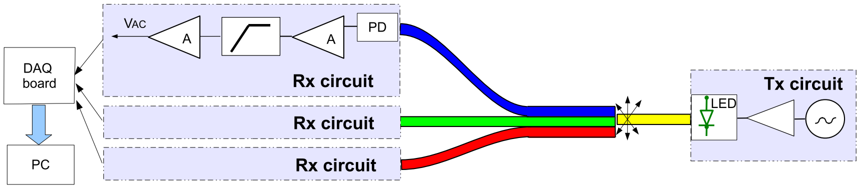

Figure 3.16. Scheme of the setup arranged to test the 2D sensor prototype.

In order to obtain the displacement in the plane, the block that contains the transmitting fiber tip has been properly fixed on a computer-controlled precision linear translation stage, which is mounted on a second stage in order to control the transmitting fiber position in both directions with an uncertainty of 10 μm, while the receiving fiber block has been maintained in a fixed position. The arranged setup is shown in Fig. 3.17.

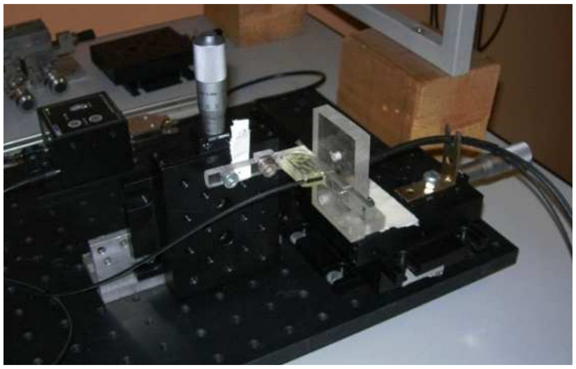

Figure 3.17. Demonstration setup arranged to test the 2-D sensor prototype.

3.6 2D sensor characterization

The sensor prototype characterization has been carried out moving the transmitting fiber block in a region of the plane between -2 mm and +2 mm in 0.1 mm steps, obtaining for each fiber the correspondent acquired voltage, as shown in Fig. 3.18.

Indeed, the calibration procedure is more complex than the one employed for the 1D displacement sensor, since here the position of the fiber on the plane (x,y) has to be obtained from the signals related to the three receiving fibers.

The method employed to measure the position is similar to the one used in navigation systems, such as GPS. The obtained signal intensity from a fiber corresponds to a curve on the plane, that is, all the points belonging to this curve produces the same signal level. So, the received voltages

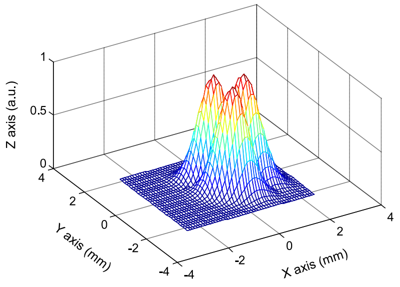

Figure 3.18. Normalized experimental data obtained during the characterization.

from the three fibers define three curves whose intersection is the position of the transmitting fiber. In particular, considering the fibers without imperfections, the curves are perfectly circular, and the position of the transmitting fiber can be mathematically obtained solving the intersection of the three circles.
Indeed, with only one fiber, the relative displacement would belong to the related first curve, with two fibers there would be an ambiguity because of two possible intersections, whereas with three fibers there is only one intersection, that is the transmitting fiber position in the plane, such as shown in Fig. 3.19.

To implement the calibration procedure, a fitting of the received voltages, obtained during the calibration test, has been performed considering that the light intensity emitted from the fiber has a gaussian shape.

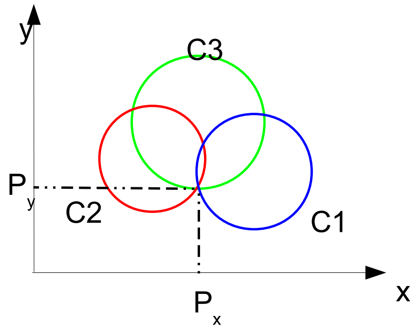

Figure 3.19. The estimation of the transmitting fiber position P(x,y) is detected by the intersection of the three constant power curves.

The employed fitting function is, therefore:

$$v_{out} = a_1 \cdot \exp\{a_2 \cdot [(x - a_3)^2 + (y - a_4)^2]\} + a_5 \tag{3.2}$$

where x and y represent the coordinates in the plane, while a_1, a_2, a_3, a_4,a_5 are constant terms. In particular, for each fiber, a_1 is the received signal peak value, a_2 is the gaussian width, a_3 and a_4 are the gaussian peak coordinates (respectively along x and y), and a_5 is the voltage offset. The fitting procedure has produced a negligible difference with the experimental data.

Since v_{out} is known because it has been measured during the characterization, Eq. 3.2 allows to define a circumference with the expression reported in Eq. 3.3:

$$x^2 + y^2 - 2 \cdot a_3 \cdot x - 2 \cdot a_4 \cdot y + (a_3^2 + a_4^2 - 1/a_2) - \ln((v_{out} - a_5)/(a_1)) = 0 \tag{3.3}$$

from which parameters of the three circumferences for the three fibers can be computed. So, the intersection of three curves can be found solving the equations two by two, in order to find the point P(x,y) that satisfies the condition to belong to the three circles.
In this way, measuring v_{out} related to the three receiving fibers, it is possible find the estimated position of the transmitting fiber in the plane.
Fig. 3.20 shows the three bidimensional gaussian shapes obtained from the three fibers during the characterization.

As an example, Fig. 3.21 shows the three curves represent the correspondent received voltage levels when the transmitting fiber is in $P(x,y) = (0, -75) \ \pm 5 \ \mu$m.

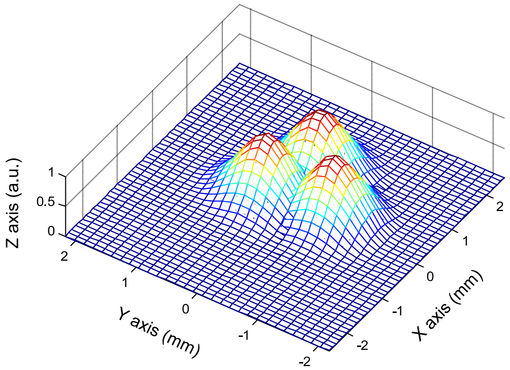

Figure 3.20. Bidimensional gaussian fitting of the experimental data concerning the three fiber outputs.

The intersection becomes an area due to the residual model error.
Fig. 3.22, shows an enlarged view of the intersection point, where it is possible observe this area. It is also evident the agreement between P, that is measured with the translation stages, and P_m that is the center of the area obtained with the intersection of the three circles, shown in Fig. 3.21.
In the full range of the sensor, the difference between the position measured from the stages and that evaluated according to the proposed measurement procedure is shown in Fig. 3.23. It is also highlighted that closer is the transmitting fiber to the center of the receiving bundle, smaller is this error. In particular, the sensor working range is between -0.5 mm and 0.5 mm and the related maximum error is lower than ±35 μm. [1]

---

[1] The work regarding the feasibility of the proposed 2D displacement sensor is published in [20].

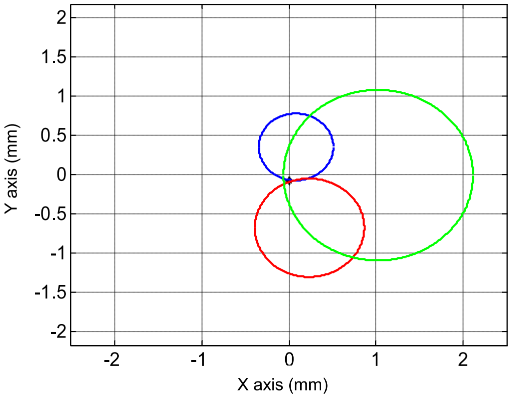

Figure 3.21. Example of the three corresponding circles obtained from the measured signals from the three receiving fibers.

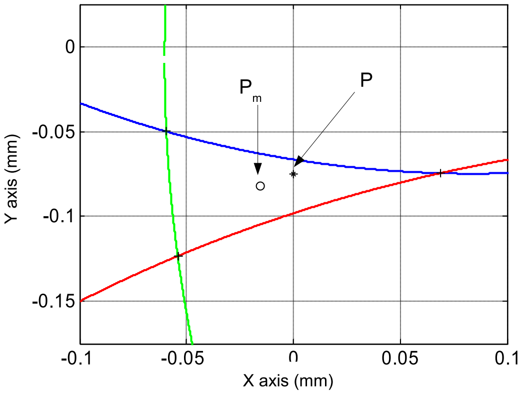

Figure 3.22. Zoom of Fig. 3.21: the intersection of the three curves is an area due to the model error and noise.

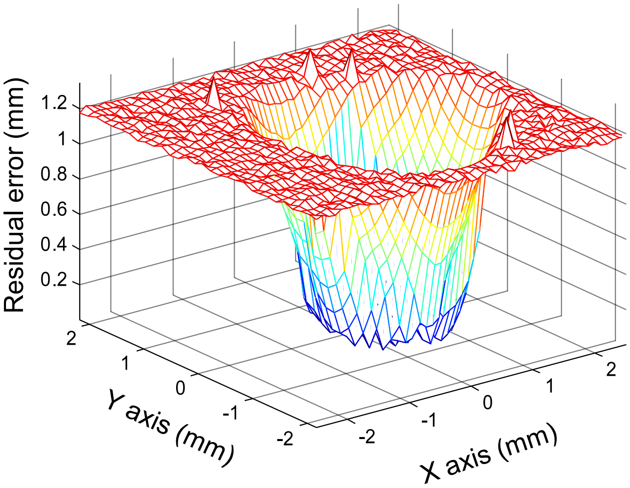

Figure 3.23. Residual error between the nominal and measured values.

Chapter 4

Sensor stability issues

The light intensity received from the intensity variation sensors depends not only from the measured displacement, but also on the other quantities such as the fiber attenuation and the stability of source and receiving circuits.
In principle, it is possible to calculate those fluctuations by estimating the system optical power budget, considering source fluctuations, fiber attenuation for length, photodetector behavior and connector losses.
In particular, the behavior of the source (LED) and of the photodetector (PD) can be modeled using the parameters provided by manufacturers, although these do not allow achieving good results, because they are not specific for the proposed purposes.

On the contrary, the attenuation of multimode plastic optical fiber is hard to model because it depends not only from the fiber length,but also on unwanted effects not easily controllable in predictable way.
These undesired effects, that have been already studied in literature [18], usually through experimental tests, can be identified as follows:

- **mode dependent attenuation**: depends on the path difference between the rays that travel along the fiber (because the difference between a ray propagating parallel to the fiber axis and another propagating close to the critical angle of total reflection can become quite large). It is known in literature that for SI-PMMA fibers, such as those employed for the developed sensors, this effect introduces about 1 dB each 100 m of fiber length. Hence, accounting for that the fiber length necessary for the proposed sensor is much shorter and the attenuation due to the fiber length is strongly predominant, this effect can be considered negligible.

- **mode coupling** between modes propagating in the fiber: this effect can be reduced using to feed the sensor fiber spans where the Equilibrium Mode Distribution (EMD) condition has already been obtained. (EMD means to reach a steady state distribution where the mode distribution remains constant). Considering SI-PMMA fibers, this happens for fiber length over than 100 m. Since the fiber composing the proposed sensor is shorter, it is possible to reach EMD conditions for shorter fiber span insert "*mode scrambler*". (The "mode scrambler", also namely "mode mixer", is a device able to achieve the EMD conditions in order to have at its output the modes dependent attenuation (mode coupling, conversion and dispersion) independent from the fiber lenght.

- **scattering losses**: they depend mainly on the imperfections caused by the fiber manufacturing process. They are estimated in literature as a function of the wavelength incident on the fiber material. Since this effect is evaluated in the order of some decibel/kilometers, it can be considered negligible for the proposed sensor.
- **attenuation depending on the fiber material**: this contribution is due to degradations in the materials composing the fibers. Since different polymeric chains can be corrupted in different ways if subjected to the same perturbations, it is necessary to know the fiber material and its behavior with temperature.
- **fiber bending**: the fiber bending sensitivity depends on the fiber diameter and the numerical aperture. The larger the NA, lower is the minimum allowed fiber curvature radius. The minimum fiber bending radius is an information always present in commercial fiber datasheets because when the fiber curvature radius is lower than limit, the bending losses becomes very high, otherwise can be considered negligible with respect of other attenuation effects.
- **environmental conditions** effects: in general this contribution can be due to mechanical, climatic, chemical, biological and radiometric conditions [19]. Since the developed sensors is expected to be employed in industrial environmental mainly influenced by climatical effects, temperature and humidity effects are the most important to be further studied.

Anyway, the stability issues of the developed fiber displacement sensors are particularly relevant in long-term monitoring.
For this reason, some experimental tests have been carried out in order to verify experimentally the stability effects on the sensor performance.

4.1 Fiber stability test

The test aim is to verify experimentally the behavior in real conditions of two SI-PMMA fiber spans nominally identical, such as those employed to realize the proposed sensors.
The developed acquisition system, employed for each span, is schematized in Fig. 4.1. The employed source is driven with a constant current and connected with a fiber span arranged to form a "*mode scrambler*", that makes the power losses caused by modes attenuation independent from the fiber length. Also, the fiber bending radius is maintained larger than the permitted minimum radius in order to have negligible bending losses.

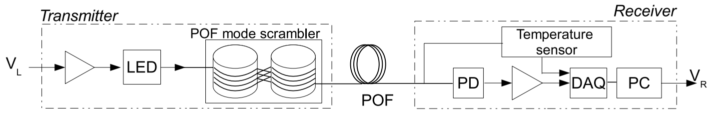

Figure 4.1. Acquisition system developed to perform the fiber stability test.

At the mode scrambler output, the fiber span is connected to the photodiode followed by a transimpedance amplifier that converts the photocurrent in an amplified signal. This output signal is acquired by means of a data acquisition board (configured to measure also a temperature in order to evaluate the temperature of the fiber) connected with a PC that stores and elaborates the received data.
Considering the test aim, the choice of electro-optical devices is not critical, and also their behavior can be considered in the power budget.
In this case, the employed source is a red led centered at the wavelength of 645 nm with a spectral bandwidth of 15 nm. The attenuation for fiber unit length is nominally 0.15 dB/km but can increase up to 0.35 dB/km due to the spectral bandwidth and to the fiber spectral attenuation.
The employed photodetector is a commercial photodiode with a responsivity of 0.44 A/W in red wavelengths.
Each fiber span is composed of a standard plastic optical fiber with step index refractive profile, PMMA core and fluorinated cladding, with a diameter of 1 mm and a length of 10 m, cut from the same spool.
Hence, it is possible to estimate the fiber attenuation losses in order to design the electronic conditioning circuit more stable than the expected fibers behavior.

At this point, employing the proposed acquisition system, two fiber spans, namely $F1$ and $F2$ respectively, have been tested for about one year (370 days) at the room temperature.
Fig. 4.2 shows the results obtained experimentally measuring the two fibers outputs each 5 minutes, and also the relative variations of the fibers outputs having fluctuations up to ± 3%.
Unfortunately, it also highlights a different behavior of the fibers despite they have the same characteristics and are produced by the same manufacturer.
In order to verify the effect of the temperature on the fiber response, the temperature of the fiber spans has been measured during this stability test, as shown in Fig. 4.3.
The fibers behavior is partially related to temperature variations and this behavior is confirmed by the experimental results that have shown the fluctuations due to the environment.
Anyway, F1 and F2 shows two different responses, especially in the first 100 days.
Therefore, the environmental conditions influence the fiber aging as expected, but it is only one of the effects acting on the fibers behavior variations.

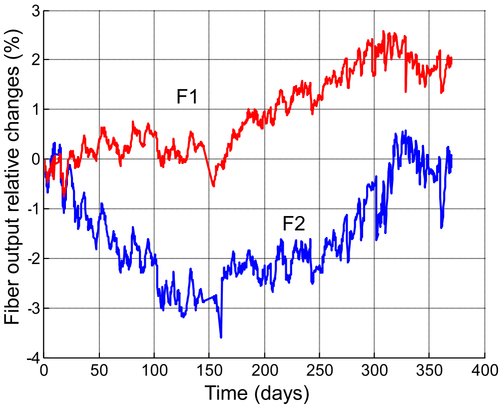

Figure 4.2. Fiber output relative changes recorded during a test of two fiber spans nominally identical for a period of about one year. The change is mainly due to the fiber attenuation.

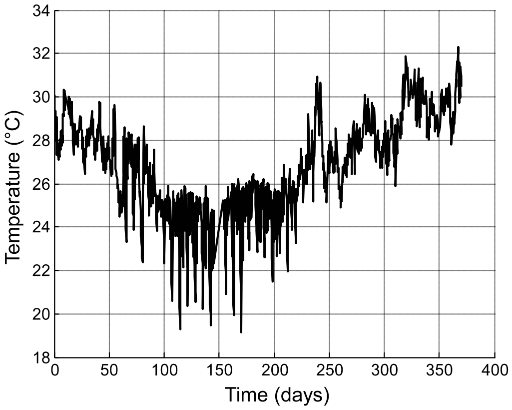

Figure 4.3. Temperature fluctuations recorded during the test to verify the fiber aging for a period of about one year.

4.2 Sensor stability tests

The test described in the previous section was designed to analyze the stability of the plastic optical fibers.
In this test, instead, not only the fiber behavior, but also the contribution of the sensor arranged in reflection structure has been investigated.
For this, two sensor prototypes, namely $S1$ and $S2$ respectively, have been configured employing fiber spans of the same lot used in the previous test. Both the transmitting and the receiving fiber span has a length of 5 m.
The sensors have been characterized and then they are blocked in a known position in order to have a sensor response sensitive to the external environmental conditions.

The sensors sensitivity has been evaluated in the fixed position, that is $d = 2$ mm, obtaining $k_1 = -2$ μm/mV and $k_2 = -2.5$ μm/mV for $S1$ and $S2$ respectively.
A first experimental test has been carried out at room temperature for about 10 days.
Fig. 4.4 shows both sensors output variations. The corresponding displacements have been evaluated from the experimental sensors response, obtaining as maximum values about -8 μm and $+8$ μm for $S1$ and $S2$, respectively.
Then, in order to simulate a long-term monitoring, the same test has been extended to 90 days.

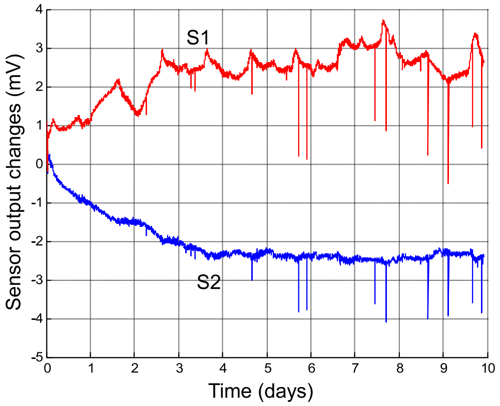

Figure 4.4. Test of two displacement sensors arranged in reflection structure, blocked in a fixed position, for a period of about 10 days.

The sensors output variations for both sensors are reported in Fig. 4.5. The corresponding displacements have been evaluated as maximum values about -30 μm and $+38$ μm for $S1$ and $S2$, respectively.

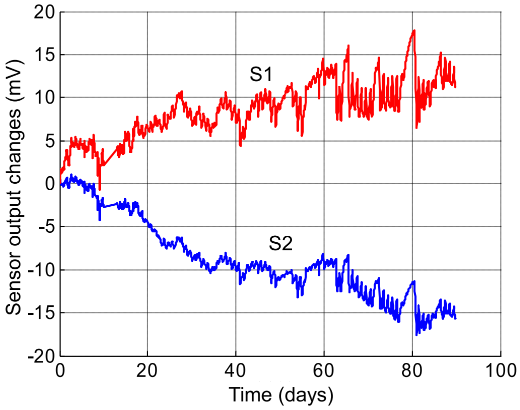

Figure 4.5. Test of two displacement sensors arranged in reflection structure, blocked in a fixed position, for a longer period of about 90 days.

These experimental results have been shown a different drift between the sensors response. The relationship between the sensor output changes (and thus the corresponding displacements) and the elapsed time is not linear. Hence, the expected displacements are not easily predictable. Consequently, it is evident that the compensation technique based on a null sensor can not completely effective due to the fiber instabilities and the sensor drifts.
In order to overcome this drawback, another compensation technique has been investigated and the proposed compensation approach, based on different wavelengths, has been described in the next chapter.

4.3 In situ sensor stability test

During the investigation of the stability issues and the development of the 2-D displacement sensor, there was the opportunity to install a crack monitoring system in a famous monument in Torino, the "Chapel of the Holy Shroud", also named "Guarini Chapel", shown in 4.6(a), from the name of the artist who designed its dome.
The chapel is currently under intense restoration, as highlighted in the external (see Fig. 4.6(b)) and in the internal view (see Fig. 4.6(c)) of the chapel, after the terrible fire happened in 1997 which caused massive damages to the structure including the detaching and collapsing of decorations, marbles and statues.
This project, supported by the Italian Ministry of Cultural Heritage and Activities, including our group of Politecnico di Torino, the applied Research center "Istituto Superiore Mario Boella" and the company Lachesi, requires a permanent monitoring system to detect possible fatigues in the artistic heritages under restoration inside the chapel. [1].
For obviously reasons, the main system requirement is fire safety, but also minimum visual impact and an installation at low costs are required.

(a) (b) (c)

Figure 4.6. A panoramic view of the Guarini dome (a), the outside view (b) and an internal overview (c) of the chapel under restoration.

For these reasons, the proposed POF displacement sensors are suitable due to the intrinsical characteristics of the fiber nature itself (fire safety, electromagnetic discharges immunity, minimum visual impact) adding the employment easiness and the simplicity of the interrogation system realized at low costs.
Hence, the proposed system architecture has been designed starting from the developed plastic optical fiber displacement sensors, employing them inside a wireless network.
The sensor is arranged in reflection structure and its working principle is that explained in the part regarding the sensor development.
Fig. 4.7 shows the realized embodiment protecting the fiber tips and the mirror from dust.
The employed fibers are SI-PMMA POF having 0.5 mm diameter without protective jacket, because the absence of the jacket and a smaller diameter allow to the fibers to appear almost transparent.
The wireless sensor network (WSN) is based on the ZigBee protocol and contains nodes of three types: coordinator, router and measurement node. This network has been designed to include one coordinator node (mains powered in a remote and safe location, always set in an active mode) interfaced to a PC, up to 16 routers (mains powered and depending on the network topology), and up to 100 measurement nodes (set to be active only during the acquisition process).
Measuring nodes are connected to the coordinator through the routers and their addresses and other configuration parameters are assigned during the initial configuration process.
Each measurement node, whose example is shown in Fig. 4.8, can interrogate up to 3 POF sensors,

---

[1] Further details about this project are available online at: *http* : *//www.progettoguarini.it*

Figure 4.7. POF sensor ready to be installed in the Chapel.

including 1 reference sensor and 2 working sensors.
The miniaturized interrogation unit contains the optical front ends, the corresponding low noise conditioning circuits, a low-power microcontroller, a wireless radiofrequency transceiver implementing the ZigBee protocol and a lithium battery.
The entire package dimensions approximately are about 5 cm length, 4 cm width and 3 cm height. The battery occupies the largest part of the package, since its capacity is of about 2 Ah in order to guarantee an operational lifetime of at least two years, supposing to set a measuring and transmission process every 30 minutes.
More in general, the system can be set in order to save and maintain the measurements in the microcontroller memory until they are send at predefined time intervals, when the nodes, in sleep-mode for most of the time, are waken-up to collect and also transmit the data.

To maintain a compact size for the measurement node, the data acquisition is performed with a microcontroller that is embedded in a dedicated and miniaturized interrogation unit.

Figure 4.8. Top view of the measurement node.

The microcontroller firmware implements the sensor calibration curve, allowing the measurement of the crack displacement to be performed inside the node.
The sensor characterization has been performed before the installation.
The calibration uncertainty depends mainly on the residual linearity errors (a low number of segments is employed due to the poor microcontroller computing capacity and memory) and on sensor repeatability effects. Hence, the obtained calibration uncertainty is about 50 μm for all the sensors.
Fig. 4.9 shows the WSN structure designed to monitor the chapel. The red spots represent the

measurement nodes, the blue ones the routers and the green one is the coordinator connected to the PC, where the maximum radiofrequency range is up to 100 m.

A preliminary version of the proposed network has been installed inside the Chapel to verify the performance of the proposed optical sensors, including four measurement nodes able to interrogate ten optical sensors, and a coordinator.

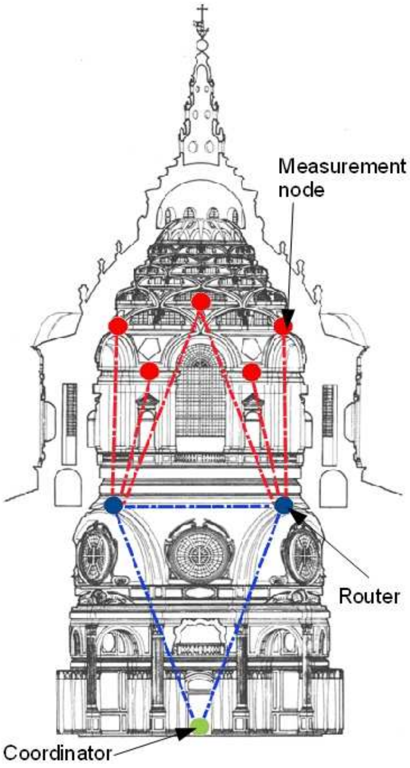

Figure 4.9. Frontal view of the wireless sensor network.

POF sensors have been fixed on marble statues recently restored, that require to be monitored because are maintained inside the chapel during its restoration works.

Some of the installed measurement nodes and the fixed POF sensors are shown in Fig. 4.10.

Fig. 4.11(a) shows the detail of the measurement node that controls the two POF sensors fixed on the marble statue of Fig. 4.11(b). In particular, the sensors are placed very close, but one sensor is placed across the crack in order to evaluate the displacement, while the other is blocked in order to be employed as reference sensor.

The experimental tests are currently in progress. Anyway, the first experimental test has been carried out in a period of about two months.

The acquired results are shown in Fig. 4.12 and they are obtained detecting the responses of the POF sensors shown in Fig. 4.11(b).

More in detail, Fig. 4.12(a) shows the reference sensor response, Fig. 4.12(b) the working sensor output, while Fig. 4.12(c) shows the temperature fluctuations recorded from the measurement

Figure 4.10. Installed measurement nodes and fixed POF displacement sensors on the marble statues inside the chapel during the restoration works.

Figure 4.11. Example of one installed measurement node (a), controlling two POF sensors fixed on a female marble statue maintained inside the chapel during the restoration works.

node.

Comparing both the reference sensor and the working sensor outputs, it is possible observe a similar drift of about 50 μm with superimposed smaller oscillations, demonstrating that, in the monitored period, the crack evolution is below the sensors sensing capabilities.

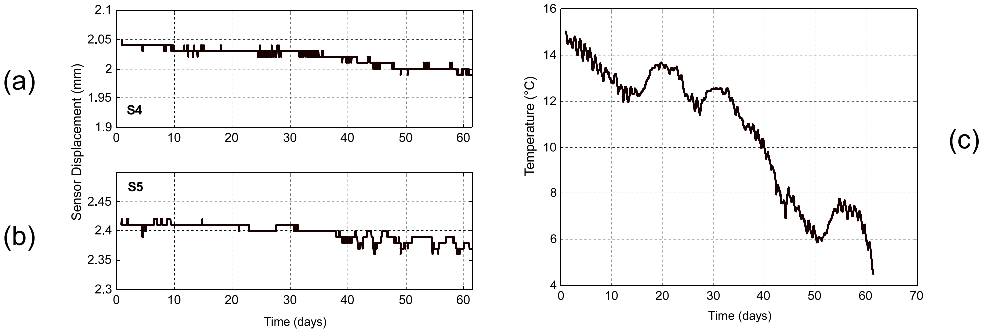

Figure 4.12. Measured results in a period of about two months. Measured displacement by reference (a) and working (b) sensor of Fig. 4.11(b) and measured temperature (c) from the node of Fig. 4.11(a).

The sensor drifts are further analyzed. The sensors response is influenced by the thermal expansion

of the sensor embodiment. Accounting for the brass thermal expansion coefficient, a temperature variation of about 10°C (measured in Fig. 4.12(c)) should correspond at only about 5 μm, that is not enough to explain the measured sensors drifts.
Consequently, these residual effects can be attributable to the temperature effects on the fibers. These effects can be evaluated as about 4 μm/°C influencing the fibers behavior [2].

---

[2] The work done inside the Guarini project is also published [21], [22]

Chapter 5

Development of displacement sensor with increased stability

Laboratory stability tests and the experimental results from field activities have demonstrated that the main drawback of the proposed displacement sensor is the large sensitivity to external perturbations, like fiber aging and temperature and humidity fluctuations.

They strongly influence, especially in long term monitoring, the received signals that become not distinguishable from that produced by actual modification of the displacement.

For this reason, a certain number of schemes have been studied to compensate the parasitic power fluctuations in the developed plastic optical fiber displacement sensors [23], [24].

The most straightforward solution is the usage of reference sensors, as done in the monitoring inside the Guarini Chapel.

This is usually effective to compensate the environmental stimuli (temperature, humidity) but not has effects typically on the attenuation of the specific fiber span, such as mechanical stresses and aging.

Hence, a displacement fiber sensor with higher stability has been designed modifying the structure of that has been already developed, introducing a wavelength-selective element in the light path, and feeding the system with two signals at different wavelengths, respectively used to measure the displacement and to correct the sensor reading.

5.1 Sensor working principle

The "conventional sensor" architecture, shown in Fig. 5.1, basically composed of two plastic fibers, an optical source OS1, a reflecting movable target and an optical detector, has been modified in order to implement the proposed compensation technique.

The new structure, shown in Fig. 5.2, includes another optical source OS2, a coupler and a selective filter to reflect the signal from one of the sources.

The sensor arranged in the conventional architecture is able to evaluate the displacement starting from the signal coupled into the receiving fiber after the propagation forward and backward over a distance d_M from the reflective target.

Thus, the detected optical power depends on the launched optical power, on the optical sensor response and on the loss A. It is reported in Eq. 5.1:

$$P_R = P \cdot A \cdot R(d_M) \tag{5.1}$$

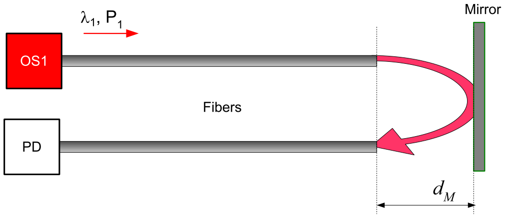

Figure 5.1. “Conventional sensor” scheme.

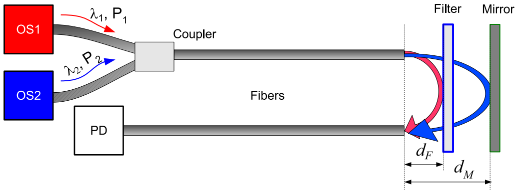

Figure 5.2. Modified sensor scheme in order to obtain a displacement sensor with increased stability.

where $R(d_M)$ corresponds to the optical power ratio and it is a function of the target distance d_M (depending also on the fiber geometrical and optical characteristics). The behavior of the sensor response is the same already shown in the previous chapter, reported also here for clarity in Fig. 5.3. The new sensor structure, modified to implement the proposed compensation technique, uses two light emitting sources having two different wavelengths λ_1 and λ_2 respectively, turned on and off alternately.

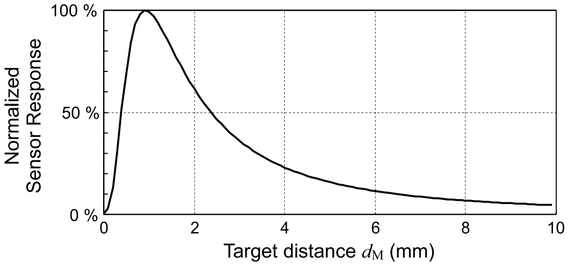

Figure 5.3. Normalized sensor response with the distance.

An optical filter is placed between the fiber tips and the movable mirror in the position d_F, that is kept constant with respect of the fiber tips.

The filter is chosen to reflect the signal at one wavelength (λ_1) and transmit the signal at other wavelength (λ_2).

The optical signal P_{R1} at λ_1 is detected when OS1 is active, while P_{R2} at λ_2 is received when OS2 is on. Considering in first approximation that the filter is ideal, the detected optical signal can be written in Eq. 5.2:

$$\begin{aligned} P_{R1} &= P_1 \cdot A_1 \cdot R(d_F) = k_1 \cdot R(d_F) \\ P_{R2} &= P_2 \cdot A_2 \cdot R(d_M) = k_2 \cdot R(d_M) \end{aligned} \tag{5.2}$$

where k_i is the product of the source power and fiber attenuations for each wavelength, and $R(d_F)$ is the sensor response evaluated at the filter position d_F, while $R(d_M)$ is the same but at the mirror position d_M.

Since the attenuation of plastic optical fibers is dependent on the wavelength [1], A_1 is different from A_2, but this is not relevant, provided that they change of the same quantity over time.

Moreover, in case of constant optical power, P_1 and P_2, the ratio between P_{R2} and P_{R1} can be written in Eq. 5.3:

$$\frac{P_{R2}}{P_{R1}} = \frac{k}{R(d_F)} \cdot R(d_M) \tag{5.3}$$

where $\frac{k}{R(d_F)}$ can be considered constant.

Hence, this ratio is theoretically insensitive to changes of the power fluctuations.

5.1.1 Real filter issues

Since ideal filters do not exist and real filters are not able to completely transmit or reflect a signal at a certain wavelength, the unwanted effects produced by a real filter employment has to be studied.

Defining as T_1 and T_2 the filter transmission coefficients at λ_1 and λ_2, respectively, the detected optical powers change as in Eq. 5.4:

$$\begin{aligned} P_{R1} &= P_1 \cdot A_1 \cdot [R(d_F) \cdot (1 - T_1) + R(d_M) \cdot (T_1)^2] \\ P_{R2} &= P_2 \cdot A_2 \cdot [R(d_F) \cdot (1 - T_2) + R(d_M) \cdot (T_2)^2] \end{aligned} \tag{5.4}$$

It is evident that to maximize the received signal, it is advisable choose a filter with a very small transmission coefficient T_1 at λ_1 and a large transmission coefficient T_2 at λ_2.

Moreover, since in the sensor working region the signal decreases when the distance increases, the sensor response at d_M is smaller than the response at d_F, and hence the term $R(d_M) \cdot (T_1)^2$ is negligible with respect to $R(d_F) \cdot (1 - T_1)$.

For these reasons, the power ratio changes as in Eq. 5.5:

$$\frac{P_{R2}}{P_{R1}} = k \cdot \left[\frac{1 - T_2}{1 - T_1} + \frac{T_2^2}{R(d_F) \cdot (1 - T_1) \cdot R(d_M)} \right] = k \cdot [a_0 + a_1 \cdot R(d_M)] \tag{5.5}$$

Eq.5.5 is the expression that describes the compensated sensor response as a function of the mirror distance, but it is highlighted an additional term $(k \cdot a_0)$ depending on the small quantity of measurement signal that is partially reflected from the filter and perturb the reflected signal by the mirror.

This constant term, at large distances, becomes prevalent with respect to distance depending term, thus reducing the sensor working range.

Moreover, it is clear that the choice of the filter position affects the sensor working range and also the amplitude of the compensation signal, since a large signal quantity is almost completely reflected by the filter.

---

[1] for details on attenuation dependence from wavelength see appendix on POF

The filter position may slightly change because of thermal and mechanical stability issues, but this effect can be reduced choosing a filter location that minimize the sensitivity of the reference signal with the filter position. Hence, the minimum of the sensor working range is bounded by the filter position and thickness while the maximum depends in theory on the free movement of the mirror. But in the real cases, the noise of the electronic conditioning circuits, that limits the sensor resolution, reduces the maximum of working range, because for the large distances the measurement signal becomes corrupted by the noise.
For these reasons, the filter position is a critical parameter to choose appropriately.

5.2 Experimental setup

Fig. 5.4 shows the displacement sensor arranged to test the feasibility of this proposed compensation technique.

In the experimental tests, the optical sources and the coupler have been replaced with a multicolor LED able to generate three different wavelengths: 465 nm (blue), 525 nm (green) and 625 nm (red), because the LED provides better stability than the optical coupler.

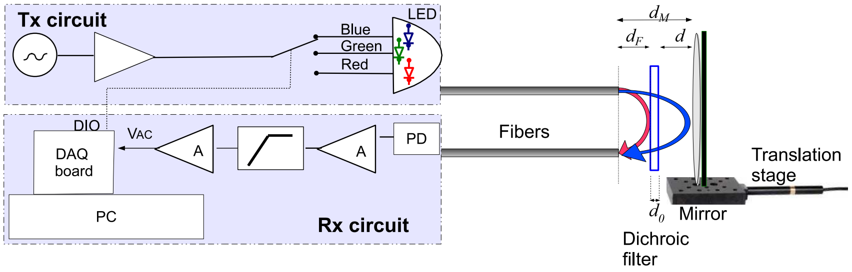

Figure 5.4. The realized setup to test the effectiveness of the proposed technique for the compensation of power fluctuations in displacement sensors.

This LED is fed by a constant current and an electronic switch turns ON (optical signals are modulated at a frequency about 1 kHz) and OFF alternately the different sources.
The optical fibers are standard PMMA-SI-POF having 0.98 mm of core diameter: one is coupled with LED, the other with the photodetector (PD).
The PD current is converted to an electric signal and amplified. Also, the fibers are fixed in a bundle positioned on a manual translation stage in front of the filter.
The chosen filter is a commercial dichroic model produced by Thorlabs, having a 2 mm thickness; the filter transmittance coefficient T_2 is about 90% at 465 nm (blue light), the transmission coefficient T_1 is about 1% at 625 nm (red light), while the green light is located at the transition band. The filter optical response is shown in Fig. 5.5 superimposed at LED spectra, measured before the tests using a high resolution CCD based spectrometer. The filter is suitable to be employed with blue and red light, because provides the best separation between these two wavelengths; hence, they have been employed in the sensor implementation.

An automatic translation stage is employed to move the mirror in order to apply known displacements and acquire the sensor response. This stage embeds a motorized actuator controlled by means a personal computer (PC).
A dedicated software running on the PC controls the digital switch employed to select the LED wavelength, the translational stages to change the distance d_M and acquires the detected signals.

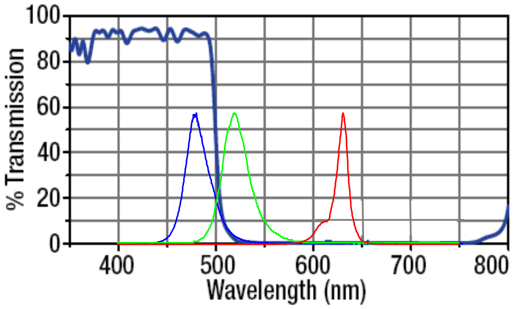

Figure 5.5. The optical response of the dichroic filter employed in the setup superimposed with LED spectra.

The optical part of the experimental setup employed to test our displacement sensor is shown in Fig. 5.6, while the filter behavior is highlighted in Fig. 5.7, that shows some photographs taken during the experimental tests when the red and blue light are alternatively switch on. As expected, the reflected red light (Fig. 5.7(c)), is more intense than the transmitted one (Fig. 5.7(a)), while the reflected blue light (Fig. 5.7(d)) is larger than the reflected one (Fig. 5.7(b)).

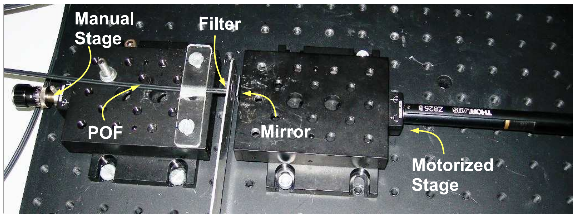

Figure 5.6. The optical part of the experimental setup employed to test the feasibility of the compensated displacement sensor.

5.3 Experimental tests

5.3.1 Design considerations

In order to maximize the signal amplitude, and therefore minimize its uncertainty, the filter should be located at the optical peak, so at about 1 mm from the fiber tips. This choice also minimizes the sensitivity of the reference signal with the filter position, because at the optical peak the signal reflected by the filter is almost constant with the filter position.

Anyway, to increase the sensor working range, and considering the reflected signal level is remarkably high, the filter was placed at a shorter distance with $d_F = 0.5$ mm from the fiber tips.

The sensor response with filter has been obtained employing the optical model described in Eq. 5.4, starting from a distance of about 3 mm (adding d_F, d_0 and the minimum tolerance to avoid the contact between the filter and the mirror to prevent frictions).

For comparison purposes, the sensor response without filter has been evaluated employing Eq. 5.2

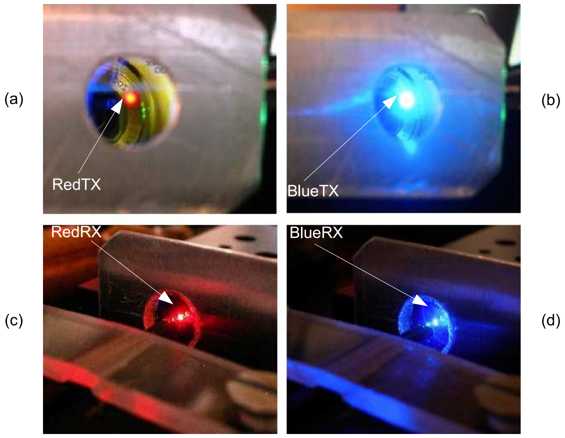

Figure 5.7. Photographs of optical signals during an experimental test: red (a) and blue (b) transmitted signals, red (c) and blue (d) reflected signals.

from the starting point, that in this case is equal to 0 mm, that corresponds to the fiber tips position.

The comparison between the sensor optical response with and without filter in the same sensor working range is reported in Fig. 5.8. The response of uncompensated sensor has a wider operating range, and smaller noise effects than the compensated sensor since the optical signals are not attenuated by the filter and the wider sensor response tends to nullify asymptotically. On the contrary, the response obtained using the filter decreases with the distance, as expected, and also presents a horizontal asymptote due to the offset term $(k \cdot a_0)$ in Eq. 5.4 and it has a reduced sensitivity for large distances.

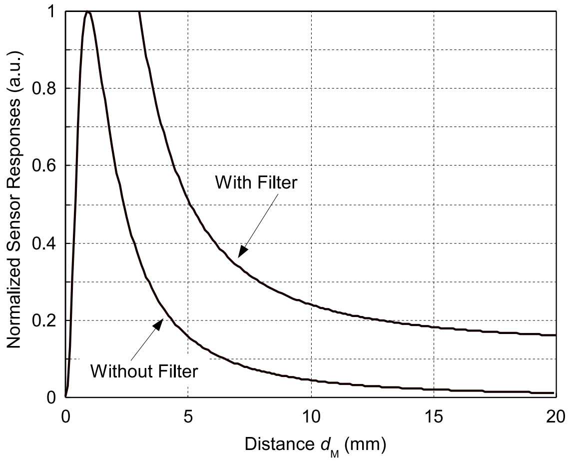

Figure 5.8. Theoretical sensor optical response with filter and without filter.

The uncertainty effects due to the noise on the measured distances have been evaluated employing

the sensor optical models and supposing a noise amplitude of about 0.1% of the detected signal range.
The comparison for the sensor with and without compensation of the corresponding distance uncertainties are shown in Fig. 5.9.

Since the sensor with the filter exhibits a larger uncertainty, assuming that the maximum tolerable value of uncertainty is about 100 μm, the sensor without filter presents a working range from 1 mm to 9.5 mm that is from the position of the optical peak to the fixed threshold value, while the compensated sensor works correctly only from about 3 mm to 9 mm, and thus it has a reduced working range.

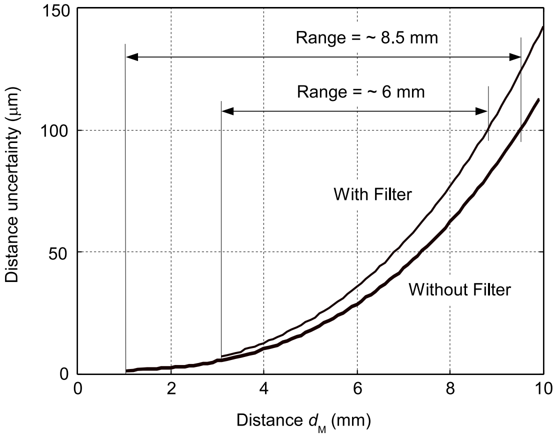

Figure 5.9. Effects of the measurement noise for both cases: uncompensated and compensated sensor response

5.3.2 Tests performed at different power levels

Tests at different optical power levels have been carried out in order to assess the effectiveness of the proposed compensation technique in the range from 0 mm to 10 mm, by changing the mirror distance d in 50 μm steps.
The red and blue lights are alternatively turned on/off at each step and the corresponding detected signals are measured through a 18 bit data acquisition board.
As d_F (the distance between the fiber tips and the filter) is maintained constant, the red signal, that is almost completely reflected from the dichroic filter, has an almost constant amplitude in the entire sensor working range. The signal depends only on the filter position and on the optical power level, and it is employed as compensation signal.
On the other hand, the filter is almost completely transparent for the blue signal, and so this signal is used to measure the distance between the fiber tips and the reflecting mirror.
Three tests have been carried out at three different power levels, namely test#1, test#2 and test#3, decreasing the power of the 25% at each test, obtaining respectively 100%, 75% and 50% of the initial power, in order to simulate a severe variation in the fiber propagation losses.

Fig. 5.10 shows the red signal amplitudes measured during the three tests; the signals are proportional to the optical power and are about constant during each test, regardless the variation of the mirror distance, as expected.

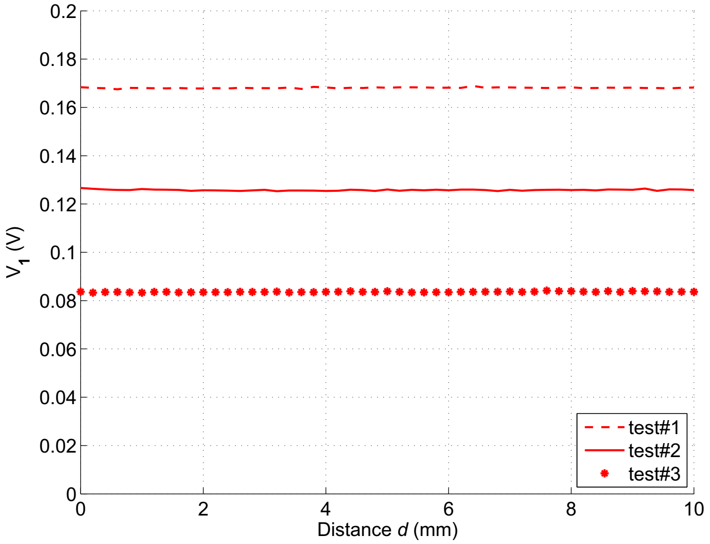

Figure 5.10. Red signal amplitudes measured at three optical power levels (100%, 75%, 50%) for mirror distance in the range of (0 ÷ 10) mm

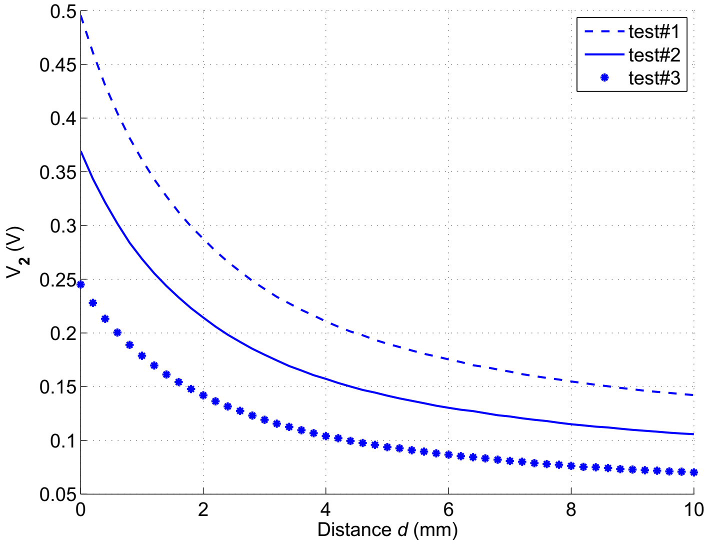

Figure 5.11. Blue signal amplitudes measured at three optical power levels (100%, 75%, 50%) for mirror distance in the range of (0 ÷ 10) mm.

Fig. 5.11 shows, instead, the blue signal amplitudes measured during the same three tests; the three signals are still proportional to the optical power and they decrease with the mirror distance d, that is considered as the distance between the filter and the moving mirror.

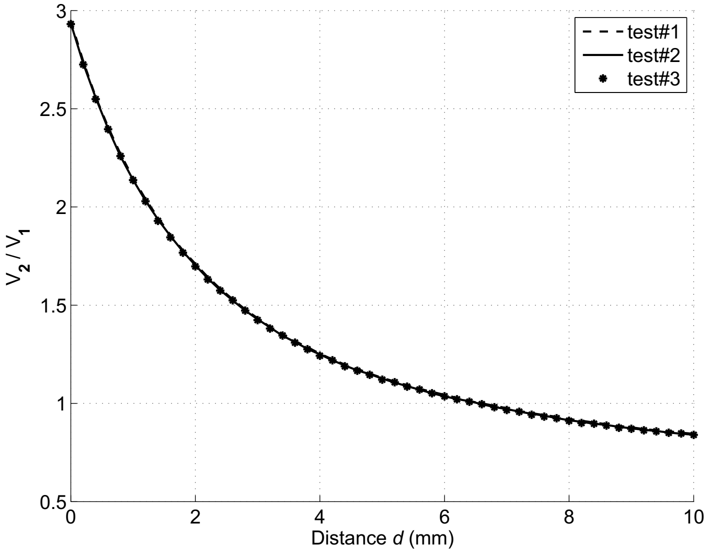

Figure 5.12. The blue/red signal ratio at three optical power levels (100%, 75%, 50%) for mirror distance in the range of (0 ÷ 10) mm.

In Fig. 5.12 is reported the ratio between the blue and red signals; the curves related to the three tests are overlapped because the ratio depends on the distance and is not influenced by the launched power, confirming the compensation capability of the proposed technique.

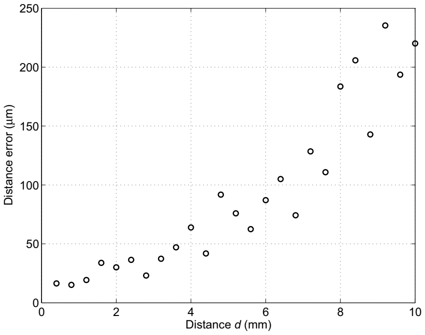

Figure 5.13. Distance error evaluated at different power levels.

The sensor performance has been investigated employing test#1 as calibration curve and calculating the distance error that arises when the sensor works at a reduced optical power.
Fig. 5.13 shows the displacement error evaluated at different power levels for variations of distance d in the range from 0 mm to 10 mm. This error remains below 100 μm for displacement up to 6 mm. For comparison, let's consider the case without compensation (that is the blue signal only) shown in Fig. 5.11: in the case of a received voltage of V = 0.2 V, the estimated distance would be

in the range of (0.3 ÷ 4.3) mm, obtaining an error of about ±2 mm, while using the compensated sensor the maximum residual error is reduced below about 50 μm.

This residual error could be caused by the response instability of the active optical components (LED and PD) described before, and also to the instabilities due to mechanical setup, since the test was performed over a period of several hours.

5.3.3 Thermal tests

The previous section has been demonstrated the capability of the proposed compensation technique to mitigate optical power changes.

In practical tests that we have been carried out, however, residual optical errors were noticed. They are not only due to the mechanical instabilities, but also caused by the fiber attenuation phenomena [19].

The fiber attenuation depends on the wavelength because it is due to the different phenomena that occur in polymeric materials that could reduce the effectiveness of the dual wavelength compensation if the attenuation of the reference (the red) and the measurement (the blue) signal changes in a significative way.

For these reasons, further investigations have been carried out on the choice of the two wavelengths. The choice of two wavelengths closely spaced would provide the best results; unfortunately, it is very difficult implement this option at a reasonable cost since two close wavelengths would require very selective filters, which costs are very high.

On the contrary, two wavelengths more spaced can be easily separated by a low-cost dichroic filter; however, their spectral distance may be too large to provide a satisfactory compensation results.

To verify this behavior, some tests have been performed with the previous filter and the fibers and sources available in the laboratory to find the fiber/source combination that provides good compensation results without requiring expensive filters.

Firstly, the behavior of several fiber spans, produced from different manufacturers were investigated with different sources. Among these spans, a 20 m length of multicore POF having 1 mm diameter has been selected, since it has similar attenuation changes at the red and green light. The source employed in this case is the "RGB" LED described before, where the green junction, having the peak wavelength at 525 nm, has been enabled. The green light has been employed as the measurement signal, even though it is only partially transmitted by the available filter, while the red signal is still employed as the reference signal. Unfortunately, the filter transmission coefficient at the green light is lower than at blue and this fact affects the sensor sensitivity and consequently reduces the sensor working range.

Anyway, the fiber sensor is able to work with the red/green sources and further tests have been performed at a fixed distance exposing the fiber at different temperatures in order to force a change in the fiber attenuation. To change the fiber temperature, the climatic chamber available in our laboratory, shown in Fig. 5.14, has been employed.

In this test, whose results are shown in Fig. 5.15, the fiber temperature was changed from 8°C to 50°C while the sensor was maintained at a fixed position at ambient temperature outside the chamber, recording the detected signals for about one day.

In particular, Fig. 5.15(a) shows the temperature variations for the fiber T_F and for the sensor T_S, Fig. 5.15(b) the relative variations of the detected signals V_1 (red) and V_2(green), while Fig. 5.15(c) shows the relative variations of the ratio V_2/V_1 (green/red). In fact, it is possible to notice that the temperature affects both the signals amplitude, and the change is about 5%, corresponding to a fiber temperature sensitivity of about 0.25%/°C.

Working without compensation, that means considering only the green signal, the signal change cornensponds to an apparent displacement of about ±1.7 mm, since the sensor sensitivity is of

about S = -3%/mm. On the contrary, working with compensation, that means computing the ratio between the green and the red signal, there is a reduction of the temperature effects on the measurement distance down to±0.3 mm and the sensor temperature sensitivity decreases to 0.05%/°C.
Moreover, this technique allows the compensation of the unwanted signal drifts due to the poor sensor setup, such as can be observed comparing the measurements of red and green signals at the beginning and at the end of the test.

Figure 5.14. Climatic chamber available in our laboratory for thermal tests.

The previous tests have also shown that the attenuation drift in the polymers, constituting the common types of plastic optical fibers, depends significantly on the wavelength. As a consequence, an effective compensation can be obtained only using a proper wavelength combination for measurement and reference signals, with the drawback to reduce the sensor working range.
Anyway, the proposed compensation technique can be successfully used either alone or to complement the reference sensor technique previously described, in order to enhance the long-term stability of the sensor against environmental disturbances, such as temperature variation and mechanical stresses acting on the fibers [2].

---

[2] The work regarding the proposed compensation technique is also published in [25], [26], [27]

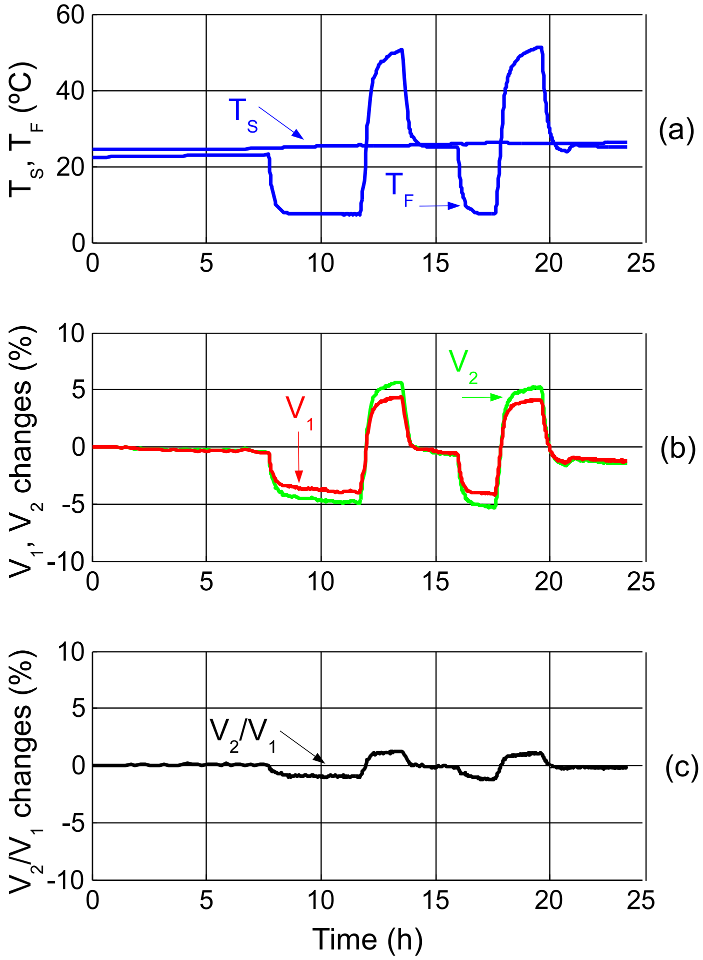

Figure 5.15. Thermal test of a multicore POF employed to arrange a compensated sensor. Fiber (T_F) and sensor (T_S) temperature (a), measurement (V_2) and reference (V_1) signals (b), signal ratio (V_2/V_1) (c).

Chapter 6

Development of a non contact POF displacement sensor for vibration monitoring

6.1 Vibration monitoring issue

Monitoring vibrations is not only related with short-term evaluation of crack evolutions, but it has an even more role relevant in many other fields of industrial engineering, where vibration tests are fundamental to study the dynamic behavior of machines and devices.

Usually, these tests are carried out employing shakers controlled by suitable systems that force known accelerations, following the recommendations of specific standards, such as the IEC 60068-2-6 for sinusoidal tests, to evaluate the mechanical behavior of machinery parts (i.e. printed circuit boards, solar panels).

During these tests, acceleration sensors are employed to measure the shaker table acceleration from which the vibration amplitude is computed. At least one of these sensors is used to measure the acceleration of the shaker vibrating table, while others acceleration sensors are placed on the device under test (DUT) to study the onset of resonances.

A sketch of the equipment necessary to carry out these vibration tests is shown in Fig. 6.1.

Typically, the vibration sensors are inertial accelerometers with wide frequency response, high dynamic range and a small size. They exploit piezoelectric, piezoresistive or capacitive working principles.

Examples of mechanical transducers suitable to measure accelerations are reported in Fig. 6.2.

In most cases, acceleration sensors can be directly placed on the surface of the device under test because the effects due to their dimension and weight can be neglected.

However, many situations exist, i.e. the testing of printed circuit boards (PCBs) and solar panels, where even the smallest and lightest accelerometer cannot be placed directly on the surface of the DUT, due to lack of space or because it can introduce perturbations due to its mass.

In those cases a non contact vibration measurement technology must be employed.

Optics technology provides excellent solutions for non-contact distance measurements, and indeed several optical techniques have been proposed in the literature, such as interferometry [28], [29] and laser Doppler vibrometry [30], [31].

However, the main limitation to their wide spreading comes from their cost. For example, some

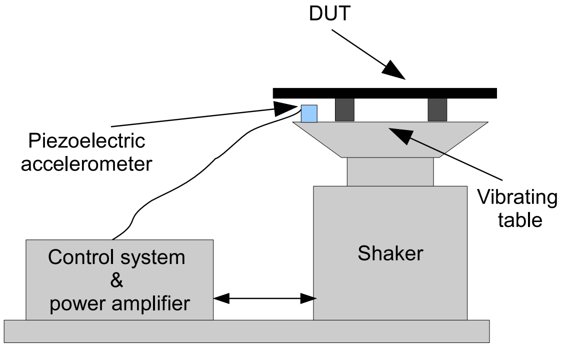

Figure 6.1. Structure of a typical vibration facility required for vibration tests: a shaker with power amplifier, vibrating table control system and acceleration sensors to measure the acceleration imposed by the shaker.

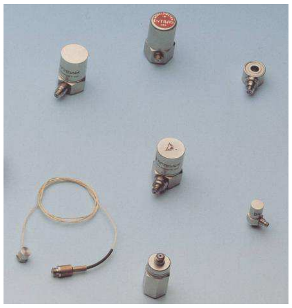

Figure 6.2. Examples of commercial acceleration sensors.

laser vibrometers are commercially available as a portable device but they are still quite expensive. In alternative, intensity-based fiber optic sensors using glass fiber bundles have been proposed in literature [6], [32], [33], [34], allowing non contact distance measurements to be performed with a good resolution at a lower price.

The aim of the activity described in this chapter is the development of a displacement intensity-based sensor made of plastic optical fiber to be employed in vibration tests without contact.

6.2 Sensor working principle

The sensor architecture is similar to that employed to realize the crack displacement sensor, but in this case the fiber tips are faced to the vibrating target.
This fiber vibrometer, shown in Fig. 6.3, is basically composed of two plastic fibers: one transmits the light, while the other receives the light that is reflected from the vibrating target.
As already discussed, in this case too, the use of POF allows working at much larger distances from the target with respect to glass fibers, thanks to their larger NA and diameter.

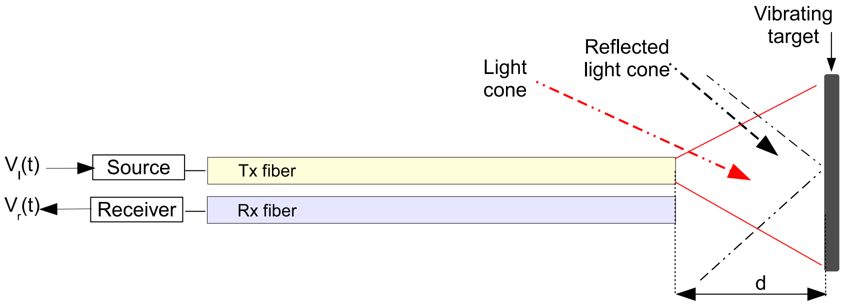

Figure 6.3. Fiber vibrometer working principle.

The fiber radius is w_a, the separation between the two fiber axes is equal to $2 \cdot w_a$, the distance between the vibrating target and the fiber tips is d. In this application, d depends on the sensor stand-off d_0, also called "working distance", and on the vibration amplitude $s(t)$, having:
$d = d_0 + s(t)$.
The expression of the received voltage $v_R(t)$ can be obtained through Eq. 3.1 and hence:

$$v_R(t) = A \cdot v_L(t) \cdot \frac{P_R(d)}{P_T} \tag{6.1}$$

where $v_L(t)$ is the voltage applied to the source, $\frac{P_R(d)}{P_T}$ is the ratio between the optical power at the receiving and at the transmitting fiber surfaces, while the term A includes all the factors independent from the distance d, both for the electronic (amplifier gains) and the optical part (source efficiency, photodetector responsivity, reflectivity of the vibrating target, fiber losses).
Employing a reflective surface, in the case of Gaussian approach, it is possible evaluate the quantity $\frac{P_R(d)}{P_T}$ by means of the Eq. 2.11 as:

$$\frac{P_R(d)}{P_T} = \left[\frac{2 \cdot w_a^2}{d^2 \tan(\theta_a)^2} \cdot \exp\left(-2 \cdot \frac{r^2}{d^2 \cdot \tan(\theta_a)^2}\right)\right] \tag{6.2}$$

where θ_a is the angle related of the light cone and r is the value of the radial coordinate perpendicular to the fiber axis, which value depends on the fiber dimensions and eventually from the presence of the jacket, accounting that the equivalent sensor structure is shown in Fig. 2.15.
The target vibrations change the distance between the fiber tips and the target and, therefore, the received optical power $P_R(d)$.
Consequently, when the target displacement due to the vibration is small with respect to the working distance, the optical power ratio can be expressed using this linear approximation:

$$\frac{P_R(d)}{P_T} = R_{EQ} \cdot [R_0 + R_1 \cdot (d - d_0)] \tag{6.3}$$

which can be rewritten highlighting the target displacement $s(t)$ due to the vibrations, obtaining:

$$\frac{P_R(t)}{P_T} = R_{EQ} \cdot [R_0 + R_1 \cdot s(t)] \tag{6.4}$$

where R_0 is the optical power computed for reflectivity unit and R_1 is its first derivative (both evaluated at the working distance d_0) and R_{EQ} is the equivalent reflectivity of the area lighted by the transmitting plastic fiber.
The received signal can be also written as a function of the target displacement related to the vibration amplitude:

$$v_R(t) = A \cdot v_L(t) \cdot R_{EQ} \cdot [R_0 + R_1 \cdot s(t)] \tag{6.5}$$

The simplest solution is the employment of a constant source. In this case, $v_L(t)$ is substituted with V_L, obtaining:

$$v_R(t) = A \cdot V_L \cdot R_{EQ} \cdot R_0 + A \cdot V_L \cdot R_{EQ} \cdot R_1 \cdot s(t) \tag{6.6}$$

As shown in Eq. 6.6, the received signal is composed of two terms: the first one is a DC term: $V_{DC} = A \cdot V_L \cdot R_{eq} \cdot R_0$, while the second one is $v_{AC}(t) = A \cdot V_L \cdot R_{eq} \cdot R_1 \cdot s(t)$, which is proportional to the displacement related to the vibration signal, obtaining $v_R(t) = V_{DC} + v_{AC}(t)$. Consequently, the displacement $s(t)$ is obtained as:

$$s(t) = \frac{v_{AC}(t)}{V_L \cdot R_{EQ} \cdot R_0 \cdot \frac{R_1}{R_0}} = \frac{v_{AC}(t)}{V_{DC}} \cdot \frac{R_0}{R_1} \tag{6.7}$$

For sinusoidal vibration tests, assuming to evaluate $\frac{R_0}{R_1}$ from the analytical model of the optical curve $\frac{P_R(d)}{P_T}$, it is possible evaluate $s(t)$ and compute the acceleration from the target displacement second derivative.
Unfortunately, the optical model depends on parameters of the sensing head and the target surface characteristics that are difficult to control.
Also, in most practical cases, these parameters cannot be determined with the required uncertainty from the analytical model of the optical curve $\frac{P_R(d)}{P_T}$.
Moreover, it is evident that the received power level and its relation with distance are strongly dependent on the test point.
The analysis of the sensor response in presence of a real target has been reported in the following, while the experimental setup employed to verify the feasibility of the proposed vibrometer is reported in the next section.

6.3 Experimental setup

The setup structure is shown in Fig. 6.4 and includes the proposed optical sensors, a computer controlled dynamic shaker with its power amplifier, the vibrating table (where the device under test is fixed during the experiments) and at least one accelerometer employed to control the dynamic behavior of the system.

Fig. 6.5 shows in more detail the sensor and the interrogation circuit. The transmitting source is a LED fed by a constant current, while the receiver has been modified starting from the circuit employed to interrogate the crack displacement sensor, because in this application, both DC and AC components, namely $v_{DC}(t)$ and $v_{AC}(t)$ respectively, are useful in order to obtain the vibration measurement (as further described in the following).

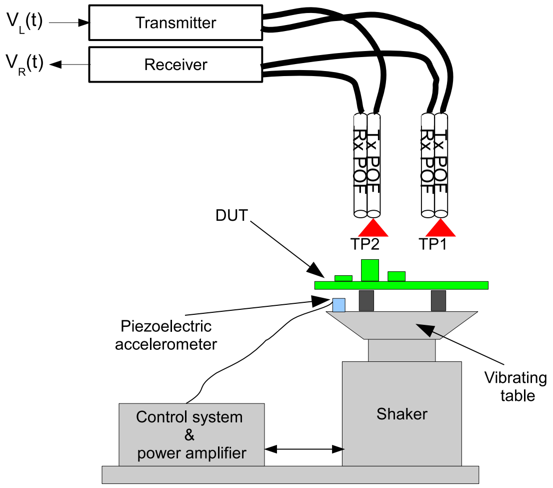

Figure 6.4. Block diagram of the experimental setup employed to test the proposed fiber vibration sensor.

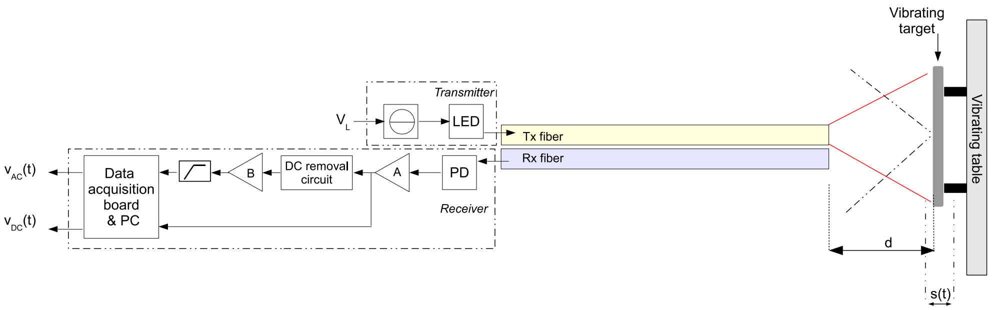

Figure 6.5. Sketch of the optical sensor structure with interrogation system.

Hence, this receiver is composed of a photodetector (PD) followed by two stages. The first is a transimpedance amplifier DC coupled, while the second is a DC removal stage, which is an amplifier with high-pass filter having a pole below 1 Hz, that amplifies in practice only the AC component of the detected signal. Both the amplifiers are band-limited to reduce the wideband noise in order to ensure the stability. This way, it is possible to acquire very-low frequency vibration signals without significative attenuation.

The DC component is measured at the first stage output, while AC component at the output of the second stage. Both are acquired through a 18-bit resolution data acquisition board, connected with a PC elaborating the signals with a DFT algorithm to extract the first harmonic components.
For the experimental tests SI-PMMA fibers having a 1 mm of diameter and 2 m length have been employed. The custom-made receiving circuits (see Fig. 6.5) have been realized with $A = 1\ \mathrm{M}\Omega$, $B = 60$ and a cutoff frequency of about 4 kHz in order to reduce the large bandwidth noise.

The measured output noise in dark conditions is about V_{RMS}=0.8 mV.

6.4 Sensor response analysis with real targets

The aim of this test is the analysis of the optical sensor response in presence of a non ideal vibrating target.
The employed DUT is a printed circuit board (PCB) populated with components.
Two optical sensors are employed in two different test points, namely TP_1 and TP_2 respectively, highlighted in Fig. 6.6. TP_1 is in a region where the lighted surface can be considered flat, although may present non-uniform reflectivity, while TP_2 is in front of a surface not even uniformly thick because of electronic components.

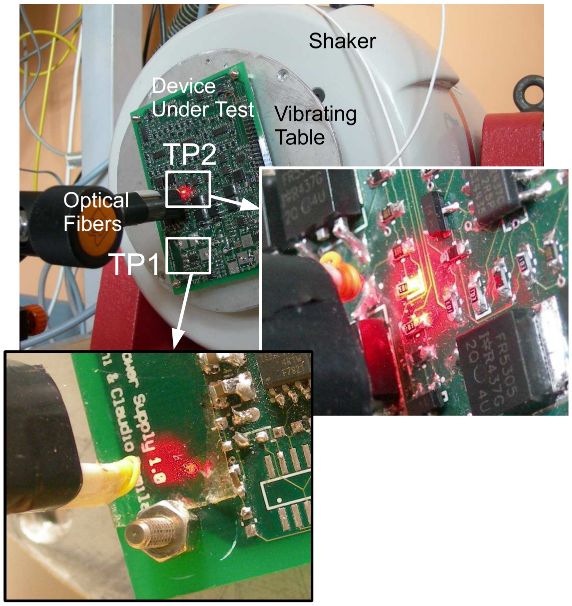

Figure 6.6. Test point TP_1 and TP_2 of the PCB under test during the preliminary characterization of the sensor.

The sensors have been characterized in absence of vibrations in the range $(0 \div 8)$ mm, that is from the fiber tips in contact with the target to a distance of about 8 mm, obtaining the curves shown in Fig. 6.7(a), representing the response proportional to the term R_0 for each sensor. The received voltages V_R, that here are V_{DC} because of vibrations absence, result directly proportional to $\frac{P_R(d)}{P_T}$, as expected.

Anyway, in both cases, the distance d is measured from the fiber tips to the target surface and it is equal to zero when the tips are in contact with the most prominent part of the PCB.
In TP_1, that is the case of a target almost uniform, when the fiber tips are in contact with the target, the received light is almost negligible, because the light from the transmitting fiber cannot reach the receiving fiber.
Contrariwise, for targets having a non-uniform surface, as in TP_2, where are present some components with different thickness and colors, the received power may be significant, as the receiving

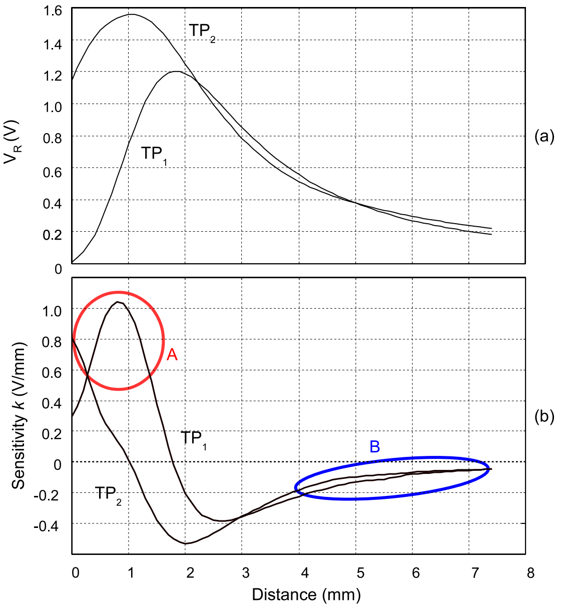

Figure 6.7. Measured received signals V_R related respectively for the sensors placed in TP_1 and TP_2.

fiber tip can be partially reached from the light reflected by the surface discontinuities.
For these reasons, the curve related to TP_2 does not start from 0 V, while TP_1 does it, as shown in Fig. 6.7(a).
Moreover, the two curves have a different shape because of the presence of the components mounted on the PCB at TP_2 and different peak amplitudes depending on the different reflectivities at the two test points.
In detail, because there are some welds points in TP_2, they cause a sparkling behavior of the surface with a consequent higher optical peak of the received power. The sensitivity of the sensors, proportional to the term R_1, shown in Fig. 6.7(b), has been evaluated as the first derivative of the results obtained in Fig. 6.7(a).
The sensors sensitivities in two different test points are different and this fact depends not only on test point characteristic, but also on the distance between the target and the fiber tips, as expected.
Hence, each sensor should be characterized separately before its employment, because it is not possible to extent the characterization result obtained in a test point to another test point. However, the calibration of each sensor is possible, but it's time consuming.
Therefore, an alternative calibration procedure has been developed to simplify the sensor characterization, and it is described in the next section.

6.5 Calibration procedure based on a reference accelerometer

This calibration procedure is based on the piezoelectric accelerometer already employed to control the shaker, that in this case is a commercial piezoelectric sensor having a sensitivity of 10.3 mV/g and a frequency response flatness of ±5% up to 5 kHz. It has been calibrated by an "ACCREDIA" center ("Centro SIT n.111" in the recent past) declaring ±5% of uncertainty.
In the considered setup, this reference accelerometer provides the vibration table acceleration and working in sinusoidal vibration conditions, this signal can be expressed as:

$$a(t) = A_P \cdot \sin(\omega_c \cdot t) \tag{6.8}$$

where A_P is the acceleration peak value measured from the accelerometer and ω_c is the known vibration frequency.
This signal is integrated twice to easily obtain the displacement $s(t)$:

$$s(t) = -\frac{A_P}{\omega_c^2} \cdot \sin(\omega_c \cdot t) \tag{6.9}$$

Since $s(t) = \frac{v_{AC}(t)}{k}$, the k term is evaluated as:

$$k = \frac{v_{AC}(t)}{s(t)} = \frac{V_P}{A_P} \cdot \omega_c^2 \tag{6.10}$$

where V_P is the peak amplitude of the AC component of the signal measured with the optical sensor.
The sign of the scale factor k can be detected through the observation of signals $v_{AC}(t)$ and $a(t)$ in the time domain; nevertheless, in many applications, knowing the sign is not relevant.

6.5.1 Calibration procedure issues

In real cases, it is suitable to analyze further those aspects of the calibration procedure (the accelerometer position, the calibration frequency ω_c, the optical sensor distance) that can strongly impact on the calibration effectiveness.

Reference accelerometer position

As the acceleration and the displacement have to be measured at the optical sensor location, the accelerometer should be placed very close to the optical sensor.
However, if the vibration frequency is low enough to be well below the resonance frequencies of the mechanical system under test, the acceleration can be considered constant in any point of the vibrating table.
Therefore, the reference accelerometer can be placed at any position, not necessarily coincident with a test point. For the same reason (the acceleration is constant over the entire vibrating table), the same accelerometer can be employed to simultaneously calibrate several optical sensors distributed over the table.

Calibration frequency

The choice of the calibration frequency has to be carried out considering, besides the vibrating table resonances, the frequency responses of the conditioning circuits of the accelerometer and the optical sensors, usually AC coupled.

Also, the acceleration cannot arbitrarily be reduced because the vibration amplitude increases at low frequencies, according to Eq. 6.9. At large displacements, systematic calibration errors can appear due to the non-linear response of the optical sensor, since in this case the hyphotesis of Eq. 6.7 is not valid.

The optical sensor response can be also affected by distortion, because a low but not negligible distortion effect can appear when the shaker controls the acceleration at low frequency.

For these reasons, considering the employed setup, in order to carry out the calibration, it is suitable avoid frequencies below a few hertz.

Optical sensor distance

The choice of the sensor distance can affect its performance since the sensor sensitivity depends on the target distance, as already shown in Fig. 6.7(b).

It is also evident that the maximum sensitivity can be reached at shorter distance, in the region A, where the fiber tips are close to the vibrating target. Also, working at small distances, the light spot is smaller. On the other hand, in this region the sensitivity stability is low and the dynamic range is not so large. Thus, it is suitable employ the sensor in the region A in order to perform local measurement with high sensitivity.

However, in practical applications, it is better employ the sensor in the working region B, where the sensor sensitivity is lower, as at larger distances it is possible to measure vibrations in a broader dynamic range and simultaneously maintain the sensor distortion low.

Furthermore, in this region, where the slope of the derivative is less slanted, the sensitivity shows a lower dependence on the distance than in the previous case.

Moreover, during the vibration tests, the working distance cannot be kept constant.

This problem can be solved by controlling the shaker not only to force known accelerations but also to maintain a steady average position. Despite both the reference acceleration and the AC component of the optical sensor signal do not provide any information about the drift of the stand-off position d_0, however it is possible evaluate this effect with the proposed interrogation system, detecting the DC component of the optical sensor response.

In particular, it is possible to measure the table position drifts exploiting the same optical sensor employed to measure the vibrations (whose are proportional to V_{AC} but considering the DC component V_{DC}.

The quantity of interest is the variation Δd from the average stand-off position d_0, that is the point where the calibration is carried out. Thus, according to Eq. 6.7, Δd can be evaluated as:

$$\Delta d = \frac{\Delta V_{DC} \cdot B}{k} \tag{6.11}$$

where ΔV_{DC} is the variation of the DC component recorded during the test and k is the sensitivity of the sensor. As k is obtained at the output of the second stage, it is necessary to take into account the gain of this stage. Thus, knowing the changes of the target distance allows to correct if necessary the sensor sensitivity.

6.6 Experimental tests

Several sinusoidal tests have been carried out to verify experimentally the feasibility of the proposed optical sensor and the effectiveness of the calibration procedure.

6.6.1 Calibration test

A calibration test has been carried out employing the demonstration setup with the configuration shown in Fig. 6.8, where the optical sensor is faced to a mirror (the employment of a high-reflectivity target increases the power level of the detected signal) while the reference accelerometer, directly fixed on the vibrating table, is positioned very close to the mirror to ensure that both sensors are subjected to the same vibrations.

The shaker has been employed to force a sinusoidal signal at calibration frequency of $f_c = 30$ Hz at constant acceleration $a_c = 1$ g $= 9.81$ m/s^2.

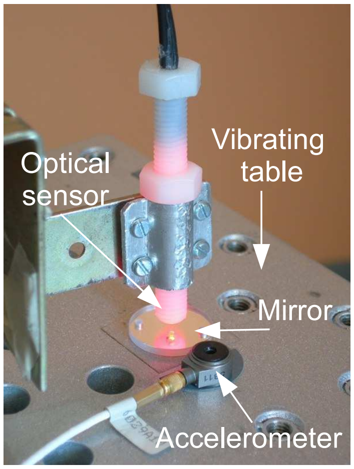

Figure 6.8. Arranged optical sensor close to the piezoelectric accelerometer during the optical sensor calibration test.

During a calibration test, both the voltage and the acceleration peak amplitudes are obtained by processing the acquired signals (through a DFT algorithm extracting the first harmonic components having set in a suitable way the sampling frequency and the acquisition time).

In this experimental test, a sampling frequency $f_s = 10$ kHz and an acquisition time $T_a = 1$ s have been employed.

An acceleration peak value $A_P = 9.21$ m/s^2 and $V_P = 2.81$ V as received AC component, at the frequency of 30 Hz, have been obtained.

Consequently, the value of the sensitivity k in this case is:

$$k = \frac{V_P}{A_P} \cdot \omega^2 = \frac{2.81}{9.21} \cdot (2 \cdot \pi \cdot 30)^2 = 10.8\,\text{mV}/\mu\text{m} \tag{6.12}$$

6.6.2 Calibration frequency choice

In the same conditions of the previous test, (constant acceleration at $a = 9.81\text{m/s}^2$, working distance $d_0 = 4$ mm that means the employment of the sensor in region B), the distortion due to the sensor non-linear response has been experimentally measured to verify the choice of the calibration frequency.

Fig. 6.9(a) shows the spectrum of the acceleration measured by the piezoelectric accelerometer,

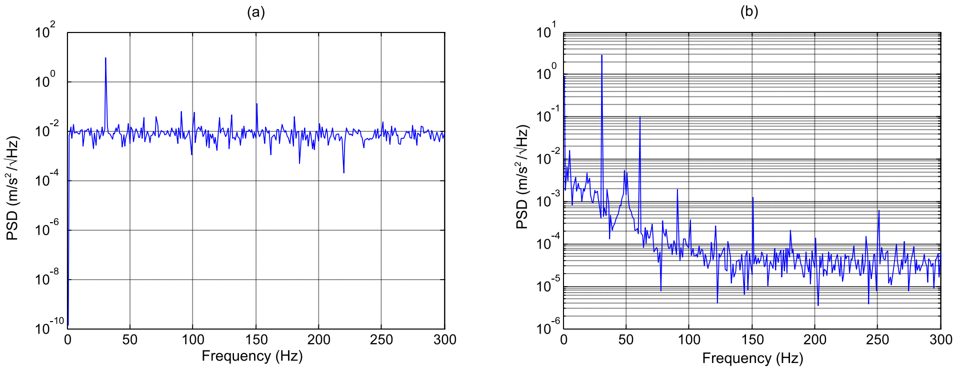

Figure 6.9. Spectrum of the acceleration (a) measured by the piezoelectric accelerometer and spectrum of the AC component of the optical sensor output (b) obtained during the calibration test.

Fig. 6.9(b) shows the spectrum of the AC component of the optical sensor output. In particular, the accelerometer signal contains a line at vibration frequency (30 Hz) superimposed at a noise floor.

The spectrum of the optical sensor presents a noise floor, accounting for both the acceleration noise shaping (due to the integrative sensor response), the effects of the conditioning circuits noise, including also the contribution due to the power supply.

The lines at the vibration frequency and its integer multiples are present because of the sensor distortion.

Anyway, the sensor distortion not only introduces harmonic components, but also affects the fundamentals component amplitude.

This amplitude error influences the sensor calibration constant and can be evaluated employing the theoretical sensor model.

The obtained simulations have shown that for a stand-off distance $d_0 = 4$ mm, the vibration amplitude must be kept below $\Delta d_{pk} = 0.6$ mm to have a calibration constant error (due to the distortion effects) below 0.1%.

Thus, it is possible to obtain the minimum value of frequency at which it is possible perform the sensor calibration, maintaining constant the calibration error:

$$f = \frac{1}{2 \cdot \pi} \cdot \sqrt{\left(\frac{A_p}{d_s}\right)} = \frac{1}{2 \cdot \pi} \cdot \sqrt{\left(\frac{9.81}{6 \cdot 10^{-3}}\right)} \simeq 20\,\mathrm{Hz} \tag{6.13}$$

6.6.3 Target distance drifts

A sinusoidal test has been performed to evaluate how well the shaker is able to maintain the vibration table position during a test.

As already explained, any change of the sensor stand-off distance d_0 after the calibration, produces an error on the measured vibration amplitude, since the sensor sensitivity strongly depends on d_0. This test has been carried out at f = 143 Hz, increasing acceleration amplitudes from 20 m/s^2 to 200 m/s^2, employing the setup shown in Fig. 6.10, where the accelerometer and a different reflecting target are directly fixed on the shaker surface.

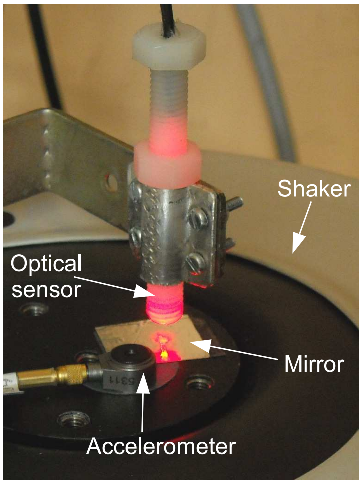

Figure 6.10. The arranged optical sensor close to the piezoelectric accelerometer during the test to evaluate the target distance drifts.

The sensor has been calibrated at the beginning of the test, choosing a calibration frequency f_c = 143 Hz at constant acceleration a = 20 m/s^2. The resulting sensitivity, according to Eq. 6.10, has been computed as $k = 15.5$ mV/μm.

The displacement amplitudes, D_{OTT}, detected from the optical sensor during the test, are in the range from about 25 μm to 250 μm, as shown in Fig. 6.11(a). Also, they are in agreement with the expected displacement computed with Eq. 6.9. Thus, the correspondent accelerations have been computed deriving twice the measured displacements.

Fig. 6.11(b) shows the relative difference, called Acc_{Diff}, between the accelerations measured with the piezoelectric sensors, and those obtained with the optical sensors. The difference is zero at the beginning of the test, where the sensor has been calibrated, and increases up to a maximum value of about 0.9% at the highest acceleration.

The average value of the detected optical signal V_{DC} has also been acquired during the test, and it is shown in Fig. 6.11(c), because this signal is strictly related to the vibrating target position during the test.

As expected, the average value of V_{DC} is not constant, but the detected signal changes from 593 mV to 597 mV, obtaining ΔV_{DC} = 4 mV, confirming that the shaker slightly modifies its average position.

As the sensitivity is known and it is equal to k = 15.5 mV/μm, it is possible compute the distance drift as $\Delta d = \frac{\Delta V_{DC} \cdot B}{k} = \frac{4 \cdot 60}{15.5} \simeq 15$ μm.

Knowing the sensitivity and the distance drift, it is possible to evaluate how the sensor sensitivity changes with the variation from the average position. This value can be determined through a theoretical analysis based on the optical model or can be computed from this test, obtaining a

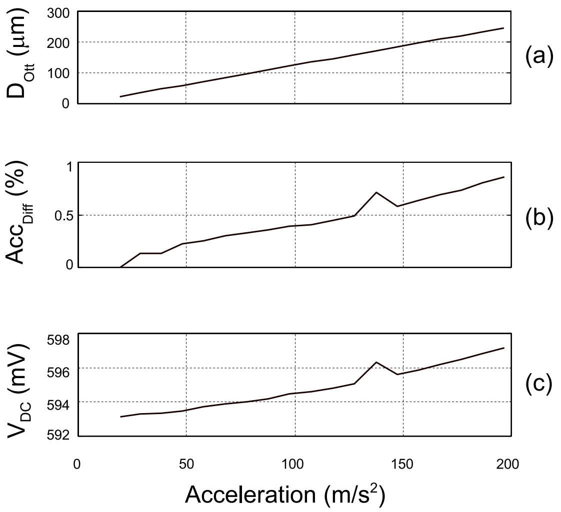

Figure 6.11. Experimental results obtained at frequency of 143 Hz at different acceleration values: measured vibration amplitude (a); relative difference between the optical sensor and the accelerometer outputs (b); average value of the detected optical signal v_{DC} (c).

sensitivity variation rate of about -0.06 $\%/\mu$m.

6.6.4 High-frequency vibration test

At low frequencies the sensor performance is limited by the sensor non-linear behavior and the stand resonances, whereas, at higher frequencies (where the target displacements are very low) the sensor main limitation comes from noise of the conditioning circuits.
The aim of this test is to verify the wideband sensor response and the effects due to the noise (the sensitivity changes due to the stand-off distance drifts at low frequency and conditioning circuits noise effects at high frequency).
This test has been carried out in a frequency range between 43 Hz and 3 kHz at a constant acceleration of 30 m/s^2, employing the setup of Fig. 6.10. Both components of the optical sensor signal have been acquired.
The sensor has been calibrated at the beginning of the test, obtaining $k = 15.6$ mV/μm.
The measurement of the DC coupled signal, is about from 538 mV to 532 mV, having a signal variation of $\Delta V_{DC} = 6$ mV. Considering Eq. 6.11, the stand-off distance variation results
$\Delta d = \simeq 23\ \mu$m. The sensitivity rate, known from the previous test, allows to correct the sensitivity as $k = -0.06\%/\mu\text{m} \cdot 23\ \mu\text{m} = 1.38\% = 15.8$ mV/μm.
Fig. 6.12 shows the displacement measured with the optical sensor and that computed from the accelerometer, demonstrating that two curves are overlapped, and also shows that the vibration peak amplitude, measured at frequency of 3 kHz is $D_{\text{ott}} = 80$ nm.

Fig. 6.13 shows instead the comparison between the acceleration computed from the displacement measured from the optical sensor and that measured by commercial device.
The accelerometer frequency flatness band tolerance of ± 5% is also reported.
The obtained results highlight a good agreement between the sensors, both at low frequency,

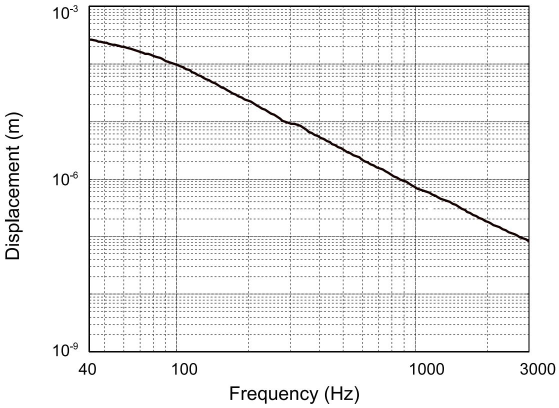

Figure 6.12. The curves related to the vibration amplitude measured by the optical sensor and to the acceleration amplitude of the commercial accelerometer are overlapped.

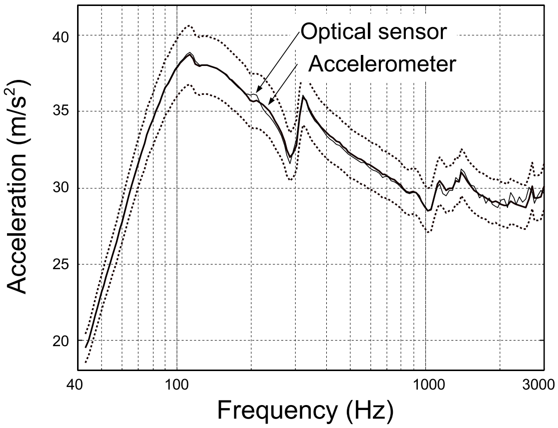

Figure 6.13. Comparison between the accelerometer response (reported with frequency flatness band tolerance drawn in dotted lines) and the acceleration evaluated from the optical sensor.

where the optical sensor has been calibrated, and at high frequency. The difference between the two curves is reported in Fig. 6.14, where the maximum relative difference is $Acc_{\text{Diff}} = \pm 2\%$ in the frequency range.

6.6.5 Sensor response during a resonance evaluation test

The optical sensor response has been detected during a sinusoidal vibration test performed in order to evaluate the resonances of the DUT.

The acceleration has been measured on the PCB surface employing the piezoelectric accelerometer and three optical sensors: the first is faced to a board tip (test point TP_1), the second is approximately faced to the center of the board (test point TP_2) while the third one (test point

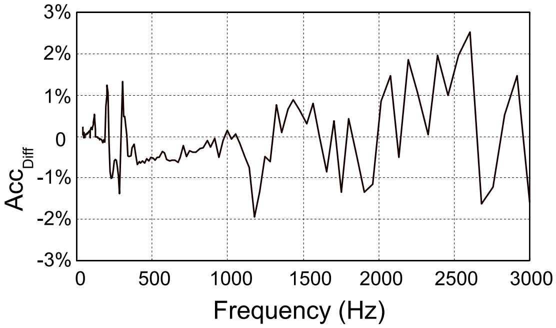

Figure 6.14. Relative difference Acc_{Diff} between the optical and piezoelectric sensor results.

TP_3, as shown in Fig. 6.15) is faced to the accelerometer in order to compare the optical and the piezoelectric sensor response. All the sensor have been calibrated simultaneously driving the shaker at a frequency of $f_c = 33$ Hz. The sensors sensitivity has been computed obtaining: $k = 3$ mV/μm. The obtained results for the three test points are shown in Fig. 6.16.

Figure 6.15. Detail of test point TP_3 chosen to compare the sensor optical and accelerometer response during the resonance test of the PCB.

The curves for TP_1 (magenta line) and TP_2 (red line) show first resonance at about $f_{r1} = 290$ Hz, while in TP_2 there is a second resonance at about $f_{r2} = 460$ Hz and the acceleration levels are higher. Thus, the PCB is more stressed in TP_2, as expected, because this point is located in the center of the board.

The curve for TP_3 (blue line) is in good agreement with the accelerometer response (green line) at any frequency.

Moreover, all the curves overlap up to about 70 Hz, confirming that the calibration frequency has correctly been chosen well below the mechanical resonances.

6.6.6 Multi-head sensor test

A multi-head sensor composed of nine optical sensors has been arranged in order to obtain a mapping of the dynamic behavior of the DUT during sinusoidal vibration tests.

Fig. 6.17 shows the proposed multi-head sensor employed for the test of a PCB and of a solar panel (placed on a module of nano-satellite prototype), respectively.

As example, the test regarding the mapping of the solar panel has reported.

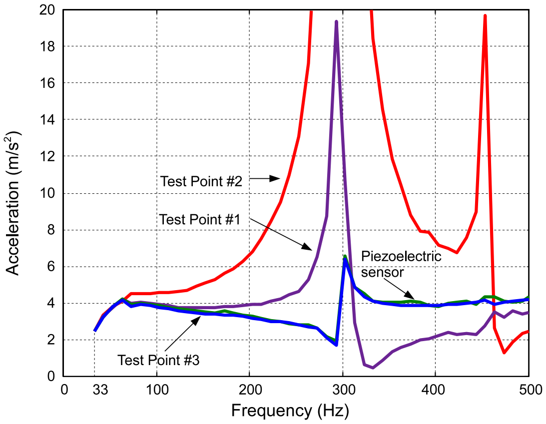

Figure 6.16. Measurement results obtained during the vibration tests of a PCB. Test points TP_1 and TP_2 are faced on the PCB surface, whereas TP_3 is faced on the accelerometer surface.

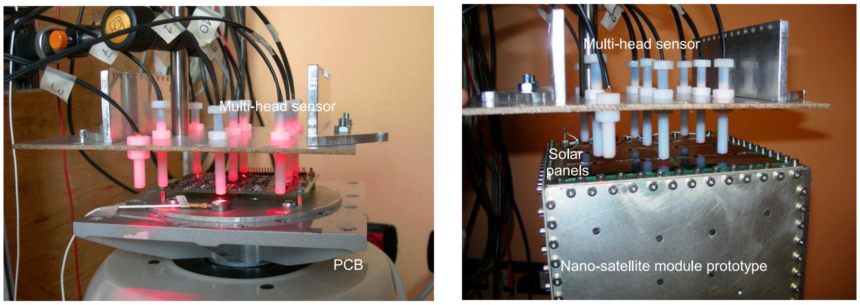

Figure 6.17. Arrangement of a multi-head sensor to be employed to measure non contact vibration during vibration tests.

First of all, the multi-head sensor has been calibrated driving the shaker at a known frequency $f_c = 45$ Hz maintaining a constant acceleration $a = 2$g.
The sensors sensitivity, obtained with the proposed calibration procedure is $k = 1$ mV/μm. This value is lower than those evaluated in the previous cases, but this is explainable taking into account a different target reflectivity and a larger distance between the target and the multi-head sensors, due to practical issues in facing the sensor to the DUT.
At this point, two experimental tests have been carried out at two different frequencies in order to mapping in both cases the DUT dynamic behavior and compare the responses.
The first test has been carried out at $f = 45$ Hz. The obtained results are shown in Fig. 6.18, where it is possible notice a measured displacement $D_{\text{ott}} = 0.2$ mm, and also that at this frequency the surface does not present resonance because its response is flat.

The second test has been carried out at frequency $f = 180$ Hz in order to verify the sensor responses at higher frequency.
The obtained results are shown in Fig. 6.19. The displacement is reduced than the previous case but it is expected because of the frequency increasing. Also, the surface response is not flat, that

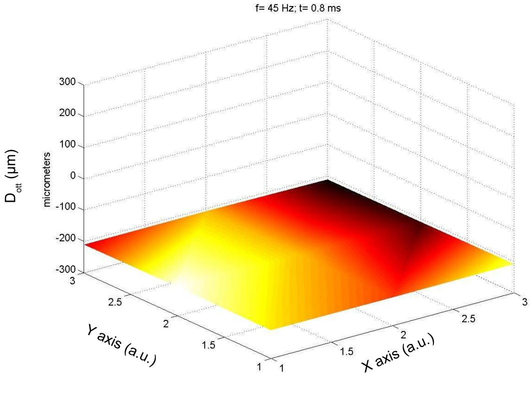

Figure 6.18. Results obtained evaluating the surface displacement evolution at low frequency (f = 45 Hz).

means the presence of mechanical resonances.

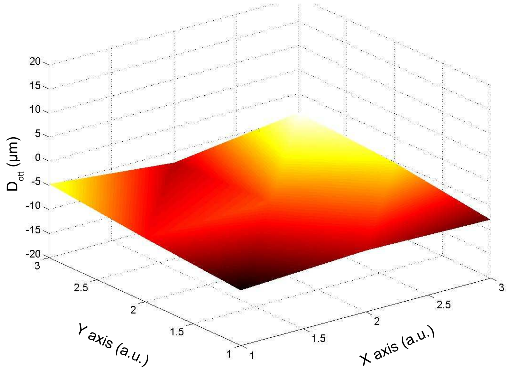

Figure 6.19. Results obtained evaluating the surface displacement evolution at higher frequency than the previous test (f = 180 Hz).

Experimental tests have demonstrated the feasibility of the proposed sensor both in single-head and in multi-head version. The sensor need to be calibrated before each employment to overcome the effects related to non-uniform targets, but the proposed calibration procedure allows characterizing in a easily way simultaneously all the employed sensors, also solving calibration issues, such as the calibration frequency choice and the effects related to the changes of the sensor distance during the test.

Moreover, the experimental results have confirmed a good agreement between the optical sensor and the commercial piezoelectric sensor.

Thus, the proposed sensor is an interesting solution to measure the acceleration of components subjected to vibration tests without contact, with a sub-micrometric resolution, at lower costs in comparison with the employment of traditional piezoelectric accelerometers. [1]

---

[1] The work regarding the proposed fiber vibrometer is also published in [35] [36].

Chapter 7

Development of a compact fiber based accelerometer

7.1 Acceleration monitoring for low frequency vibrations

Measuring acceleration at frequencies up to few hundred of hertz is very useful in many industrial applications, such as vibration tests, or to assess the dynamic behavior of machine moving parts. The measurements of acceleration has to be carried out in harsh environments or in presence of intense electromagnetic fields, as often happens in industrial environments.

The employment of the fiber optic technology can provide a competitive advantage over electromechanical systems, and for this reason, it is very important design a low-cost all fiber accelerometer able to replace the conventional acceleration sensors.

This activity has been developed mainly in the framework of the "Regione Piemonte" funded project called "Laser Factory", in which the goal is the development of a fiber based sensor able to detect accelerations or vibrations of moving arms of high-precision laser cutting and welding machines, whose example is shown in Fig. 7.1. Unwanted small vibrations could result from side effects of the moving actuators, resulting in poor quality cuts. Therefore, it is necessary to improve the stiffness of the arms by controlling these vibrations, and this requires measuring the acceleration in several points.

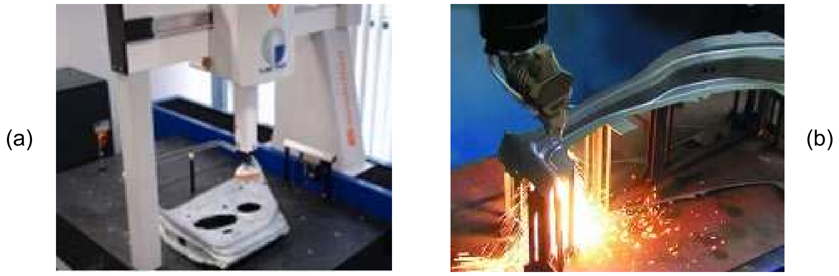

Figure 7.1. Examples of moving arms of laser-cutting (a) and welding machines (b) produced by Prima Industrie.

A large number of fiber accelerometers has been presented in literature over the last years, exploiting different working principles, like those based on a mechanical cantilever [37], [38], [39] or based on FBG sensors, [40], [41] on the fluctuation of the optical power received after a vibrating short span of fiber [42] or target, and based on interferometers.
However, as known, all these systems make use of glass fibers, difficult to handle for users not familiar with fiber technology, but achieving high performances with high costs due to the expensive and complex fiber interrogation system.
Hence, the design and the development of an accelerometer based on plastic optical fibers have been investigated in order to obtain a low-cost fiber acceleration sensor.

7.2 Sensor working principle

The proposed sensor is composed of a mechanical system based on the cantilever structure and a plastic optical fiber span designed to sense the cantilever bending, exploiting the attenuation strong dependence on the fiber curvature radius.
However, the measurement of acceleration with this technique requires an extremely high sensitivity, much higher than that usually achievable from intrinsic bending losses in standard fibers.
This limitation can be easily overcome increasing the fiber sensitivity with curvature through the perturbation of the core/cladding structure of the fiber with a suitable technique, such as by inscribing grooves [43] as shown in Fig. 7.2, that represents a schematic representation of a cutting tool employed to produce the sensitive zone in part of the fiber core (see Fig. 7.2(a)) and of the sensitized fiber (see Fig. 7.2(b)). Then, the grooved fiber is fixed on an elastic cantilever loaded with a seismic mass, as sketched in Fig. 7.3, in order to constitute a "mass- spring-damper" system. This way, the sensitized fiber is able to measure the bending induced from the cantilever curvature subjected to the acceleration, as visualized in the sequence reported in Fig. 7.4, where the arrows represent the optical power at the fiber input, the power lost and the power reflected, respectively.

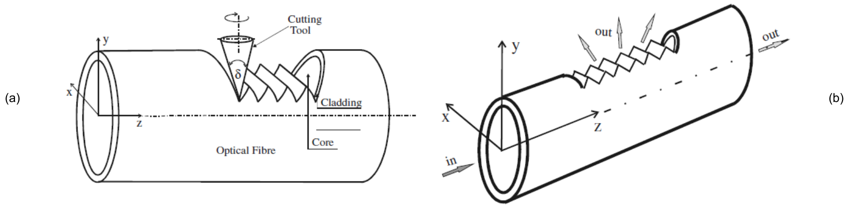

Figure 7.2. A schematic representation of a cutting tool employed to produce the sensitive zone in part of the fiber core (a) and of the sensitized fiber (b).

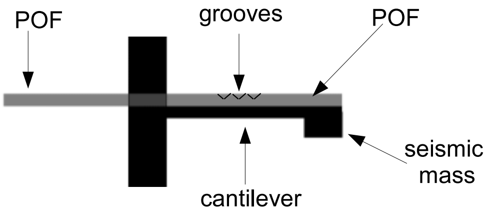

Figure 7.3. Fiber accelerometer layout (lateral view).

7.2.1 Natural frequency of a cantilever structure

Mechanical vibrations theory (assuming that the physical system damping subjected to acceleration has a negligible effect on the physical system natural frequency), allows verifying the proper resonance of a cantilever structure if the cantilever stiffness and weight are known. Taking into account that the cantilever width is negligible with respect to other dimensions, the cantilever

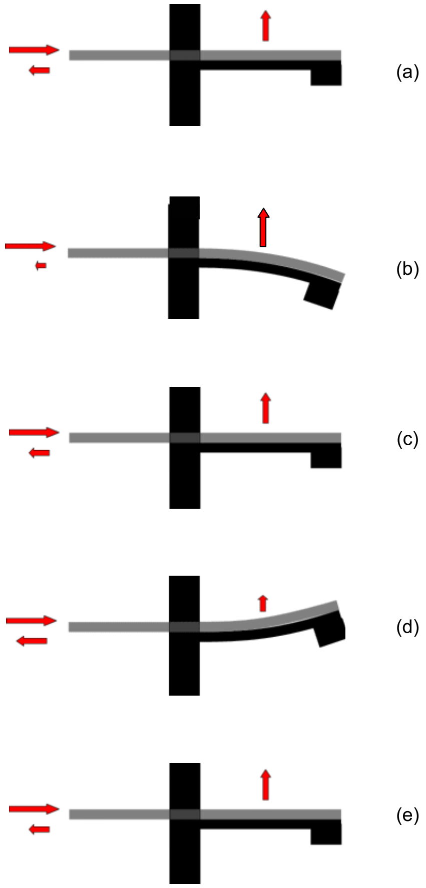

Figure 7.4. Block scheme of the sensor dynamical behavior: horizontal position (no acceleration) (a), down deflection (b), horizontal position (c), up deflection (d), horizontal position (e).

resonance frequency can be evaluated according to Eq. 7.1:

$$f_n = \frac{1}{2 \cdot \pi} \cdot \sqrt{\frac{E \cdot b \cdot h^3}{4 \cdot l^3 \cdot (m + 0.236 \cdot m_B)}} \tag{7.1}$$

where E is the material elasticity's modulus, b, h, l are the width, the thickness and the length of the cantilever respectively, while m and m_B are the seismic and the cantilever mass respectively.

7.2.2 Proposed sensor structures

Two types of sensors have been proposed. The first one, shown in Fig. 7.5, has two sensitized fiber spans connected through a large curvature in order to have both fiber ends on the same side, and also there is a seismic mass on the other side of the cantilever. In this sensor arrangement the light is propagated directly in the photodetector without reflection, and hence the sensor works in *"transmission mode"*. In this structure the minimum width of the cantilever depends on the minimum allowed curvature radius of the fiber to have acceptable curvature induced loss. Consequently, given that the cantilever dimensions (suitable to contain the fiber bent), according to Eq. 7.1, the structure resonant frequency will be small.

On the contrary, the other structure, shown in Fig. 7.6, have been designed with a single sensitized fiber span with a reflecting target placed at its tip and fixed on the cantilever beam.

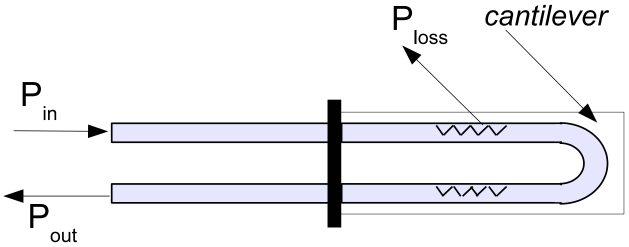

Figure 7.5. Sensor structure designed in transmission mode (top view).

The transmitted optical power is reflected from the target and it is routed to the detector using an optical coupler in order to separate received and transmitted power components. Thus, this sensor works in *"reflection mode"*.

Assuming to employ fibers with the same diameter in both the proposed structures, since in the sensor working in reflection mode there is a single fiber span, it requires a smaller cantilever (to dimensioned to contain only one span) and consequently will be an higher resonant frequency, according to Eq. 7.1, and also a wider frequency range.

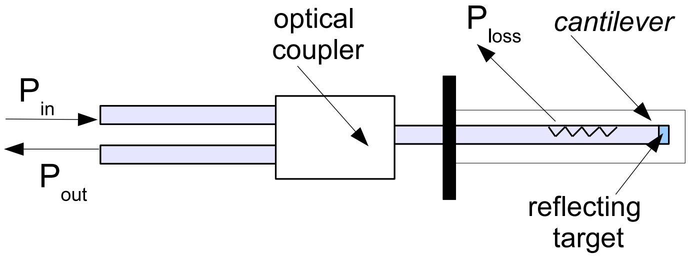

Figure 7.6. Sensor structure designed in reflection mode (top view).

7.3 Prototypes

Some prototypes have been realized both in transmission and in reflection mode and also without or with grooves on the fiber surface in order to evaluate the feasibility of the proposed structures.

7.3.1 In transmission mode

A first prototype of sensor working in transmission mode has been arranged according to the structure shown in Fig. 7.5.
The cantilever is an aluminum bar having 8 cm length, 3 cm width and 1.5 mm thickness, also with a tip free to move. At the same cantilever tip, an aluminum seismic mass of 250 g is fixed.
The fiber is general purpose, unjacketed, with Step Index refractive profile, a large core of Poly-Methil-MethAcrylate (PMMA) surrounded by a thin cladding made of fluorinated polymer for a total diameter of 0.5 mm and 2 m length.
The fiber has been fixed on the cantilever surface in order to have both fiber tips on the same side and leave the seismic mass free to move on the other side. A portion of the fiber of about 1 cm length has been grooved manually by means of a cutter. Finally, holes have been produced on the cantilever beam in order to reduce its stiffness and consequently distinguish the accelerations.
The arranged sensor prototype is shown in Fig. 7.7, which has been taken in dark conditions to highlight the optical power losses due to the grooves in the fiber core.

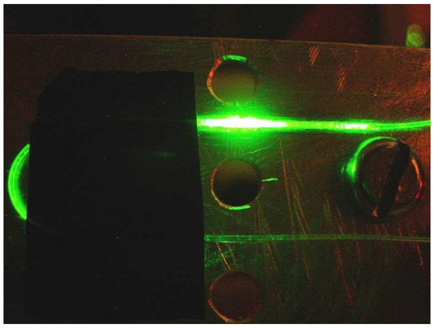

Figure 7.7. A detail of a sensor prototype realized in transmission mode.

7.3.2 In reflection mode

The sensor in reflection mode seems to be more promising than the other one in order to realize a compact fiber device, because it requires only a fiber span. So it is possible to decrease the cantilever dimensions and also the sensor size. For this reason, a prototype working in the reflection mode has been arranged, employing a SI PMMA POF with a diameter of 1 mm, larger than in the previous case, because the larger is the diameter, greater is the fiber bending sensitivity and also better is the signal to noise ratio.
Since this prototype has been designed to work in the reflection mode, only a single fiber span is required to be fixed on the cantilever, and hence the cantilever can be realized with reduced dimensions, decreasing the sensor size, and increasing the expected resonance frequency and consequently the sensor working region.

In particular, this cantilever beam has been realized through a thin copper bar having 2 cm length, 0.5 cm width and 0.5 mm thickness, with a light copper mass positioned on the bottom side of the cantilever tip free to move, whereas on the top of the cantilever the fiber span is fixed. Here, a fiber tip is very close to the reflecting target, that is a circular aluminum foil allowing the reflection of the light back, whereas the other tip is connected to a commercial 3-dB coupler that separates the input and the reflected optical power and hence routes the detected light to the receiver.
Two prototypes of sensors working in reflection mode have been realized. One, shown in Fig. 7.8, doesn't present the grooves, whereas the other prototype, shown in Fig. 7.9, is arranged as the previous but has a grooved fiber portion of about 1 cm length. The aim is a comparison between the prototypes without and with sensitized fiber in order to verify experimentally how the sensitivity increases employing the grooved fiber.

Figure 7.8. Detail of the sensor prototype realized in reflection mode without grooves on the fiber surface.

Since the cutting procedure is currently a manual operation done with a cutter, it is evident that the obtained cuts are not so easily reproducible.
For this reason, an automatic cutting tool, based on a fiber laser, is currently under investigation.

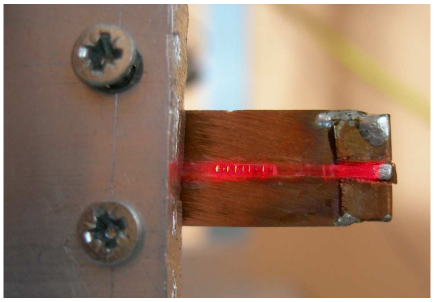

Figure 7.9. Detail of the sensor prototype realized in reflection mode with grooves on a portion of the fiber surface.

7.4 Experimental setup

An experimental setup has been realized in order to verify the dynamical behavior of the developed prototypes, using the available electrodynamic shaker and the vibrating table, already employed to carry out the vibration tests described in the previous chapter.
Fig. 7.10 shows the setup arranged to test the fiber accelerometer structured in transmission mode, where are also present the shaker and the related vibrating table, on which the cantilever structure has been fixed and the interrogation circuits allowing to detect the sensor response.
The light source is a commercial green LED driven at constant current while the receiver is composed of a photodiode connected to a transimpedance amplifier with gain $G = 300\ \mathrm{M}\,\Omega$, such as the one explained describing the interrogation circuit employed for the optical displacement sensor. The conditioning circuit is followed by a data acquisition board connected with a PC in order to elaborate the received data.
Fig. 7.11 shows the setup arranged to test the fiber accelerometer structured in reflection mode, both in lateral and front view.

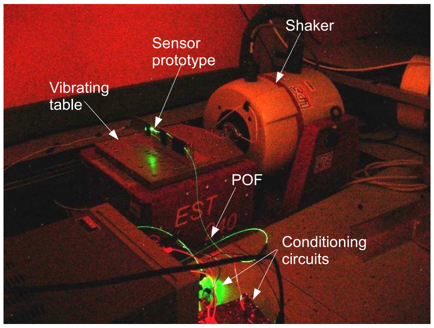

Figure 7.10. Setup arranged to test the prototype in transmission mode during sinusoidal vibration tests.

The arranged setup is very similar to the previous one, with the difference that the source is a red led, because among the optical devices available in laboratory, the choosen LED has the high optical power and the photodiode presents a high responsivity at red wavelength.
Fig. 7.12 shows the sensitized prototype in reflection mode arranged to be tested, where the setup is the same employed for the sensor arranged in reflection mode without grooves.

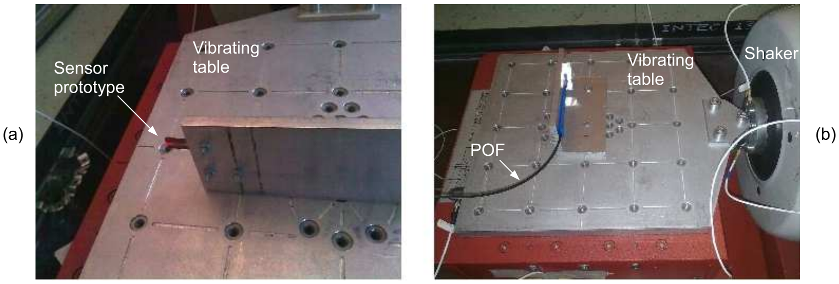

Figure 7.11. Setup employed to test the prototype without grooves in reflection mode: lateral (a) and front view (b).

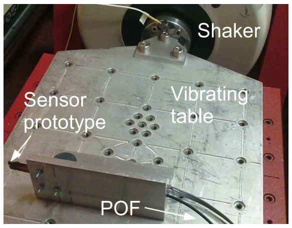

Figure 7.12. Setup employed to test the sensitized prototype in reflection mode: lateral view.

7.5 Experimental sensor characterization

Prior to running the experiments, the expected resonance peaks for both prototypes have been evaluated analytically to establish on which frequency range execute the sinusoidal vibration tests. According to Eq. 7.1, considering the physical characteristics of the cantilever, loaded with the seismic mass, and considering negligible the effect of the glued fiber on the cantilever, the resonance frequencies are about $f_n \approx 23$ Hz and $f_n \approx 204$ Hz respectively for the prototype in transmission and in reflection mode.

Then, some sinusoidal vibration tests had been carried out to verify the dynamical behavior of the developed prototypes, forcing a constant known acceleration by means of the shaker and simultaneously detecting the sensor prototype response.

Finally, since the shaker is able to control in real time the acceleration signal, it is possible to exploit this information to characterize experimentally the prototypes under test, combining the sensors measured voltages with the provided acceleration information in order to obtain the sensor sensitivity.

7.5.1 Prototype in transmission mode

The sensor prototype of Fig. 7.7 has been tested under sinusoidal excitation to verify its dynamic behavior, forcing a constant acceleration at $a \approx 5\,\mathrm{m}/s^2$ while changing the frequency from 5 Hz to 150 Hz, which is the range that contains the expected resonance peak.

An example of the obtained results is shown in Fig. 7.13, where it is possible to distinguish the resonant peak at a frequency of about 18 Hz.

This value is slightly lower than that expected, but this difference can be explained considering that the used cantilever beam had some holes made on purpose to decrease the structure stiffness in order to distinguish the accelerations, whereas they were considered negligible to simplify the structure model during the analytical evaluation of f_n through Eq. 7.1. The sensor behavior has the typical response of a second order system.

The useful sensor working range is limited up to few hertz because of the resonance peak position, but the detected signal in this range is about 100 mV. Hence, the sensor sensitivity results S = 200 mV/g.

7.5.2 Prototype in reflection mode without grooves

An experimental test under sinusoidal conditions has been carried out to verify the dynamic behavior of the prototype arranged in reflection mode without grooves, shown in Fig. 7.8. The sensor response has been measured maintaining the acceleration constant, forced by means of the shaker,

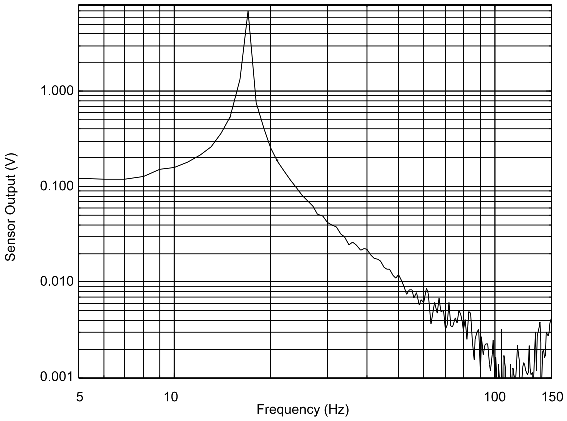

Figure 7.13. Measured sensor response during a sinusoidal vibration test carried out at constant acceleration in order to evaluate the dynamic behavior of the prototype arranged in transmission mode.

at 4 g, and changing the frequency from 50 Hz to 500 Hz, which is the range that contains the expected resonance peak for this prototype.

The measured sensor response is shown in Fig. 7.14, where the resonance peak appears at a frequency about of 210 Hz, which is slightly higher than the theoretical value of 204 Hz, but this latter has been obtained considering negligible the mass of the glued fiber.

It is also possible show that in the sensor working region (before the resonance) the signal level is low and about 1.5 mV.

Hence, the sensor sensitivity in the useful region results to be $S = 1.5$ mV/g.

This poor sensitivity, expected and reasonable because the fiber has not been sensitized yet, anyway allows demonstrating the feasibility of the proposed approach.

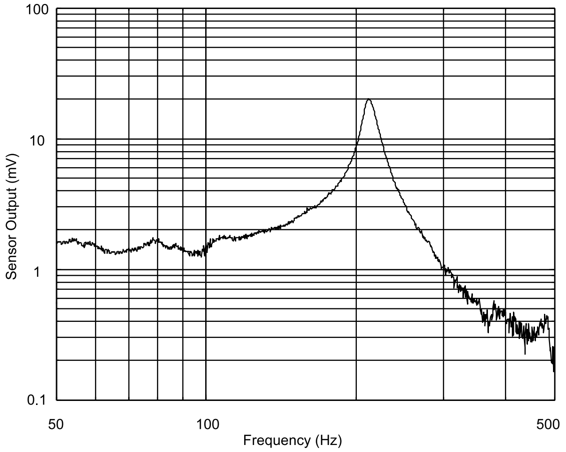

Figure 7.14. Measured output from the prototype arranged in reflection mode without grooves during a sinusoidal vibration test carried out at constant acceleration.

7.5.3 Prototype in reflection mode with grooves

The prototype arranged in reflection mode with grooves in part of the fiber span, has been shown in Fig. 7.9. It has been tested in sinusoidal conditions, forcing a constant acceleration of about 1 g and changing the frequency from 50 Hz to 500 Hz.
The sensor response is shown in Fig. 7.15. The sensor sensitivity is about S = 4.5 mV/g.
This result demonstrates experimentally the importance of the grooves in order to increase the sensor sensitivity to the cantilever bending.
Moreover, because the cantilever dimensions and the seismic mass are the same as in the previous case, the measured frequency resonance peak is at the same frequency of about 210 Hz, as expected.

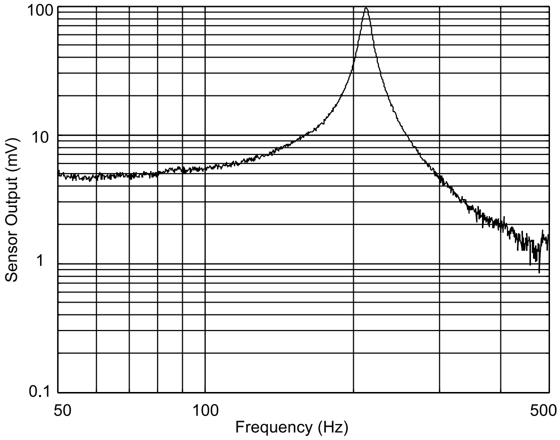

Figure 7.15. Measured output from the prototype arranged in reflection mode with grooves during a sinusoidal vibration test carried out at constant acceleration.

The experimental tests have shown the feasibility of the proposed approaches [1].
The sensor working in reflection mode seems to be more promising since it has reduced dimensions, requiring a smaller cantilever because of only a single fiber span and a reflecting target.

The next activities will be focused on a further reduction of the sensor dimensions and an improvement of the sensitivity.
Also, it provides the development of an automatic grooving procedure, that is currently under investigation, the noise reduction of the interrogation circuits, and the selection of the optimal fiber diameter and LED wavelength.

---

[1] The work regarding the proposed fiber accelerometer is also published in [44].

Chapter 8

Conclusions

The thesis has presented an overview of the research activities carried out while working toward the doctorate in *"Metrology: measuring science and technique"*.

First, the characteristics of Plastic Optical Fibers (POF) have been introduced. Then, the development of innovative fiber sensors for the measurement of displacements and vibrations has been described, reporting also examples of practical applications.

POF have been chosen for the fabrication of the sensors instead of the more common glass fibers, like those used in telecom applications. The characteristics of plastic fibers make them a good platform to develop sensors for applications that require the advantages of fibers but with the costs of electro-mechanical systems.

All the studied sensors have been developed and characterized.

These sensors relate the quantity under measure with the changes of the light intensity along an optical link composed of one or more fiber spans and for this reason, they are namely "intensiometric" sensors. The developed sensors can be divided into three groups according to their use:

- **Sensors for monitoring displacement in one and two directions**:
  sensors that exploit the light received from a fiber either facing a reflective target or another fiber and that can be moved longitudinally (for one dimensional sensors) or transversally (for two dimensional sensors).
  Advantages and drawbacks of this type of sensors have been analyzed in detail and possible approaches to overcome their limitations have been proposed and tested, also in long-term monitoring applications.
  These applications represent the worst possible case since the measurements obtained in the long-term are affected by parasitic effects, such as temperature, humidity, fiber aging, electronic circuit drifts.
  A working range of ±3 mm with a short-term accuracy of 0.01 mm and a long-term accuracy of 0.1 mm have been achieved.
  A typical application of this sensor is the long-term monitoring of cracks in cultural heritage preservations.
- **Sensors for measuring vibration amplitude and frequencies without contact**:
  sensors that evaluate the vibration characteristics through the changes of the power received

by a fiber facing the vibrating surface.
Both single-point and multi-point sensing head has been developed in order to map the vibration modes of the DUT surface.
A procedure to calibrate the sensors regardless of target reflectivity has been devised and assessed by comparison with a reference piezoelectric accelerometer.
Experimental test results have shown that the sensor can detect vibration amplitudes as low as 80 nm over a frequency range extending up to few kilohertz.
A typical application is in vibration tests of devices, such as printed circuit boards (PCBs).

- **Sensors for measuring acceleration exploiting the modulation of propagation loss with fiber micro-bending**:
  these sensors are fiber-based but made by fixing the plastic fiber on a metallic cantilever with a suitable shape. Two structures have studied, one in transmission mode and the other in reflection mode. The preliminary results have demonstrated that the structure arranged in reflection mode is more promising because it can be realized with reduced dimensions than the other one. However, the metrological characterization of these sensors is still under investigation.

Bibliography

[1] D.A. Krohn, "*Fiber optic sensors - fundamentals and applications*", ISA - The instrumentation, systems and automation society, 2000.

[2] B. Glisic, D. Inaudi, *"Fibre optic methods for structural health monitoring"*, John Wiley and Sons Ltd, 2007.

[3] D.C. Lee, J.J. Lee, I.B. Kwon, D.C. Seo, "*Monitoring of fatigue damage of composites structures by using embedded intensity-based optical fiber sensors*", Smart Mater. Struct, vol. 10, pp. 285-292, 2001.

[4] L.K. Cheng, "*High-speed dense channel fiber Bragg grating sensor array for structural health monitoring*", Proc. of IEEE conf. on NANO and Smart Systems, 2005.

[5] G. Zhou, L. M. Sim, *"Damage detection and assessment in fibre-reinforced composite structures with embedded fibre optic sensors-review"*, Smart Mater. Struct., Vol. 11, N. 6, pp. 925-940, 2002.

[6] R. Dib, Y. Alayli, P. Wagstaff, "*A broadband amplitude-modulated fibre optic vibrometer with nanometric accuracy*", Measurement, Elsevier Science, vol. 35, pp. 211-219, 2004.

[7] V.A. Pliem, S. Scheibelhofer, G. Brasseur, "*Crack detection on an escalator handrail*", Proc. of I2MTC 2002, pp.1001-1005, Anchorage, Alaska, May 21-23th, 2002.

[8] $http://www.philtec.com$

[9] K. Peters, S. Kiesel, O. Abdi, T. Hassan, M. Kowalsky, *"Intrinsic Polymer Optical Fibers for large deformation strain sensors"*, SPIE Newsroom, 10.1117/2.1200802.1065.

[10] S. Binu, V. P. Mahadevan Pillai, N. Chandrasekaran, *"Fibre optic displacement sensor for the measurement of amplitude and frequency of vibration*, Opt. Laser Technol., vol. 39, pp. 1537-1543, 2007.

[11] A. Babchenko, Z. Weinberger, N. Itzkovich, J. Maryles, *"Plastic optical fibre with structural imperfections as a displacement sensor"*, Meas. Sci. Technol., vol. 17, pp. 1157 - 1161, 2006.

[12] $http://www.prginc.com/Masonry/PRG - crackmon_1.html$

[13] $www.micro - epsilon.com$

[14] J.B. Faria, *"A Theoretical Analysis of the Bifurcated Fibre Bundle Displacement Sensor"*, IEEE Trans. Instrum. Meas., vol. 47, no. 3, pp. 742-747, 1998.

[15] G. Perrone, A. Vallan, *"A Low-Cost Optical Sensor for Noncontact Vibration Measurements"*, IEEE Trans. Instrum. Meas., vol. 58, no. 5, pp. 1650 - 1656, 2009.

[16] G. Perrone, M. Olivero, A. Vallan, A. Carullo, A. Neri, "*Long Term In-Situ Test of a Low-Cost Fiber-based Crack Monitoring System*", Proc. of IEEE Sensors Conf. (Sensors2008), Lecce, Italy, Oct 26-29th, 2008.

[17] M. L. Casalicchio, A. Penna, G. Perrone, A. Vallan, "*Optical Fiber Sensors for Long- and Short-Term Crack Monitoring*", Proc. of IEEE Workshop on Environmental, Energy, and Structural Monitoring Systems (EESMS2009), Crema, Italy, Sep 25th, 2009.

[18] O. Ziemann, J. Krauser, P.E. Zamzow, W. Daum, "*POF Handbook: Optical Short Range Transmission Systems*", ed. Springer, 2nd Edition, 2008.

[19] A. Appajaiah, "*Climatic Stability of Polymer Optical Fibers (POF)"*, BAM Dissertation Series (available on line), Vol. 9, 2005.

[20] M.L. Casalicchio, M. Olivero, A. Penna, G. Perrone, A. Vallan, *"POF Sensor for Measuring 2D-Displacements in Structural Momintoring"*, Proc. of POF 2011, Bilbao, Spain, September 14 - 16th, 2011.

[21] M.L. Casalicchio, G. Perrone, A. Penna, A. Vallan, "*Distributed POF sensor network for crack monitoring in buildings*, Proc. of POF Conf. 2010 (POF 2010), Yokohama, Japan, Oct 19-21th, 2010.

[22] M.L. Casalicchio, D. Lopreiato, A. Penna, G. Perrone, A. Vallan, "*POF Sensor Network For Monitoring The Guarini Chapel*", Proc. of POF Conf. 2011 (POF 2011), Bilbao, Spain, Sept 14-16th, 2011.

[23] D. S. Montero, C. Vázquez, I. Möllers, J. Arrúe , D. Jäger, "*A Self-Referencing Intensity Based Polymer Optical Fiber Sensor for Liquid Detection*", vol.9, Sensors, pp. 6446-6455, 2009.

[24] M. Olivero, G. Perrone, A. Vallan, "*Compensation of the power fluctuations in intensity-based plastic optical fiber sensors*, Proc. of Optical Fiber Communication Conf. (OFC2009), San Diego, CA, U.S.A., Mar 22-26th, 2009.

[25] M.L. Casalicchio, M. Olivero, G. Perrone, A. Penna, A. Vallan, "*Compensation Techniques for low-cost intensity-based POF displacement sensors*, Proc. of POF Conf. 2010 (POF 2010), Yokohama, Japan, Oct 19-21th, 2010.

[26] M.L. Casalicchio, M. Olivero, G. Perrone, A. Vallan, "*Plastic Optical Fiber Sensor for Displacement Monitoring with Dual-Wavelength Compensation of Power Fluctuations*", Proc. of I2MTC 2011, Hangzhou, May, 10-12th, pp. 832-836, 2011.

[27] A. Vallan, M.L. Casalicchio, M. Olivero, G. Perrone, "*Assessment of a Dual-Wavelength Compensation Technique for Displacement Sensors Using Plastic Optical Fibers*", accepted for the publication in IEEE Trans. Instrum. Meas. 2012

[28] S. Donati, *"Electro- optical instrumentation: sensing and measuring with lasers"*, Upper Saddle River: Prentice Hall, 2004.

[29] A. Link, H. J. Von Martens, *"Amplitude and phase measurement of sinusoidal vibration in the nanometer range using laser interferometry "*, Measurement 24, Elsevier, pp. 55-67, 1998.

[30] P. Castellini, M. Martarelli, E.P. Tomasini, *"Laser Doppler Vibrometry: Development of advanced solutions answering to technology's needs"*, Mech. Syst. Signal Process., vol. 20, no. 6, pp. 1265-1285, 2006.

[31] A. Chijioke, J. Lawall, *"Laser Doppler vibrometer employing active frequency feedback"*, Appl. Opt., vol. 47, pp. 4952-4958, 2008.

[32] F. Suganuma, A. Shimamoto, K. Tanaka, *"Development of a differential optical - fiber displacement sensor"*, Appl. Opt., vol. 38, no. 7, 1999.

[33] H. Cao, Y. Chen, Z. Zhou, G. Zhang, *"General models of optical fiber - bundle displacement sensors"*, Microwave Opt. Tech. Lett., vol. 47, no. 5, 2005.

[34] R. O. Cook, C. W. Hamm, *"Fiber optic lever displacement transducer"*, Appl. Opt., vol. 18, no. 19, pp. 3230-3241, 1979.

[35] M.L. Casalicchio, G. Perrone, A. Vallan, *"A Fiber Optic Sensor for Displacement and Acceleration Measurements in Vibration Tests"*, Proc. of I2MTC 2009, Singapore, May 5-7th, pp. 1676-1680, 2009.

[36] M.L. Casalicchio, G. Perrone, A. Vallan, *"Displacement and Acceleration Measurements in Vibration Tests Using a Fiber Optic Sensor"*, IEEE Trans. Instrum. Meas., vol. 59, n. 5, pp. 1389-1396, 2010.

[37] J. Kalenik, R. Pajak, *"A cantilever optical fiber accelerometer"*, Sens. Actuators, vol. A 68, pp. 350-355, 1998.

[38] F.R. Barbosa, F. Borin, A. Arakaki, J.G.D. Aguiar, C. Chaves, *"A novel optical accelerometer"*, Proc. of IMOC 2005, Brasilia, Brazil, July 2005.

[39] J.M. Lopez-Higuera, M.A. Morante, A. Cobo, *"Simple low-frequency optical fiber accelerometer with large rotating machine monitoring applications"*, J. Lightw. Technol., vol. 15, no. 7, pp. 1120-1130, 1997.

[40] T.A. Berkoff, A.D. Kersey, *"Experimental demonstration of a Fiber Bragg Grating accelerometer"*, IEEE Photon. Technol. Lett., vol. 8, no. 12, pp. 1677-1679, 1996.

[41] P.F. da Costa Antunes, H.F.T. Lima, N.J. Alberto, H. Rodrigues, P.M.F. Pinto, J. de Lemos Pinto, R.N. Nogueira, H. Varum, A.G. Costa, P.S. de Brito Andr, *"Optical fiber accelerometer system for structural dynamic monitoring"*, IEEE Sensors J., vol. 9, no. 11, pp. 1347-1354, 2009.

[42] V.T. Chitnis, S. Kumar, D. Sen, *"Optical fiber sensor for vibration amplitude measurement"*, J. Lightw. Technol., vol. 7, no. 4, pp. 687-691, 1989.

[43] M. S. Kovacevic, D. Nikezic, A. Djordjevich, *"Monte Carlo simulation of curvature gauges by ray tracing"*, Meas. Sci. Technol., vol. 15, pp-1756-1761, 2004.

[44] M.L. Casalicchio, C. Fallauto, A. Penna, G. Perrone, A. Vallan, *"Compact POF Accelerometer"*, Proc. of POF 2011, Bilbao, Spain, September 14 - 16th, 2011.

[45] A. Laudati, F. Mennella, M. Giordano, G. D'Altrui, C. Calisti Tassini, A. Cusano, *"A Fibre-Optic Bragg Grating Seismic Sensor"*, IEEE Photon. Technol. Lett., vol. 19, no. 24, pp.1991-1993, 2007.

[46] S. Lee, S. Saini, M. Jeong, *"Simultaneous Measurement of Refractive Index, Temperature, and Strain Using Etched-Core Fiber Bragg Grating Sensors"*, IEEE Photon. Technol. Lett., vol. 22, no. 19, pp. 1431-1433, 2010.

Appendix A

Optical fibers and fiber optic sensors

This appendix reports the fundamental aspects regarding the optical fibers, also highlighting the plastic optical fibers characteristics, and a fiber optic sensors classification.

A.1 Optical fibers

Optical fibers are optical waveguides that propagate the light. A fiber is basically composed of two cylinders: the inner part is the *core* and the surrounding is the *cladding*, as shown in Fig. A.1. Fibers have been characterized from an optical parameter depending on their material composition, that is *refractive index.* The refractive index is the parameter describing the optical density of that material and it is the ratio between the light velocity in the vacuum and in the medium. Hence, each optical fiber is characterized by *core refractive index* and *cladding refractive index* and the light propagation in the fibers depends mainly on them.

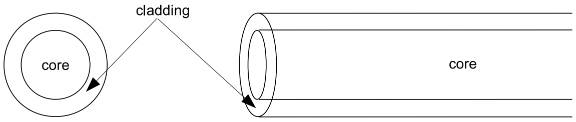

Figure A.1. Front and lateral view of an optical fiber.

A.1.1 Light propagation into the fiber

The light can propagate from a material with low refractive index n_1 to another material with high refractive index n_2, as shown in Fig. A.2(a) or in the opposite way, as shown in Fig. A.2(b). The total internal reflection (TIR) occurs when the refractive index of the first medium is higher than the refractive index of the second one.

In the fibers TIR happens when the core material has a refractive index higher than cladding refractive index, or rather for every angle $\theta < \theta_{max}$, where θ is defined as the angle between the incident ray and the fiber axis, while θ_{max} is the maximum value beyond which there is no total

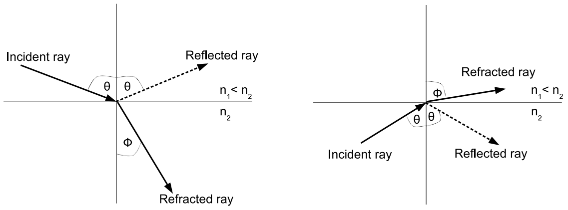

Figure A.2. Light propagation from a medium with low refractive index to one with high refractive index (a) and the opposite case (b).

internal reflection. This value is a threshold depending on the refractive indexes according to Eq. A.1:

$$\theta_{max} = \arcsin \sqrt{n_{core}^2 - n_{cladding}^2} \tag{A.1}$$

The angle θ_{max} is defined also as the half angle of the *Acceptance Cone*, as shown in A.3. For an

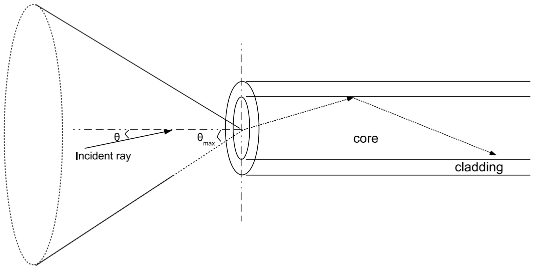

Figure A.3. Definition of light cone.

optical system, and therefore for the fibers, θ_{max} is related with *Numerical Aperture* (NA), a very important parameter characterizing the fiber, that is defined in Eq. A.2:

$$NA = n_0 \cdot \sin \theta_{max} \tag{A.2}$$

where n_0 is the refractive index of the means surrounding the fiber, that usually is air, and consequently n_0 is equal to one. For each external light ray that forms an incidence angle $\theta < \theta_{max}$ with the fiber axis, the light propagates along straight lines in the core and is theoretically completely reflected at the core/cladding interface.
There are two types of propagation in the fibers: single mode and multi mode, and the number of propagating modes depends on the V-parameter, reported in the following equation:

$$V = \frac{2\pi \cdot r_{core}}{\lambda} \cdot NA \tag{A.3}$$

where r_{core} is the core radius, λ is the light wavelength, NA is the numerical aperture.
If $V < 2.405$ only one mode can propagate and the fiber is monomodal or single-mode. Otherwise, the fiber is multimode and the number of modes depends on the index profiles fiber.

Refractive index profiles

The properties of wave guiding through a fiber are governed largely by the profile of the refractive index of the core and cladding. The main index profiles fibers are Step Index (SI) and Graded Index (GI).
In a SI profile fiber, the refractive index is constant across the entire cross section of the core and cladding and between two materials there is a definite step.
Instead, in the GI profile fiber, the core has a radius-dependent refractive index and the cladding refractive index is constant. Hence, the light propagates on a sinusoidal trajectory that is created within the graded-index profile through refraction.
Anyway, if the fiber is multimode, the number of modes results approximately: $N \approx \frac{V^2}{2}$ and $N \approx \frac{V^2}{4}$ respectively for SI and GI profiles.

A.1.2 Optical fibers characteristics

In addition to the light propagation inside the fibers, several parameters characterize the fiber behavior, and hence they are briefly described below.

Material composition

The refractive indexes depend on from the material types of which the fiber is composed. The main division is between *glass fibers* and *plastic fibers*.
Glass fibers have lower attenuation, wider transmission bandwidth and smaller size than the corresponding plastic ones. Unfortunately, the glass fibers handling during production, splicing and installation processes can be quite difficult and also glass fibers are quite fragile.
On the contrary, plastic fibers are easier to employ, because of diameter, up to few millimeters, and high flexibility for high Young's modulus. Unfortunately, in their working range, that is the visible light, they have a very high attenuation, depending mainly from light wavelength.
Typically, glass fibers are singlemode, while plastic optical fibers are multimode. Most of the glass fibers are based on silica (SiO_2) glasses doped with Germanium dioxide or Aluminum oxide to increase the core refractive index and with fluorine or Boron trioxide to decrease the cladding refractive index. In this way, the refractive indexes are modified but the good transmission characteristics of silica are maintained.
Instead, the major part of plastic optical fibers are based on polymeric materials.
Traditionally PolyMethylMethachrylate (PMMA) is employed for the core and fluorinated polymers constitute the cladding. Also, it is possible employ other compounds of perfluorinated polymers to increase the fiber performance. Obviously, the choice between glass or optical fibers depends on the specific application and available budget.

Attenuation

The attenuation coefficient α is expressed in decibel/kilometers and it is defined as:

$$\alpha = \frac{10}{L} \cdot \log \frac{P_0}{P_L} \tag{A.4}$$

where P_0 and P_L are respectively the optical power at the front end of the fiber and after a certain length L of the fiber.

Dispersion

Dispersion refers to all processes that result in a difference in the transit times of various modes of propagation. The most significant contributions are chromatic dispersion and mode dispersion if the fiber is multimode.
Chromatic dispersion describes the influence of the spectral width of a transmitter on a temporal broadening of the input pulse, and includes two effects: waveguide-dispersion and material-dispersion.
Waveguide dispersion is caused by the fact that light waves penetrate into the fiber cladding to various depths, depending on the wavelength of the light wave. Thus, the different speeds of the core and cladding parts result in pulse broadening. Fortunately, only a small portion of the light wave in higher modes of large diameter fibers spreads into the cladding, then this effect is not so relevant.
Furthermore, a pulse broadening can occur due to material dispersion due to the spectral width of the source.
Chromatic dispersion for typical materials employed in fibers is reported in Fig. A.4 [18].

At the beginning of the fiber the pulses are launched simultaneously, but since the light paths have different lengths, i.e. due to modal coupling, the pulses arrive at different times at the output of the fiber.
In fact, in shortest paths the pulse comes first, in longest ones, the pulse arrives late and the delay leads to pulse broadening. The differential delay increases approximately by the square of the angle relative to the fiber axis.
The propagation times of the two different propagation paths can be determined in a geometric way having as information the path length, the core refractive index and the light velocity.

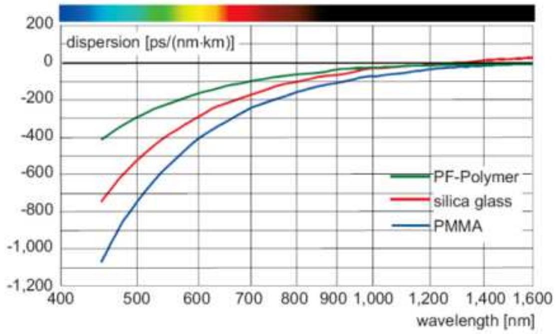

Figure A.4. Dispersion of materials commonly used to realize fibers: silica for glass fibers, PMMA for core and a perfluorinated (PF) polymer for cladding of plastic optical fibers.

Absorption

Absorption is caused by impurities in the material and refers to the conversion of optical energy into either optoelectronic activity or molecular vibrations. The amount of absorption by these impurities depends on their concentration and the light wavelength.

Scattering

Scattering is a result of imperfections in the basic structure of the fiber.
There are two main types: *Rayleigh* and *Mie* scattering.
Rayleigh scattering is caused by material inhomogeneities, regions with slightly different density or composition, which cause fluctuations in the refractive index, taking account that the inhomogeneities are much smaller in size than the wavelength of light. Rayleigh scattering produces an attenuation increase and is proportional to the reciprocal of the fourth power of the wavelength. Unfortunately, the incidence angle of rays striking an inhomogeneity are refracted on to new paths which are not subject to TIR.
Mie scattering is defined when the inhomogeneities size is comparable with the light wavelength dimension. It's linear scattering that occurs from imperfections in the fiber's geometry or irregularities in the refractive index often caused during fiber manufacturing process. Thus, a careful control of the fiber manufacture can reduce significantly this effect.

Bending losses

Bending losses are generally defined as losses due to the fiber curvature or an abrupt change in radius of curvature. For this reason, one significant parameter for an optical fiber is the *minimum bending radius*, that is threshold value beyond which the transmitting characteristics of the fiber degrade strongly and consequently the attenuation increases.
It is possible distinguish two types of bending: *macrobending* and *microbending*.
The first type is associated to an attenuation due the light escaping out of the fiber because the fiber is bent or wrapped.
On the contrary, microbending occurs when physical irregularities, described as random variables with a distribution of spacing and amplitude, are present on the fiber surface and perturb the light propagation. In fact, these perturbations couple power among modes in the fiber and the power can be dissipate through scattering.

Field distribution

Field distribution is defined according to the section where is measured.
The *near field* describes the power distribution of the light in the output face of the optical fiber. The *far field* is defined through the field distribution at the distance D from the output face of the fiber at least equal to $D \gg 2 \cdot a$ where a is the fiber core radius, and it represents the intensity distribution on a spherical surface, in the center of which the light output face is located. In most cases, during the detection of the fiber output signal, the power measurements are carried out in far field conditions.

Mode distribution

When a steady state mode distribution is achieved and remains constant, this condition is defined *Equilibrium Mode Distribution* (EMD).
It is very different from the mode distribution excited at the beginning of the fiber, where all modes have initially the same power whenever the acceptance cone is illuminated completely (full filled launching). This condition is defined *Uniform Mode Distribution* (UMD).

A.2 Plastic Optical Fibers

The first point concerns the name: POF is the acronym of Plastic Optical Fiber but often it is employed not properly for the synonym Polymer Optical Fiber.

A.2.1 Chemical characteristics

In the most cases the polymeric materials employed to realize a plastic fiber are PolyMethyl-Methachrylate (PMMA), better known as *Plexiglas*, for the core and fluorinated or perfluorinated polymers for the cladding. PMMA is a water resistant organic compound with an amorphous structure. Its polymeric chain is derived from a monomer composed of ethylene, hydrocyanic acid and methyl alcohol, of which structure is shown in Fig. A.5. Its organic composition allows to absorb a certain quantity of water, depending on temperature and relative humidity conditions, that also affects the fiber attenuation characteristics.
The power losses due to absorption of water in the PMMA chain depend on the wavelength of the light transmitted in the fiber; in particular around at 627 nm (red light) and 736 nm (UV) this effect is not negligible, absorbing up to 1.5% of water due to C-H bonds present in the polymeric chain.

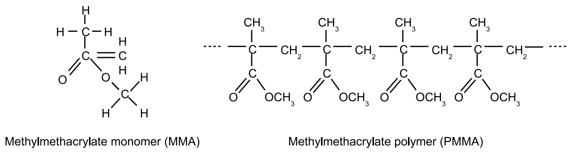
Methylmethacrylate monomer (MMA)
Methylmethacrylate polymer (PMMA)

Figure A.5. Molecular structure of monomer and polymeric chain of Methylmethacrylate.

A.2.2 Physical properties

The fiber diameter is included about between 0.1 mm and 3 mm but the typical value is 1 mm; in this case the core diameter is 980 μm and the cladding one is 20 μm.
For this reason the fiber is easy to handle and connect with other fibers.

A.2.3 Optical characteristics

The optical parameters characterizing a POF are: refractive index profile, numerical aperture, attenuation, dispersion, absorption, scattering, bending, field and mode distribution.
In a POF the numerical aperture is a value very close to 0.5 because it depends on the compounds of PMMA employed for the core and the cladding. Typically, a PMMA core has a refractive index of 1.492.
The high value of NA allows to the fiber of collect a considerable amount of light as the power coupled into the fiber is high.
Also, the bending sensitivity and the connecting loss for fiber angular mismatch are smaller than the case with a low value of NA, while connecting losses for axial fiber gap and for fiber axis lateral gap are higher.
As the plastic fiber is multimodal, due to the modal dispersion, the modes start together but arrive at the fiber end at different times because of light paths with different lengths. Differential delays between these light components lead to a reduction in the modes amplitude at higher frequencies,

making the POF a sort of low-pass filter.
Another aspect depending on the light wavelength and fiber material composition is power loss due to Rayleigh scattering, i.e. for PMMA the attenuation is about 12 dB/km at 650 nm (red light) and increases up to 28 dB/km at 520 nm (green light).
The field and the mode distribution can act on the bandwidth in a fiber, but the bandwidth is not a critical parameter employing the fiber to realize fiber sensors.
Between the optical parameters characterizing a POF, the attenuation and the bending are very critical and for this reason they are explored in detail.

POF attenuation

At first, for a POF, contrariwise of the glass fiber, is not possible assume that the attenuation depends only on the fiber length and it is identical for all propagating modes along the fiber length.
Fig. A.6 shows as the attenuation changes respect with the wavelength for a SI-POF produced by the Italian company Luceat. Although the attenuation levels vary slightly for different fibers in different points, the concept is that the attenuation changes very with the wavelength. Also,

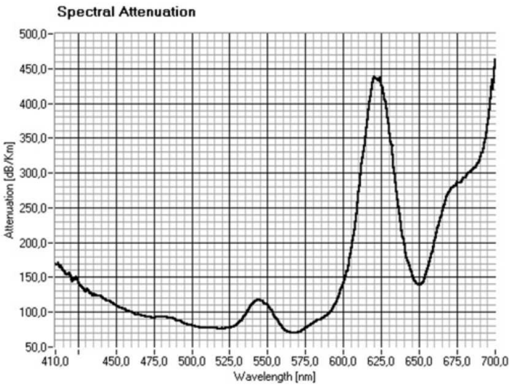

Figure A.6. Attenuation declared from Italian company Luceat for a SI-PMMA-POF with a 1 mm diameter.

POF is strongly multimodal and the path difference between the rays parallel to the axis and the propagation directions close to the critical angle of total reflection is significant, becoming cause of additional attenuation.
Furthermore, another cause of mode-dependent attenuation is that resulting from the effect known as *Goos – Hänchen Shift*. This effects happens when the electrical field moves to the cladding (optically the thinner medium) by a distance in the order of magnitude of the wavelength. Hence, the reflected ray is slightly displaced on the interface surface and the additional light path is subjected to the higher attenuation of the cladding material. This effect is particularly striking when the core diameter is very reduced in size respect of the cladding one. Actually this effect occurs also in glass fibers but is negligible. Another effect of additional attenuation is the *mode coupling*. This term refers to the process by which energy from one direction of propagation is transferred to several others. Mode coupling occurs predominately at the core/cladding interface, and it is also dependent on the angle of propagation. The shorter is the coupling length, larger is the additional attenuation due to mode coupling. The coupling length of a fiber is defined as the

state of equilibrium arisen through mode conversion and coupling.
Theoretically, the concepts expressed above are true for straight fibers. In fact, when the fiber is bent, the modes propagation would be to recalculate for the system of coordinate suitable for bent fiber. However, it is appropriate consider as straight the region before and after the bend, and perform a new reference axis only for the bending part.
Furthermore, the attenuation change slightly due to other causes relative to the fiber production: manufacturer and diameter. Two examples [18] are reported in Fig. A.7 and in Fig. A.8. The first example shows the attenuation measured for three fibers nominally equals but produced by three different manufacturers, while the second one shows the attenuation differences between three fibers of the same manufacturer having three different diameters.

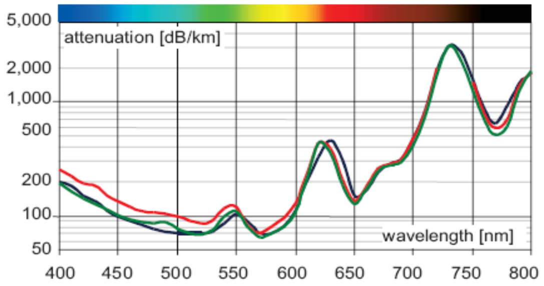

Figure A.7. Attenuation measured for three plastic optical fibers with the same characteristics but produced by different manufacturers.

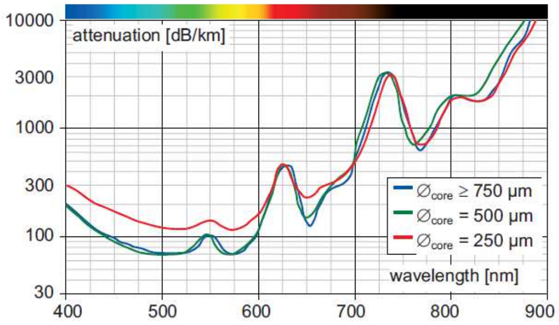

Figure A.8. Attenuation measured for three plastic optical fibers of the same manufacturer having three different diameters.

Bending

Bending of plastic optical fibers is another critical aspect. The bending attenuation is typically determined from the fiber diameter and its numerical aperture, also it is not directly proportional to number of bends that follows each other, because high modes transport less energy than lower modes. The larger is NA, lower is bending sensitivity, because lower is the minimum bending radius. The bending problem regards primarily SI-POF because of total internal reflection at

core/cladding interface.
A special case bend insensitive is constituted from the MultiCore POF, that have a very low sensitivity to bending.

A.3 Fiber optic sensors

The greatest advantages of a fiber-optic sensor (FOS) are intrinsically linked to the optical fibre nature itself. Since the light confined in the core of the optical fibres does not interact with any surrounding electromagnetic field, fibre-optic sensors are intrinsically immune to any electromagnetic interference. By design, fibre-optic sensors are intrinsically safe since they do not light fires, making them particularly suitable for health monitoring applications risky structures or unsafe conditions. Also, fibre-optic sensors have small size, resulting appropriate in space-restricted environments, such as thin composite structures. At least, the ability to measure over great distances without the need for any electrically active component is also an advantage. This can be an important feature when monitoring large and remote structures.

A.3.1 Classification

The fiber optic sensors can be classified according to several schemes, according to:

- fiber material: sensors based on Glass Optical Fiber (GOF) or Polymeric Optical Fiber (POF)
- function: intrinsic or extrinsic sensors
- working principle: intensiometric, interferometric, polarimetric or spectrally-based sensors
- quantity to be measured: physical, chemical or biomedical quantities.
- measurement point distribution: single measurement point, quasi-distributed or distributed sensors

Material

Differences between glass optical fibers and plastic ones have been explained in the first chapter of the appendix in the section regarding the fiber material. From the point of view of fiber sensor technology, the main differences are about costs and ease of use. Fiber glass sensors costs are significant higher due to fibers handling (during production and installation processes) and fibers interrogators. Otherwise, POF sensors are low-cost, because they are easy to use (size up to few millimeters and high flexibility due to high Young's modulus) and to interrogate (high diameter and numerical aperture cause high capability of collect light and then a non coherent light source and a photodetector are enough). In general, in the sensors field, a smaller area but currently growing, the choice between glass or optical fibers depends on the specific application and available budget.

Function

Fiber sensors can be classified in *intrinsic* or *extrinsic*. In intrinsic fiber sensors, fiber is the sensing element and also transports the light. Extrinsic sensors are composed of a modulator and a fiber, where the modulator is sensitive to the quantity to be measured, while the fiber is simply a link to relay signals from the sensor to the data processing unit, as shown in Fig. A.9.

Sensor working principle

The working principle changes according to which parameter modulates the light in the fiber. Therefore, the fiber sensors can be classified in intensiometric, interferometric, polarimetric, spectrally-based sensors respectively if the quantity to be measured from the fiber sensor is proportional to

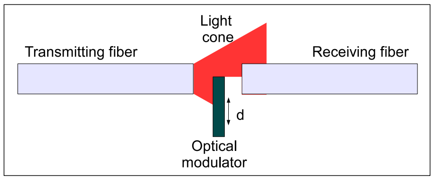

Figure A.9. Sketch of displacement extrinsic IB sensor with external modulator.

amplitude intensity, phase, polarization, wavelength. Intensiometric or intensity variation sensors are widely employed because of their simple realization. In detail, intensity based sensors can be distinguish in extrinsic or intrinsic. The extrinsic sensors are farther classified according to the presence of an external optical modulator. In the case without optical modulator, the sensors are *Numerical Aperture* sensors in the sense that the detected light is proportional not only to the distance but also depends on the light distribution, since a larger numerical aperture corresponds to a larger amount of light. Otherwise, the intrinsic sensors exploit the fiber losses, detecting the fiber bending, the critical angle or the evanescent field. In the particular case of extrinsic intensiometric sensor without optical modulator, that are very diffused as easy to arrange, the sensor sensitivity depends on the fiber numerical aperture. As in far field the optical power has a gaussian shape, the light NA sensors can work in transmission mode, where the fibers are facing each other, or in reflection mode, where the fibers are both facing to a reflecting target, as shown respectively in the Fig. A.10(a) and in Fig. A.10(b).

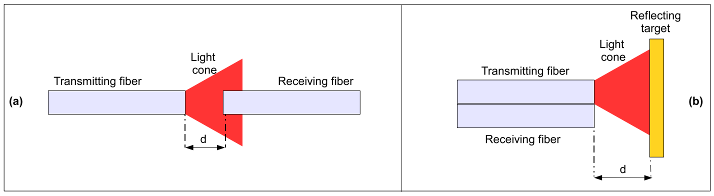

Figure A.10. NA sensor working in two modes: transmission mode (a) and in reflection mode (b).

Measuring quantity

Other type of classification is based on the quantity that the fiber measures, and it is divided in three categories:

- physical quantities: temperature, strain, pressure, displacement, distance
- chemical quantities: PH, pollutants, selective detection of specific molecules
- bio-medical quantities: blood pressure, glucose contents, selective detection of specific biomolecules

Measuring point number

The sensors can be classified as:

- point sensors: the measurement point is single. E.g. intensity based sensors, a single fiber Bragg grating

- quasi-distributed sensors: several point sensors are multiplexed allowing measurement at multiple points. The multiplexing can be based on wavelength, time or space division. E.g. OFDR, OTDR

- distributed sensors: the sensing is continuous at any point along a single fiber. E.g. Fiber Bragg Gratings

A.3.2 Application fields

Fiber optic sensors provide an interesting alternative to the electrical or mechanical traditional sensors in several application fields:

- Civil engineering: fiber optic sensors are employed in landslide evolution and Structural Health Monitoring (SMH), that includes also cultural heritage preservation, post seismic crack opening analysis and monitoring of civil infrastructures especially regarding the crack monitoring

- Mechanical engineering: optical fibers are typically employed to realize instruments as gyroscopes and accelerometers

- Industrial applications: fiber optic sensors are employed to measure several parameters, like as temperature (e.g. temperature of electrical power transformers), electrical current, pressure, vibration, acoustic fields and flow (e.g. for downhole oil and gas reservoir monitoring, in both retrievable and permanently installed systems)

- Medicine and bio-engineering: blood pressure, glucose contents, muscular force and specific bio-molecules can be detected by suitable optical fiber sensors

- Chemical sensing and environmental protection applications: fiber sensors are employed to measure pH, gases, ion and to detect explosive substances or dangerous chemical compounds by functionalization of the fiber surface

A.3.3 Structural monitoring fiber sensors

These type of sensors are further described because they represent a significative case of fiber optical sensors employed in structural monitoring.

Fiber interferometric sensor

An interferometric sensor is composed of two cleaved optical fibers facing each other with a micrometric air gap between them. When the light is launched into the fiber, a back reflected interference signal is obtained. This interference is demodulated using coherent or low-coherence technique to reconstruct the changes in the fiber spacing, because these variations are proportional to the average strain between the two points.

Fiber sensors based on Optical Time Domain Reflectometer (OTDR) technique

In the fiber OTDR, an optical pulse is launched in the fiber and a photodetector measures the backscattered light as the pulse is propagated through the fiber. The detected signal decays exponentially with time, that is proportional to the fiber linear attenuation. Knowing the light speed, the distance information can be extracted from the time information. Given that the OTDR technique is based on scattering phenomenon, Raman and Brillouin scattering have been used in many distributed sensing applications. Exploiting the Raman scattered light, that depends on thermally influenced molecular vibrations, and filtering in a suitable way the detected signal, the backscattered light carries the information on the local temperature where the scattering occurs. Measurement systems based on Brillouin scattering are commercially available from different producers for temperature and strain measurements, Raman scattering sensors are available commercially only for distributed temperature measurements in several structural monitoring applications.

Fiber Bragg Grating sensors

Bragg gratings are imposed periodic alterations in the core refractive index, fabricated by exposing the fiber to an intense UV-laser light. FBG sensors are distributed Bragg reflectors based on photosensitive fibers and they behave as frequency selective mirrors. Bragg gratings are imposed periodic alterations in the core refractive index, fabricated by exposing the fiber to an intense UV-laser light. Gratings manufacturing are obtained on a germanium-doped silica fiber, through several techniques: two-beam interference (UV beam is split in two others that interfere creating a periodic intensity distribution), phase mask technique (photomask with desired pattern is placed between the UV light and the fiber), point-by-point technique (a single UV laser beam creates the grating). The period of grating Λ determines the frequency at which an input wavelength λ_1 is reflected from the FBG and it is dependent from the strain and the temperature. When a tuneable light source is injected into the fiber containing the grating, the wavelength corresponding to the grating pitch will be reflected while all other wavelengths will pass through the grating undisturbed, as shown in Fig. A.11. FBGs are characterized by reflectivity, bandwidth, and side-lobe (or grating) strength. The grating strength, δn_0, determines the bandwidth. The grating length allows to set the peak reflectivity, which depends on both the grating length and strength. Side lobes can be controlled through the grading of the refractive index variation at the end of the grating, usually with gaussian or raised cosine profiles. In addition, the reflected spectrum can be broadened and the dispersion can be controlled by a chirp, that is a linear variation in the grating period. As the refractive index and grating period change when externally mechanical or thermal perturbations are applied, it is possible exploit this mechanism to realize FBG sensors, taking account that along the same fiber, several sensors can be inscribed, increasing the sensitivity. Therefore, the shift of

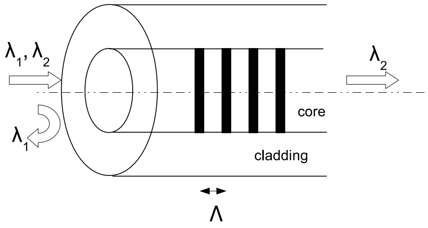

Figure A.11. Fiber Bragg grating principle the Bragg wavelength in response to strain ε and temperature variation ΔT is reported in Eq. A.5:

$$\frac{\Delta\lambda_B}{\lambda_B} = P_e \cdot \varepsilon + [P_e \cdot (a \cdot \alpha_s - \alpha_f) + \xi] \cdot \Delta T \tag{A.5}$$

where P_e is the strain-optic coefficient, α_s and α_f are thermal expansion coefficient respectively of the material surrounding the fiber and of the fiber itself, ξ is the fiber thermo-optic coefficient. Several interrogation methods, depending on the wavelength, can be employed to obtain the FBGs response. The spectrometer converts the wavelength position while matched filter or matched grating convert the wavelength amplitude. Alternatively, it is possible analyze the wavelength frequency (using AOTF) or the phase (employing an interferometer). Independently from interrogation technique, in quasi-static applications the intrinsic response of an FBG to both strain and temperature (called cross-sensitivity) makes almost indistinguishable any temperature variation along the fiber from the strain. To recover temperature and strain without ambiguity, a two-grating sensing system is used to describe the relation between the wavelength shifts and the measurands, employing a reference FBG sensor shielded from strain and temperature. Otherwise, for dynamic strain, the cross sensitivity is not a relevant issue, since the thermal fluctuations occur at low frequencies and they do not overlap the resonance frequency. In particular, FBG sensors are present in literature employed as seismic [45], strain and temperature sensors [46] and also they have been exploited commercially to detect strain and temperature, like as shown in Fig. A.12, and acceleration, as shown in Fig. A.13).

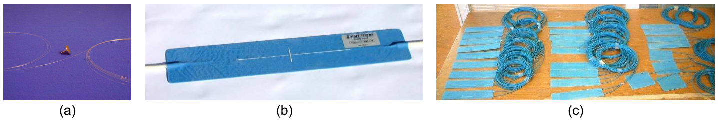
(a) (b) (c)

Figure A.12. Unpackaged (a) and integrated in a flexible patch (b),(c) Fiber Bragg grating sensors for strain and temperature measurements.


(a) (b)

Figure A.13. Examples of commercial single axis accelerometers based on Fiber Bragg Gratings up to 100 m/s^2 (a) and 400 m/s^2 (b).